ABSTRACT

Title of dissertation: MEASUREMENTS OF THE TWO-PHASE VORTICAL FLOW AND TURBULENCE CHARACTERISTICS BELOW A ROTOR

Jürgen Rauleder
Doctor of Philosophy, 2014

Dissertation directed by: Minta Martin Professor J. Gordon Leishman
Department of Aerospace Engineering

Time-resolved particle image and particle tracking velocimetry measurements were made in the particle-laden turbulent flow environment below a rotor hovering over a mobile sediment bed. The results were also compared to the near-wall flow produced by a nominally equivalent two-dimensional wall jet. The objective of the work was to understand the fluid dynamic mechanisms of how the mean flow, stochastic turbulence, and concentrated vorticity produced by the rotor affected the mobilization and pickup of particles from the sediment bed. Another objective was to better understand the assumptions that would be required for the development of models that are more applicable to rotor-induced particle mobilization. It was shown that the mean flow in the boundary layer at the ground below the rotor was similar to that of a wall jet. However, the instantaneous flow field and turbulence characteristics between these two flows were significantly different. Mobilized particles of 45–63 μm diameter (with a particle Reynolds number of less than 30 and a Stokes number of about 60) were individually identified and tracked, with the objective of

relating any changes in the temporal evolution of the vortical flow and turbulence characteristics of the carrier flow phase to its coupling to the dispersed particle phase. The processes of particle mobilization and pickup from the bed were found to correlate to the Reynolds stresses and discrete turbulence events, respectively. The mean flow and turbulence characteristics were modified by the presence of particles in the near-wall region, showing clear evidence of two-way coupling between the phases of the resulting two-phase flow. Specifically, it was shown that the uplifted particles altered the carrier flow near the sediment bed, leading to an earlier distortion of the flow induced by the blade tip vortices and to the accelerated diffusion of the vorticity that they contained. The uplifted particles were also seen to modify the overall turbulence field, and when sufficient particle concentrations built up, the particles began to attenuate the turbulence levels. Even in regions with lower particle concentrations, the turbulence was found to be attenuated by the indirect action of the particles because of the distortions to the tip vortices, which were otherwise a significant source of turbulence production. After the tip vortices had diffused further downstream from the rotor, the uplifted particles were also found to increase the anisotropy of the resulting turbulence in the flow.

MEASUREMENTS OF THE TWO-PHASE VORTICAL FLOW AND TURBULENCE CHARACTERISTICS BELOW A ROTOR

by

Jürgen Rauleder

Dissertation submitted to the Faculty of the Graduate School of the
University of Maryland, College Park in partial fulfillment
of the requirements for the degree of
Doctor of Philosophy
2014

Advisory Committee:
Minta Martin Professor J. Gordon Leishman, Chair/Advisor
Alfred Gessow Professor Inderjit Chopra
Associate Professor James D. Baeder
Keystone Associate Professor Christopher Cadou
Wilson Elkins Professor James Duncan

Dedicated to my parents, the first and most subtle mentors I had.

And to many professional and personal mentors who came thereafter.

I am in their debt, especially those who do not know because I have never told them that they are an important part of my life.

Stress, relief, dust cloud,

come and gone,

dinner table full of love.

– Haiku inspired by RV II, RV III, CV, and JV.

Acknowledgments

I would like to thank Professor Siegfried Wagner at the University of Stuttgart who was the first to introduce me to and engage me in the amazing yet challenging subject of helicopter aerodynamics and dynamics. By his mentorship, he enabled me to embark upon a rotorcraft research and education journey that is certainly not finished with the completion of this dissertation. Leaving family and friends behind (yet only geographically), I crossed the pond and found a new academic home for the next leap. I am grateful for all the faculty members of the Alfred Gessow Rotorcraft Center at the University of Maryland for their support and for teaching me all aspects of rotorcraft science and technology, in the classroom and beyond. My biggest thank-you goes to Professor J. Gordon Leishman, my advisor, teacher, and mentor. He took this new and quite direct German guy "fresh off the boat," and he gave me the guidance yet the freedom in research that I needed. I took the opportunity and I will make good use of all that I have learned from him.

I would like to thank the other members of my advisory committee for their guidance and support, namely Professor Inder Chopra, Professor James Baeder, Professor Christopher Cadou, and Professor James Duncan. I would also like to acknowledge Professor James Wallace for our discussions in turbulence and boundary layer research. Thanks to Anish Sydney and Joe Milluzzo. With their experience in experimentation and measurement techniques they made a lot of my work possible. Furthermore, I would like to thank Bharath Govindarajan who seems to have an answer and a solution to every problem you may have.

My parents, my girlfriend Annick, and my friends deserve great gratitude. I learned a lot from them and they have been a constant source of support throughout my life. The advice of my parents and a lot of my friends has made (and still makes) a difference in who I am and how I do things in my life, both professionally and personally. While there are a lot of friends to be grateful for, I would like to specifically thank Jared Grauer and Robert Vocke for their friendship and support during my years in Maryland, and beyond. Finally, I would like to thank the Vocke family for their open door. Your hospitality and love will stay with me, unlike a dust cloud; I am sure you did not need this elaboration on the Haiku.

Table of Contents

List of Figures

Nomenclature

Roman Symbols

A	Rotor disk area, m^2
c	Chord of the rotor blade, m
C_T	Rotor thrust coefficient, $= T/\rho A(\Omega R)^2$
d_c	Vortex core diameter, m
d_p	Particle diameter, m
h	Nozzle exit height, m
k	Turbulent kinetic energy (in 2-D), $= 0.5(\overline{u'^2} + \overline{v'^2})$, $\mathrm{m}^2\mathrm{s}^{-2}$
l_e	Characteristic length scale of energy-containing eddies, m
L_m	Spatial resolution, $\mu\mathrm{m\,pixel}^{-1}$
N_b	Number of rotor blades
p	Pressure, $\mathrm{N\,m}^{-2}$
r	Radial distance measured from rotor axis, m
r_c	Vortex core radius, m
R	Rotor radius, m
Re_c	Blade tip chord Reynolds number, $= V_{\mathrm{tip}}c/\nu$

Re_{jet}	Jet Reynolds number, $= u_{\text{jet}} h/\nu$
Re_v	Vortex Reynolds number, $= \Gamma_v/\nu$
St	Stokes number, $= \tau_p/\tau_f$
t	Time, s
T	Rotor thrust, N
T_u	Streamwise turbulence intensity, $= \sqrt{\overline{u'^2}}/v_h$
T_v	Wall-normal turbulence intensity, $= \sqrt{\overline{v'^2}}/v_h$
u, v	Flow velocities in r and z directions, respectively, $\mathrm{m\,s^{-1}}$
$\overline{u}, \overline{v}$	Mean velocities in r and z directions, respectively, $\mathrm{m\,s^{-1}}$
u', v'	Fluctuation velocities in r and z directions, respectively, $\mathrm{m\,s^{-1}}$
u_{jet}	Nozzle exit velocity, $\mathrm{m\,s^{-1}}$
$u_{\max}$	Maximum flow velocity, $\mathrm{m\,s^{-1}}$
u_τ	Friction velocity, $= \sqrt{\tau_w/\rho}$, $\mathrm{m\,s^{-1}}$
u^+	Normalized wall-parallel velocity, $= u/u_\tau$
v_h	Hover induced velocity, $= \sqrt{T/2\rho A}$, $\mathrm{m\,s^{-1}}$
V_{tip}	Rotor tip speed, $= \Omega R$, $\mathrm{m\,s^{-1}}$
x	Downstream distance measured from nozzle exit, m
z	Distance above the ground plane, m
$z_{\max}$	Distance of maximum velocity from wall, m
z^+	Normalized distance from ground, $= z\, u_\tau/\nu$

Greek Symbols

Γ_v	Vortex circulation, $\mathrm{m^2 s^{-1}}$
δ	Boundary layer thickness, m
ϵ	Energy dissipation, $\mathrm{m^2 s^{-3}}$
ζ	Wake age of the tip vortex, deg
μ	Dynamic viscosity, $\mathrm{kg\,m^{-1} s^{-1}}$
ν	Kinematic viscosity, $= \mu/\rho$, $\mathrm{m^2 s^{-1}}$
ρ_f	Air density, $\mathrm{kg\,m^{-3}}$
ρ_p	Particle mass density, $\mathrm{kg\,m^{-3}}$
σ	Rotor solidity, $= N_b c/\pi R$
τ_f	Characteristic fluid time scale, s
τ_p	Particle relaxation time, $= \rho_p d_p^2/18\rho_f \nu$, s
τ_{rz}	Reynolds shear stress (in 2-D), $= -\rho\,\overline{u'v'}$, $\mathrm{N\,m^{-2}}$
τ_{rr}	Normal Reynolds stress in the r direction, $= -\rho\,\overline{u'^2}$, $\mathrm{N\,m^{-2}}$
τ_{zz}	Normal Reynolds stress in the z direction, $= -\rho\,\overline{v'^2}$, $\mathrm{N\,m^{-2}}$
τ_w	Wall shear stress, $= \mu \left(\frac{\partial u}{\partial z}\right)_{z\to 0}$, $\mathrm{N\,m^{-2}}$
ψ_b	Blade azimuth angle, deg
Ω	Angular velocity of the rotor, $\mathrm{rad\,s^{-1}}$

Abbreviations

CCD	Charge-coupled device
CFD	Computational fluid dynamics
CMOS	Complementary metal oxide semiconductor
FFT	Fast Fourier transform
Nd:YAG	Neodymium-doped yttrium aluminum garnet
Nd:YLF	Neodymium-doped yttrium lithium fluoride
PIV	Particle image velocimetry
PTV	Particle tracking velocimetry
RANS	Reynolds-averaged Navier–Stokes
rms	Root mean square
ROI	Region of interest

Chapter 1: Introduction

The present research work is motivated by the problem of rotorcraft brownout. Although the brownout problem is operational in nature, the complex multiphase fluid dynamics involved must first be fully understood to better understand the underlying physics of this problem and to determine strategies for brownout mitigation. The underlying mechanisms are manifold and the problem is a true multidisciplinary research problem, involving the research fields of sedimentology, flow physics, fluid/particle dynamics and multiphase flows, turbulence and boundary layers.

1.1 Motivation: Rotorcraft Brownout

The rotorcraft brownout problem is a well recognized but poorly understood problem that occurs when rotorcraft are operating near ground surfaces covered with loose sediment, especially in desert areas. The occurrence of brownout is characterized by the rapid evolution of a large dust cloud around the rotorcraft that is generated by the rotor wake, especially during takeoff, approach, or landings. A typical dust cloud generated by a helicopter encountering brownout conditions during landing is shown in Fig. 1.1. The severity of the dust cloud can greatly reduce

the pilot's ability to distinguish visual cues on the ground that would normally be used as a reference for landing purposes, thereby compromising the safety of flight. Furthermore, if the rotorcraft is completely engulfed in the dust cloud, the suspended sediment particles can cause motion cue anomalies or vection illusions, i.e., the pilot perceives a relative motion of the vehicle that is not real. This perception may lead the pilot to applying improper control inputs, in some cases leading to a crash.

Brownout is not as much of a problem during takeoff because in this case the pilot often has the opportunity to quickly climb the rotorcraft out of the evolving dust cloud. However, the risk during landing is much higher, because to land the rotorcraft safely it must be slowly decelerated and the pilot must see the ground. The loss of situational awareness under brownout conditions is a substantial cause of human-factor-related rotorcraft mishaps during military operations. According to Mapes et al. [4], brownout occurrences are one of the most frequent reasons for human-factor-related helicopter airframe losses and loss of life during U.S. military operations. Although not limited to military operations, because of the nature of their missions, brownout-related mishaps with military rotorcraft by far outnumber those experienced by civilian rotorcraft [5].

Another aspect of rotorcraft brownout is that mechanical parts and material are subjected to abrasion by the airborne particles, which leads to serious damage over time, especially for rotating parts, rotor blades in particular, and to the engines. In fact, rapid engine wear and heavily eroded rotor blades contribute significantly to operational costs. For instance, in the worst desert conditions helicopter rotor blades last as little as 20 flying hours before damage from airborne particles becomes

Figure 1.1: Photographs showing the time-history of an evolving dust cloud for a helicopter in a landing maneuver over terrain covered with loose sediment. (From Ref. 1)

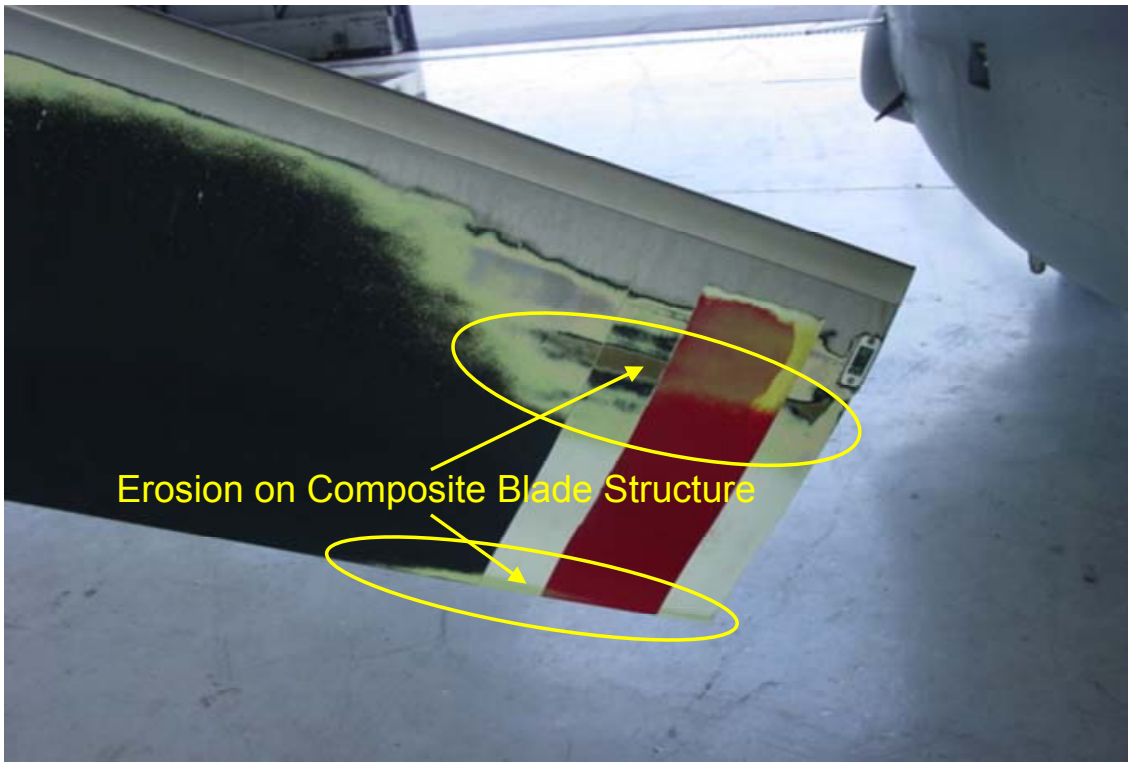

Figure 1.2: Photograph showing the erosion on a rotor blade caused by sediment particles.

so severe that they have to be removed and repaired or exchanged; see Fig. 1.2. This problem also reduces mission readiness rates because of the grounding of the rotorcraft for maintenance, repair and overhaul. In the field, this downtime can often be more important (and costly) than the actual expenses involved in the replacement of parts.

New sensors and avionics technologies have been developed to assist the pilot in safely maneuvering the rotorcraft during periods when brownout conditions are encountered. These enhancements help the pilot to compensate for the loss of

situational awareness if immersed in a brownout cloud [6–8]. While such systems can reduce the risks during takeoffs and landings, they do not solve the brownout problem nor do they eliminate the abrasion and/or wear problems. There are also piloting strategies to operationally mitigate brownout. Such strategies involve a faster landing approach thereby outpacing the formation of the dust cloud, steep flare maneuvers, rapid descent rates, etc. [9]. However, such techniques are only partially effective and sometimes risky or even prohibitive, e.g., because of the nature of the terrain or other obstacles around the landing site.

1.2 Rotor Flow in Ground Effect

The underlying physics of brownout involve three-dimensional unsteady, turbulent, two-phase fluid dynamics. The schematic in Fig. 1.3 shows the various fluid dynamic mechanisms that may contribute to the development of a particle cloud. A prerequisite to understanding brownout is to understand the fluid dynamics of the rotor wake as it approaches the ground, as well as the interaction of the rotor wake with the ground plane. Most prior research has examined rotor performance or the aerodynamics at the rotor itself rather than at the ground level [10–22]. More recent studies utilizing novel measurement techniques and simulations have furthered the knowledge about the aerodynamics of rotors and, in some instances, also about the fluid dynamics near the ground [23–28]. However, the complex flows near the ground are still not completely understood nor are they easily predictable [29–36].

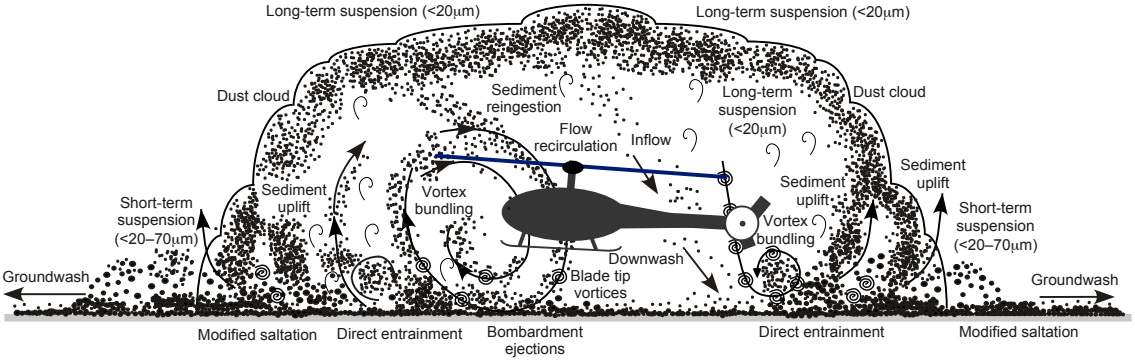

Figure 1.3: Schematic showing different modes of particle uplift and particle motions generated by a helicopter encountering brownout conditions.

Examinations of photographs and videography of brownout occurrences performed by Milluzzo and Leishman [37] have suggested that rotorcraft can produce very different dust clouds in terms of their spatial extent, concentration, and rapidity of their development, for reasons that are not yet well understood. During landing, some helicopters appear to produce radially expanding, toroidal-shaped dust clouds that can allow the pilot to maintain the necessary visibility and situational awareness; see Fig. 1.4(a). Some other helicopters produce large, more dome-shaped dust clouds where particles can recirculate through the rotor disk, bombard the sediment bed on the ground, and so eject many more sediment particles from the bed, which can cause the rotorcraft to be completely engulfed in the dust cloud; see Figs. 1.1 and 1.4(b).

There are many factors influencing the fluid dynamics and, therefore, potentially the development of a brownout cloud. According to Milluzzo and Leishman [37]

(a)

(b)

Figure 1.4: Photographs showing the evolution of a dust cloud for two different types of helicopters in a landing approach over dry, dusty terrain.

these factors include forward airspeed, rotor disk loading, blade loading, blade twist, number of blades, number and placement of rotors, and blade tip shape. The fuselage shape has also been shown to affect the aerodynamics at the ground and, therefore, it will be expected to influence the brownout signature; see Sydney and Leishman [38]. For a rotor operating in ground effect, the flow fields at the ground, in the near wake below the rotor, and at the rotor blades themselves all affect each other. Therefore, the detailed fluid dynamics in all of these regions have to be understood to be able to better understand the problem of brownout. Only then might a way be found toward the successful mitigation of brownout, at least from a fluid dynamics perspective.

1.3 Flow Physics Related to Brownout

Lee et al. [39] examined the effects of the ground on the overall flow field for several rotor heights off the ground, although they investigated only the single-phase flow (i.e., without sediment particles). Further experimental work on the brownout problem has been performed by Nathan and Green [40] who examined the effect of forward flight on the uplift of sediment particles in a wind tunnel. However, only dual-phase flow visualization was performed in this case, and quantitative results are not available. Johnson et al. [41] examined the two-phase flow (sediment and carrier phase) below the rotor using particle image velocimetry (PIV). These two-phase flow experiments, along with the recent laboratory experiments by Sydney et al. [2, 38], have given further insight into the flow physics related to brownout. However, there

is still a lack of knowledge about how the flow structures and their interactions with each other (and with the particles on the ground) affect the processes of sediment uplift and the development of a brownout cloud, and how turbulence in the flow affects these processes.

It has been suggested that if the flow physics of brownout and the underlying fluid dynamics that lead to particle mobilization and uplift can be better understood, then a predictive capability for brownout could be developed [42, 43]. To this end, the mean fluid motion, as well as coherent flow structures and turbulence events, must be fully understood as they relate to the processes of particle mobilization and pickup. Such improved understanding will be required to develop capabilities to reduce the severity of brownout conditions [44–46].

Recent experimental studies have better exposed the intricate fluid dynamic details of the flow conditions produced near the ground below a hovering rotor [39, 43, 44, 47]. Such flow fields contain the tip vortices and vortex sheets that are created at the rotor blades [48], as well as the associated eddies and smaller-scale turbulence, thereby creating a highly complex flow environment with intermittent characteristics; see Fig. 1.5. The pickup and suspension of particles from the sediment bed is at least partly caused by high surface shear stresses; see Bagnold [49], Shao and Lu [50]. However, the actual process is also affected by fluctuations in flow velocity and the turbulent Reynolds stresses, discrete turbulence events, local pressure gradients, and the unsteady upward (or wall-normal) flow velocities induced by the vortices [43, 51, 52].

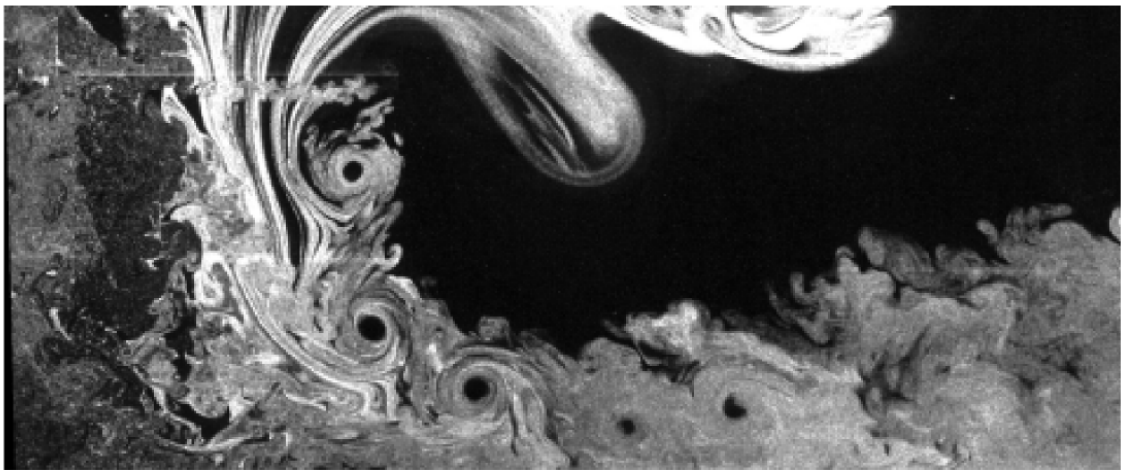

(a) Flow visualization image

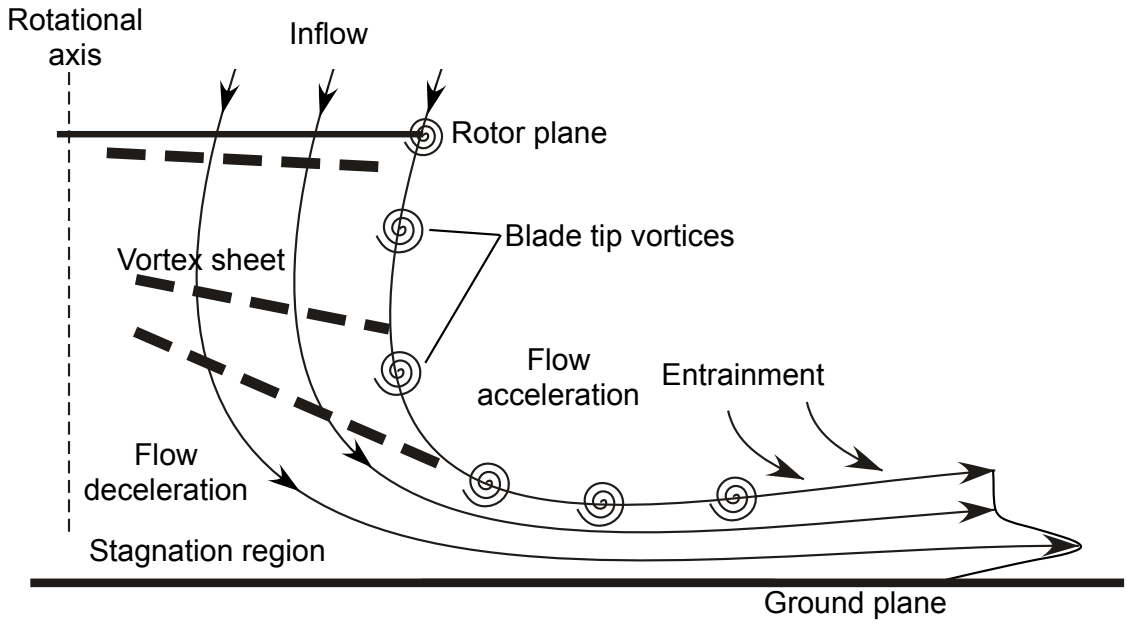

(b) Schematic of the flow

Figure 1.5: Flow features in the rotor wake developing in ground effect shown by: (a) flow visualization, (b) corresponding schematic of the basic flow characteristics.

1.4 Particle Dynamics

Fundamentally, the uplift of sediment is caused by the fluid-dynamic interactions of the rotor wake with the particle bed; see Fig. 1.3. The forces acting on a particle on the mobile sediment bed include shear forces in the boundary layer, gravitational forces, unsteady pressure effects induced by the vortices, and inter-particle forces [49, 50]; see Fig. 1.6. For a particle to become mobilized, the gravitational and the inter-particle forces must be overcome by the aerodynamic forces. Once uplifted and entrained, the dominant forces on the particle constitute the aerodynamic lift, drag, and other inertial forces; see Fig. 1.7.

The mobilized particles are convected by the energetic turbulent flow produced by the rotor. The smaller and lighter particles trapped in the stronger vortical flow regions of the rotor wake may also be recirculated back onto the sediment bed, ejecting many more particles by means of bombardment mechanisms, and so rapidly increasing the overall quantity of particles in the flow [2, 53, 54]; see Fig. 1.3.

During hover or slow forward flight at relatively low heights, the ground effect is strong and the uplifted sediment can also become reingested through the rotor disk into the main rotor downwash. These reingested particles are then bombarded back onto the ground, in the process ejecting many smaller particles from the sediment bed if the impact (and so the momentum transfer) is intense enough to overcome the forces responsible for keeping particles on the bed; see Fig. 1.6. These mobilized particles then, in turn, can be uplifted to greater heights or even suspended in the flow if the local fluid velocity components upward and away from the ground are sufficiently high

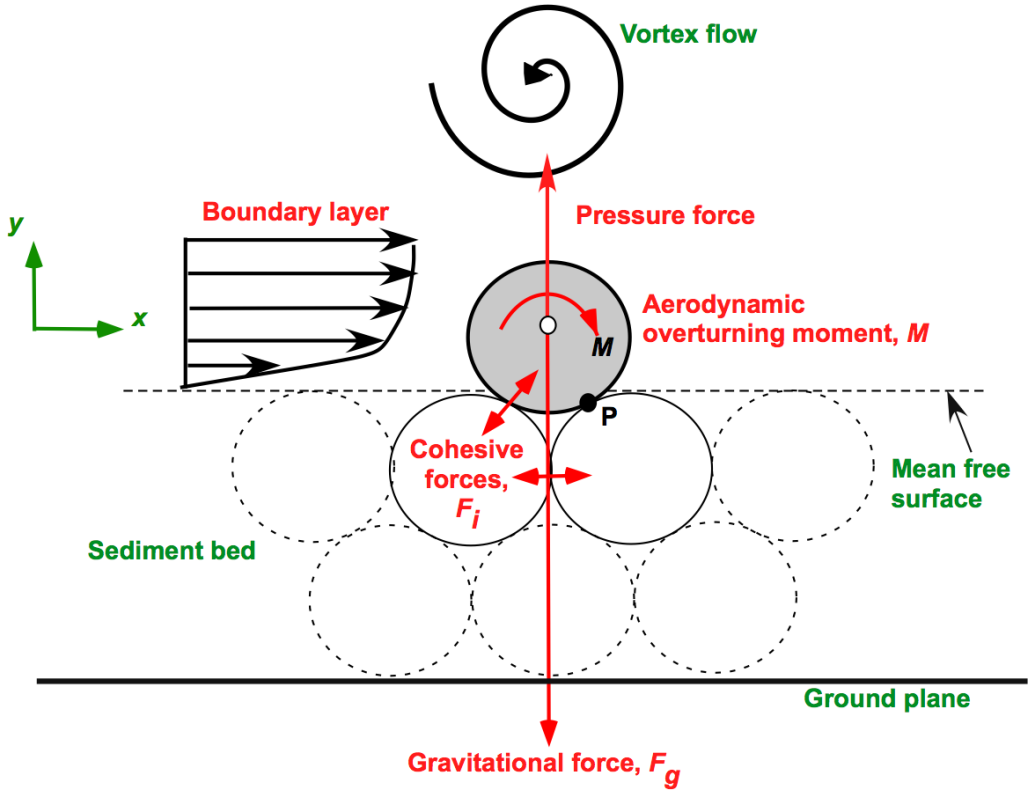

Figure 1.6: Schematic showing the forces and moments acting on a particle on a mobile sediment bed under the action of an external vortical flow.

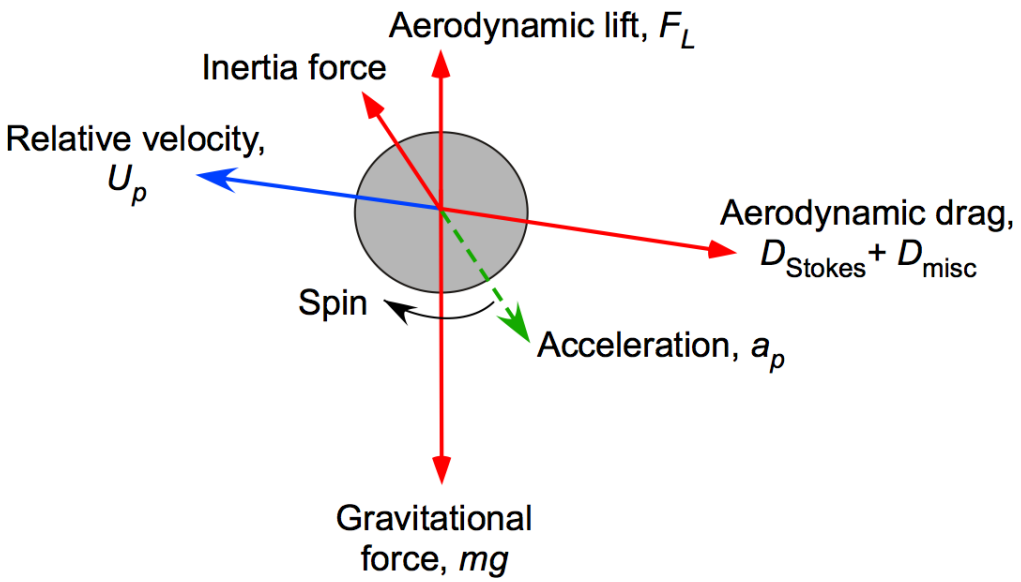

Figure 1.7: Schematic showing the forces acting on a particle in suspension.

to exceed the gravitational forces, e.g., if induced by a vortex convecting downstream. A schematic of this so-called "bombardment ejection mechanism" is shown in Fig. 1.8. Sydney et al. [2] showed that bombardment ejections were an important mechanism in the entrainment of sediment particles into the main flow, and so this mechanism should also be included in the modeling of brownout, as implemented by Syal and Leishman [54].

The lighter particles often reach substantial heights and are suspended in the air for relatively long time scales; see Fig. 1.3. Heavier particles (sometimes referred to as bedload particles) tend to creep along the sediment bed or they are moved into saltation, which is another characteristic transport mechanism of these bedload particles, according to Sydney et al. [2] and Johnson et al. [41]; see also Fig. 1.9.

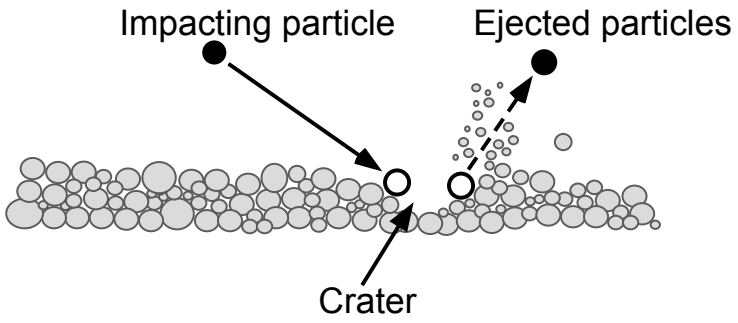

Figure 1.8: Schematic showing the bombardment mechanism as a contributor to the mobilization of previously stationary particles in the sediment bed.

Particle ejections are not only caused by the reingested particles but also by particles that saltate on the sediment bed and that impact other (often smaller) previously stationary particles, ejecting these from the bed by the momentum transfer during their collision. This latter mechanism is called saltation bombardment [2].

1.5 Tip Vortices as a Primary Contributor to Brownout

Each rotor blade trails one single, concentrated tip vortex, as shown in Fig. 1.10. Its characteristics, including the strength of the vortex, can vary with the shape of the rotor blade and also the blade tip it is trailing from. The vortex parameters, such as its swirl velocity and core size, are further dependent on the operational parameters of the rotor and the wake age of the tip vortex. Moreover, potential interactions with other flow structures (such as another vortex) can distort or diffuse the tip vortices [47], and if the rotor operates in ground effect, the tip vortex filaments can

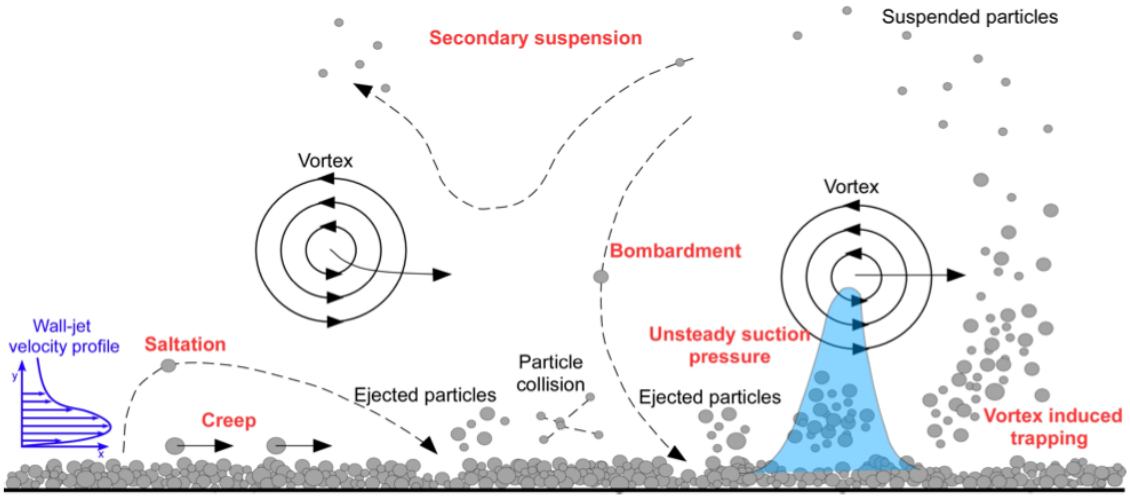

Figure 1.9: Schematic showing the characteristic particle transport mechanisms for a rotor-generated vortical flow. (From Ref. 2)

also be stretched and reintensified by their interactions with the ground plane [25].

Sydney et al. [2] and Johnson et al. [41] showed that when the blade tip vortices approach the ground they induce transient increases in the wall parallel velocity component that, in turn, can produce considerably larger values of shear stress on the sediment bed. By this mechanism, more sediment particles can reach their threshold friction velocities for mobility, causing them to creep, proceed into saltation, or become airborne and become entrained into the main flow. The tip vortices also create regions of significant instantaneous uplift velocity, i.e., a positive vertical velocity component, which is referred to as "upwash." These upwash velocities can not only uplift particles, but they also can cause smaller particles to be suspended around the rotor. Therefore, the tip vortices can be considered as being a primary

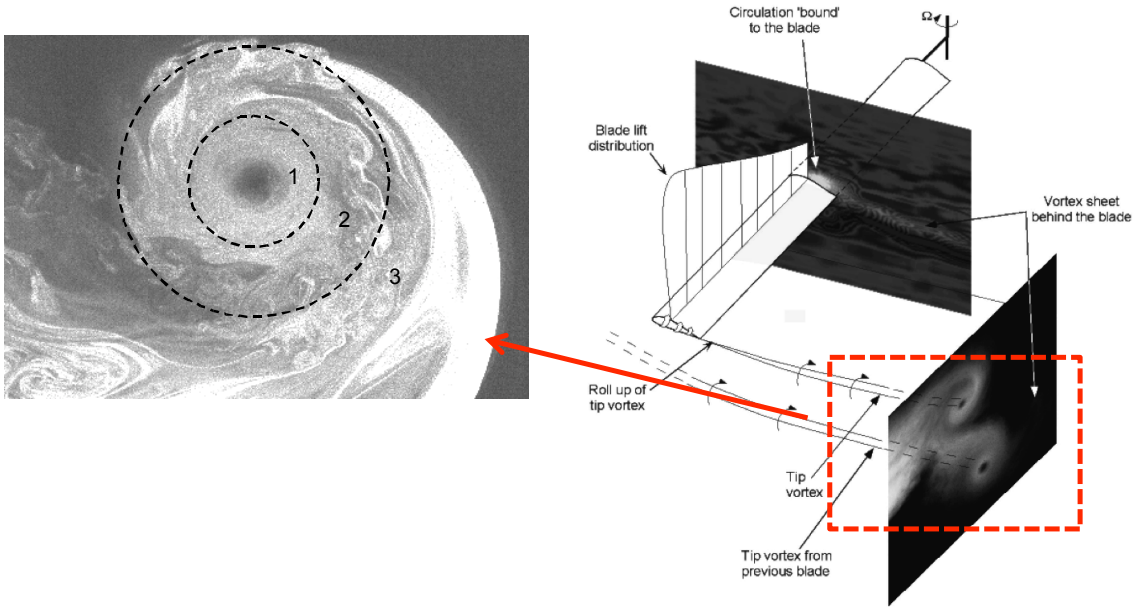

Figure 1.10: Schematic showing the roll-up of the tip vortices as well as a close-up view of a typical tip vortex with its three distinct regions: 1. the laminar core, 2. the laminar-turbulent transition region, 3. the turbulent outer region. (From Ref. 3)

contributor to the generation of brownout clouds, which was shown in previous dual-phase measurements by Sydney et al. [2] and by Rauleder and Leishman [43].

Because the rotor blade tip vortices have been identified as being a main contributor to the development of a dust cloud, the change in characteristics of these discrete vortices and their effects on the flow field in the near-blade region as well as near the ground have been examined [25, 44]. It is well known that the blade tip shape affects the characteristics of the trailed tip vortex [55–57]. Therefore, one of the key ideas in the attempts to mitigate brownout is in the use of appropriate blade tip shape, with the goal of changing the characteristics of the tip vortices and the overall flow field in a desirable way so as to reduce the vortex-induced velocities near the ground [44].

It was shown that one way to lower these induced velocities is by more rapidly diffusing the tip vortex, as achieved by a slotted blade tip design of Han and Leishman [58]. The results from the numerical simulations by Syal et al. [45] later suggested that this approach of more rapidly diffusing the tip vortices resulted in a lower quantity of uplifted particles and it also produced less severe brownout conditions when observed from a pilot's point of view. However, such results have not yet been proven by flight tests or laboratory experiments.

The discrete tip vortices are several rotor revolutions old when they reach the ground, and while they convect downstream in the flow they encounter a complex unsteady flow field containing other tip vortices (trailed from a different blade), the turbulent wake sheets, and high levels of turbulence; see Fig. 1.5. It was previously shown that these flow structures may interact with each other, inducing extra velocities or causing "vortex bundling" or "vortex merging" [2]. As a consequence of these interactions, smaller-scale eddies and turbulence are generated, which can alter the turbulent flow environment near the ground [43]. This behavior affects the Reynolds stresses and velocity fluctuations near the ground and so the total shear stresses on the sediment bed; see Rauleder and Leishman [43]. The tip vortices themselves may also be influenced by their interactions with the sediment particles. Such a coupling of the fluid phase to the dispersed particle phase has not been studied yet for a vortically-dominated flow, and understanding the effects of suspended sediment particles on the vortex structures was, therefore, part of the present research.

1.6 The Effects of Turbulence in the Dual-Phase Flow

The stochastic nature of turbulent boundary layer flows has been well investigated and documented in the literature [59–61]. However, there has been little previous experimental research into the turbulent boundary layer flow in the flow environment produced at the ground below a rotor system, not even for single-phase flows (without sediment). Therefore, one objective of the present research was to better understand the flow characteristics that cause the incipient motion of particles on the sediment bed, and as to how these particles become uplifted and entrained into the rotor flow. To this end, this complex, rotor-generated flow environment near the wall was dissected into its fundamental flow components, namely the mean flow (a wall jet-like flow), the unsteady nominally periodic part (mainly induced by the blade tip vortices), and the stochastic part.

Research has been conducted into the effects of discrete turbulence events on the Reynolds stresses by Wallace et al. [59]. However, there is little understanding as to how turbulence affects the mobilization, transport, and entrainment of sediment particles in vortically-dominated flows. Moreover, some results given in the literature are conflicting [51, 52, 62, 63]. It has been previously recognized that turbulence can play an important role in particle mobilization by the wind [49, 52, 64], and that turbulence events (or organized turbulence) can be responsible for the initiation of sediment motion below the mean threshold velocity conditions [51, 65]. For a number of different flows, it has already been shown that turbulence can significantly influence both the particle mobilization from a sediment bed and the subsequent particle

motion [66–68], although for rotor problems the effects are not yet understood.

The fluid dynamic mechanisms that could lead to brownout conditions have been previously studied in measurements of the dual-phase heterogeneous flow environment near a sediment bed below a rotor [2,40,41]. However, such studies have not yet investigated the detailed turbulence characteristics of such a flow. These characteristics could be very important because any change in the turbulence field may subsequently affect the processes of sediment mobilization and uplift of particles from the underlying bed, i.e., the physics of the problem are likely to include a degree of coupling between the carrier flow and the dust field. The relative significance of these couplings, however, is not yet well understood, and so obtaining a better understanding of such flow phase couplings is another objective of the present work.

Furthermore, turbulence effects on particle mobilization have not yet been modeled to an acceptable degree [68]. For example, sediment transport and particle uplift models, such as the well-known models of Bagnold [49] and Shao and Lu [50], do not explicitly account for the effects of turbulence and unsteadiness in the flow, although these semi-empirical models have been derived from certain wind tunnel tests with turbulent boundary layers. These models also do not account for the possibility that the mobilized particles may alter the carrier phase or any of the coherent flow structures it may contain, or even the resulting turbulence. Such flow modifications to the carrier phase can lead to modified aspects of the mechanisms of particle mobilization and uplift [68].

1.7 Modeling Rotor-Induced Dual-Phase Flows

Most models that have been used to predict the behavior of two-phase flows are based on semi-empirical descriptions of the mean flow [62], in most cases developed for channel or pipe flows. However, because of the dearth of experimental data and a fairly poor understanding of turbulent dual-phase flows, in general, such semi-empirical models are both difficult to formulate and challenging to validate [69]. These difficulties are particularly true for real-world problems such as brownout, which is vortically dominated, three-dimensional and highly unsteady. For example, in the absence of sufficient experimental data, turbulence models used in CFD simulations of two-phase flows often employ simple extensions of the standard single-phase $k-\epsilon$ model, which may or may not be correct; see e.g., Montante et al. [70,71]. In fact, it has already been suggested that such models should include interphase turbulence transfer terms for turbulence modulation [72].

Most existing numerical models of two-phase fluid flows do not include two-way coupling (i.e., the particles affect the carrier-phase flow and vice versa). However, even when ignoring the coupling between the phases, the modeling of the brownout problem is still extremely challenging. Modeling issues arise because the problem involves the development of highly swirling two-phase flows at relatively high Reynolds numbers, and so the anisotropy of turbulence may also have a significant effect on the mean flow. Furthermore, the rotor flow contains concentrated vorticity in the tip vortices that must be numerically preserved when they convect downstream from the blades toward the ground, which by itself is a significant computational challenge.

Nevertheless, ambitious simulations have been attempted [35, 53, 73–79] and they have given much insight into several aspects of the rotorcraft brownout problem, although numerous levels of assumptions and simplifications are necessary to make the modeling computationally efficient or even just feasible.

Besides the complexity of the rotor flow itself, simplified assumptions and approximations must also be used to model particle mobilization and transport from an underlying sediment bed. Such so-called "pickup" models are semi-empirical integral descriptions based on the assumptions of steady, uniform, turbulent boundary layer flows [80, 81]. However, in light of a growing body of experimental evidence, the validity of such models become increasingly questionable for the nonequilibrium types of flows found below a rotor. In steady, uniform boundary layers, the effects on particle mobility can be characterized by the shear stresses on the bed because the statistical distributions of the turbulent fluctuations scale with the friction velocity [62]. However, recent measurements [62, 82–84] have shown that nonuniformities in the flow can produce substantial changes in the near-bed turbulence field, which can then play an important role in the mobilization and entrainment of the sediment particles.

Vortex-induced effects have been raised to be a possible explanation for particle mobility below the normal (i.e., boundary-layer driven) threshold conditions [65, 85]. Xuan [68], Williams et al. [66], and Xuan and Robins [67] have investigated the effects of turbulence on sediment transport and how turbulence will affect the thresholds for sediment transport and particle flux. From wind tunnel tests, they concluded that turbulence significantly influenced the dust mobilization and particle mass flux in

the more canonical, aeolian flows they investigated. Xuan [68] derived parameters to amend the threshold friction velocity and the particle mass flux in existing models. However, little quantitative data yet exist to validate such models or to aid in developing better ones. Furthermore, while various hypotheses with regard to the effects of turbulence on sediment transport have been put forward, there is still an insufficient understanding of how coherent vortex structures affect the processes of particle mobilization from a mobile sediment bed.

1.8 Flow Phase Coupling and Turbulence Modifications

Turbulence studies in heterogeneous dual-phase flows with a solid particle (or dispersed) phase have been performed for a number of different flows, such as channel and pipe flows; see Poelma and Ooms [86] for a review. Even though there is some consensus regarding the effects of couplings between the flow phases (and turbulence modifications that appear as a consequence), there are still several conflicting results and a lack of general conclusions in the published literature [86, 87]. However, it is generally accepted that if the particle concentration in the flow is high enough, thereby changing the particle volume fraction and mass load (and possibly other flow properties as well), then the flow structures themselves and the turbulence properties can be modified [63, 82, 88, 89]. These findings suggest that the problem of brownout, for example, is most likely two-way coupled (i.e., the particles affect the carrier-phase flow and vice versa), or even four-way coupled (particle–particle interactions also

become important) whenever sufficiently high particle concentrations are produced; see Elghobashi [90].

The particle volume fraction is the fraction of the total volume occupied by the average quantity of particles measured in the region of interest (ROI) with respect to the volume of the fluid in this ROI. The average volume fraction of particles in the rotor wake was measured to be in the order of 10^{-5}. This volume fraction (often referred to as volume loading) is in the "two-way coupling regime" as defined by Elghobashi [90] and the flow is too dilute (by two orders of magnitude in the volume loading) for particle–particle interactions to have a significant effect on the fluid.

Elghobashi [90] classified three coupling regimes between the flow phases on the basis of the particle volume fraction in the fluid. For a volume fraction less than 10^{-6}, the presence of the particles has a negligible effect on turbulence in the flow and the interaction between the particles and turbulence is "one-way coupled." For a volume fraction between 10^{-6} and 10^{-3}, the momentum transfer from the particles is large enough to alter the mean flow and turbulence structure, and turbulence modifications may occur, also depending on other flow parameters. This interaction is termed "two-way coupled." For a volume fraction greater than 10^{-3}, particle–particle collisions become important, which can alter the trajectories and the spin of both of the interacting particles. As a consequence, the turbulence of the carrier phase can also be affected by such collisions, which is termed "four-way coupled."

The mass loading is the fraction of the total mass of the average quantity of particles measured in the ROI with respect to the mass of the fluid in this ROI. The bulk mass loading in the ROI was measured to be about 0.03. However, locally the

volume and mass loadings can be significantly greater than the bulk loading. The volume and mass loading heavily depends on the section (or control volume) that is used for calculating it because the particles are inhomogeneously distributed in this kind of flow; most particles are near the sediment bed with much fewer in the main flow above.

Experimental investigations into turbulence modifications have been conducted and are documented for a wide range of volume and mass fractions; see Poelma and Ooms [86] for a review. However, such studies were for channel flows and pipe flows that are much different from the rotor-in-ground-effect flows investigated in this study. Nevertheless, for horizontal channel flows, recent studies revealed that even for very low volume and mass fractions (that belong to the one-way coupling regime in some instances), the presence of the particles still resulted in significant turbulence modifications [63, 87, 89, 91]. It is well known that one of the main mechanisms for how turbulence can be attenuated is through particle–eddy interactions. Thus, for the (tip) vortex-dominated (i.e., eddy-dominated) rotor flow, an even stronger effect of the particles on the fluid flow is expected than in aforementioned studies of horizontal channel flows, even at very low volume or mass loadings.

Depending on the particle size, as well as the mass and volume fraction of the particles in the flow, the dispersed phase may produce [69] or suppress [88, 92–94] the turbulence of the carrier phase. Results and conclusions from different particle-laden flows, however, are not easy to generalize because they will depend not only on the fluid properties and particle parameters, but also on the type of flow and the flow regime [92]. There are also further challenges in the development of appropriate

predictive models that can be applied to such flows, mainly because of the complexity of the widely varying turbulence modifications that can occur in the different flow regimes, even in the absence of suspended particles.

Most numerical models are unable to accurately predict the turbulence modifications caused by a dispersed particle phase in the flow [93–95], i.e., such models are unable to correctly predict the physics in a turbulent dual-phase flow, even for relatively simple flow problems. Therefore, existing models that attempt to simulate the problem of brownout will also fall into this same category because they generally rely on assumptions that have been developed for simpler and often one-dimensional, quasi-steady flow problems. For example, in the presence of an organized motion such as a vortex, the assumption of isotropy in the turbulence model may be insufficient; see Thiesset et al. [96].

Introducing a dispersed phase that may alter the carrier-phase flow properties is certainly computationally challenging to model. However, for rotor flows, experimental evidence is yet to show whether the presence of uplifted sediment particles modifies the turbulence characteristics, or whether it changes the mean fluid flow, or both. Only if such evidence can be shown can the effort in modeling these flow modifications be justified, including the increased complexity of the numerical models and the increased computational expense of the resulting two-phase flow simulations (e.g., brownout simulations). Therefore, one goal of the present research was to experimentally examine any two-way couplings between the fluid flow and the dispersed particle phase in the flow below a rotor.

1.9 Objectives of the Present Work

The present research contributes to the understanding of the fluid dynamics responsible for the development of rotorcraft brownout conditions. It is the dynamic interplay of the flow features in the rotor wake and their interaction with the ground that makes it difficult to discern the fundamental mechanisms that contribute to the mobilization and pickup of mobile particles and to the formation of rotor-induced brownout conditions. Therefore, flow field measurements near the ground below laboratory-scale rotors were performed to understand the details of the rotor wake-induced flow, the flow-induced particle motion, and any particle-induced modifications to the vortical fluid flow.

The objectives of the present research were to quantify the particle mobilization and uplift from a mobile sediment bed below a rotor, and to better understand the fluid mechanic details of the processes involved. The role of both concentrated vorticity and stochastic turbulence in the rotor flow was investigated as it influences the motion of particles on the bed, the subsequent pickup of these particles from the bed and their suspension in the flow. Another objective was to establish useful approximations and boundary conditions for the development of better sediment entrainment models that are based on justifiable physical assumptions and that can be applicable to the modeling of rotor-induced brownout conditions.

The present work also furthers the understanding of the flow phase couplings and turbulence modifications in the dual-phase flow environment generated by a rotor when it is operating over a mobile sediment bed. The high spatio-temporal

resolution of the present measurements allowed for individual flow structures and turbulence to be resolved. With the simultaneous resolution of both of the flow phases, any changes in the temporal development of the vortical flow structures could be correlated to the action of the dispersed particle phase and to the degree of two-way coupling that was present in such a complex flow.

1.10 Overview of Dissertation

Chapter 1 has given the motivation and the objectives for the current research. The problem of brownout has been introduced, and various aspects of the problem have been discussed with a focus on the underlying dual-phase fluid dynamics that are involved in the generation of a brownout dust cloud. Because the problem of brownout truly is a multidisciplinary research problem, prior work has been reviewed in Chapter 1 as it pertains to the present research, including studies in sedimentology, flow physics, fluid/particle dynamics and multiphase flows, turbulence and boundary layer research. However, the outcomes from the reviewed studies are only partially applicable to the problem at hand because vortically-dominated flows have not been studied with respect to sediment mobilization and uplift, and also not with respect to the flow phase couplings in such flows. Therefore, flow field measurements near the ground below laboratory-scale rotors have been performed to understand the details of the rotor wake-induced flow, the flow-induced particle motion, and any particle-induced modifications to the vortical flow.

In Chapter 2, detailed descriptions are given of the experiments that have been performed, along with the methodology used to obtain the measurements. Three different experiments were conducted: 1. Single-phase flow measurements below a rotor of 0.816 m diameter operating over a ground plane, 2. Single-phase and dual-phase time-resolved flow field measurements below a smaller rotor of 0.17 m diameter, and 3. Time-resolved measurements of the flow produced by a nominally two-dimensional wall jet that developed over a ground plane as generated by the exit flow from a nozzle. The experimental setups are shown and explained, and the specific test conditions and operating parameters for each of the experiments are reported. The particle image velocimetry and particle tracking velocimetry measurement techniques are also introduced, as these techniques were used to measure the single-phase and the dual-phase flow fields. Furthermore, the image acquisition and data processing procedures are described in this chapter.

Chapter 3 shows and discusses the results from the analyses of the single-phase and the dual-phase flow fields. These measurements give much insight into the rotor-generated wall-bounded flows with and without sediment particles in the flow, including an analysis of the boundary layers developing over the ground plane and the sediment bed below the rotors, and also a comparison of these flows to more canonical types of flows. The vortical structures and the turbulence characteristics of the rotor-generated flows are documented, and they could be correlated to sediment mobilization and particle uplift from the underlying sediment bed. Furthermore, the detailed vortex flow–particle interactions are examined, including detailed investigations into the two-way coupling of the carrier flow to the

dispersed particle flow, and vice versa.

Chapter 4 provides a summary of the contributions of the present research to the state of the art in brownout research and in multiphase fluid dynamics. The specific conclusions that have been drawn from the performed measurements are given in this chapter, as well as recommendations for future work that could follow based on the results and conclusions drawn from the present research.

Chapter 2: Methodology and Description of the Experiments

This chapter contains a detailed description of the experiments that were performed. Technical descriptions are given of the hardware used to measure the characteristics of the single-phase and dual-phase flows. This chapter also describes the experimental techniques and methods that were used. The operating conditions and data acquisition parameters specific to each of the experiments are reported, and relevant data processing procedures are discussed.

2.1 Overview of Experiments Performed

Three different experiments were conducted and the results were analyzed in detail: 1. Single-phase flow measurements below a rotor of 0.816 m diameter operating over a ground plane, 2. Single-phase and dual-phase time-resolved flow field measurements below a smaller rotor of 0.17 m diameter, and 3. Time-resolved measurements of the flow produced by a nominally two-dimensional wall jet that developed over a ground plane as generated by the exit flow from a nozzle.

The 0.816 m-diameter rotor setup provided larger length scales and allowed for the resolution of the near-wall region with greater detail. However, with a rotor of

this size, dual-phase measurements were not practical because of the need to confine the dust or sediment particles inside the relatively large test section. Therefore, another set of experiments was performed using a smaller rotor system in a dust chamber to perform both single-phase and dual-phase flow measurements. All of the flow measurements were performed using two-dimensional, two-component particle image velocimetry (PIV) for the single-phase flows and for the carrier-phase in the dual-phase experiments, while particle tracking velocimetry (PTV) was used to measure the velocities of the sediment particles in the dispersed phase.

The objective of the wall jet experiment was to mimic the time-averaged flow over the ground plane that was produced by the rotors, mainly in an attempt to separate the unsteady effects of concentrated vorticity in the rotor wake flow near the wall from the other characteristics of the developing wall flow. In other words, the idea behind the nozzle-generated wall jet experiment was to learn more about the characteristics of the mean flow over the ground plane generated by the rotor. In the rotor case, a wall jet-like flow was formed over the ground plane, however, it contained the effects of concentrated vorticity and turbulence, mainly from the tip vortices and vortex sheets trailed by the rotor blades. The effects of these discrete rotor flow features cannot be isolated from the mean (wall jet-like) flow produced by the rotor.

However, when comparing the rotor-generated wall jet flow and the nozzle-generated wall jet flow to each other, the primary differences induced by individual flow structures should become apparent. For the purposes of this comparison, the measurements from the wall jet experiment were compared to the near-wall flow

measurements produced by the larger (0.816 m-diameter) rotor. The larger rotor was used because the larger length scales provided by this setup, along with the instrumentation used in this case, allowed for a finer spatial resolution of the near-wall region.

2.2 Experimental Techniques and Methods

Three different types of experimental techniques were used to make the measurements: (1) Flow visualization (FV); (2) Particle image velocimetry (PIV); (3) Particle tracking velocimetry (PTV). The working principles of each of these methods are introduced in this section also briefly explaining why the respective techniques were chosen to interrogate the flow. All three techniques were used with different laser and camera systems, depending on the specific purpose of each experiment. Reported in the following sections are details of the hardware used for each experiment, the data acquisition procedures, as well as processing techniques used when applying the measurement techniques to the respective experiments.

2.2.1 Flow Visualization (FV)

As an experimental technique, flow visualization (FV) provides a quick solution toward the understanding of the flow field being investigated. FV provides qualitative information about the flow and larger-scale flow structures it contains, and a rapid

assessment of the entire flow field is possible. Specific portions of the flow field that exposed interesting fluid dynamical features can then be explored further by means of quantitative PIV and PTV measurements.

In the current investigation, FV was used to obtain a global understanding of the flow fields. In particular, the regions were located that showed strong rotor wake–ground interactions and interesting flow phenomena so that these could be studied further. In the dual-phase flows being investigated, the regions of incipient motion of the sediment particles on the bed were also identified by means of FV, and so were the locations where the sediment particles became uplifted under the influence of the rotor flow. With this (qualitative) knowledge about the respective flows, detailed (quantitative) PIV and PTV measurements could then be conducted in these specific regions of interest (ROI). This latter approach was advantageous because it allowed the PIV and PTV techniques to be applied to smaller ROIs, therefore permitting higher spatial resolution measurements within these particular ROIs.

To visualize the flow, seed (or tracer) particles that are small enough to follow the flow were introduced into the carrier phase. For all of the experiments, mineral oil seed particles with a diameter of 0.2 μm were used. These seed particles were illuminated by a laser light source in a thin imaging plane to scatter light that was then recorded by a camera. Seeding the flow with tracer particles is an important part of FV and PIV experiments and is, therefore, explained later in more detail in Section 2.2.5. In contrast to PIV, the seed particles for FV do not need to be uniformly distributed in the flow. In fact, it is advantageous if a dense

concentration of seed is introduced into the flow relatively closely upstream of the flow features to be investigated, making them more clearly visible. For example, in the vortically-dominated flow produced by the rotor, seed particles were introduced near the blade tip upstream of the rotor to visualize the tip vortex; see Fig. 1.5.

2.2.2 Particle Image Velocimetry (PIV)

For the present studies, the PIV method was used to measure both the single-phase and the dual-phase flows. In the latter case, the PIV method was only used for calculating the fluid velocity vectors, while the velocities of the dispersed-phase particles were calculated by means of the PTV technique, which will be explained in Section 2.2.3. PIV is a non-intrusive measurement technique (other than for the seeding of the flow), i.e., this measurement technique does not change the characteristics of the flow as long as the seed particles are small enough to follow the flow faithfully.

The PIV method was used because it enables measurements of the flow field in an entire plane (rather than doing discrete point measurements) and in relatively short time intervals, i.e., the PIV method allows for the flow to be spatially and also temporally resolved. This capability of spatially and temporally resolving the dual-phase flows was needed to relate any sediment particle motion to the action of individual flow structures and discrete flow events. A high spatio-temporal resolution of the flow was also needed to correlate any possible changes in the characteristics of

the rotor-generated flow structures to the action of the dispersed particles.

To characterize highly swirling or rotating flows, one important measure of the flow is the vorticity. In this two-dimensional case, the out-of-plane vorticity, ω_y, was defined as

$$\omega_y = \left(\frac{\partial v}{\partial x}\right) - \left(\frac{\partial u}{\partial z}\right) \tag{2.1}$$

The vorticity is obtained from finite-difference estimates of the velocities obtained at neighboring measurement points.

For PIV, the flow is seeded with tracer particles, as also discussed later in Section 2.2.5. However, with PIV, the flow field needs to be seeded uniformly to obtain good measurements. The flow is illuminated twice consecutively within a relatively short time interval, the laser pulse separation time, Δt, which is of the order of microseconds. The light scattered by the illuminated tracer particles is imaged by a camera, yielding an image pair.

For the analysis, the resulting PIV image pair is divided into a grid of much smaller interrogation windows whose optimum size is to be determined by the average tracer particle displacement. The interrogation window size is typically of the order of 32 x 32 pixels. However, the optimum dimensions of the windows are governed by the flow regimes that are to be examined. For example, the window size requirements will be different for a near-wall flow compared to a highly swirling (e.g., vortex) flow.

Small groups of tracer particles (in the order of 10 particles) are tracked between the interrogation windows of the image pair. Sometimes the individual images of such an image pair are referred to as the first and second frame of a

double-frame recording. The tracer particles within the two associated interrogation windows are then cross-correlated. If all of the correlated particles have the exact same displacement, then the correlation function between the two windows will have a single maximum at one particular displacement. This measured displacement is then the displacement of the whole interrogation window (Δx, Δz in x and z directions, respectively). The according velocity vector for this interrogation window is subsequently calculated based on this displacement using

$$(u, v) = \frac{(\Delta x, \Delta z)}{M \Delta t} \tag{2.2}$$

where M is the optical magnification and Δt is the time that has elapsed between the two correlated images of a PIV image pair.

If not all of the particles within two cross-correlated interrogation windows are displaced by the exact same distance, then there will be several peaks in the correlation function, hence effectively increasing the signal-to-noise ratio. Without using advanced algorithms, the displacement found by the correlation in this case is approximately an average over the individual particle displacements. A Fast Fourier Transform (FFT) algorithm was used to perform the cross-correlations in the frequency domain before converting back to the spatial domain, which is computationally much more efficient [97].

Only one single velocity vector is obtained from each interrogation window. This process is repeated for all of the interrogation windows in the ROI, giving the instantaneous velocity vectors in the entire ROI that is being investigated, and so

giving the flow field at one point in time. For a more extensive description of the PIV measurement technique, see Adrian and Westerweel [97].

In general, various preprocessing, processing, and postprocessing measures are included in the PIV interrogation of the flow field. Such processing steps and some of the underlying algorithms are specific to the experiment to be performed and they are, therefore, discussed in the sections that are pertinent to the different experiments.

2.2.3 Particle Tracking Velocimetry (PTV)

In the PTV method, the displacements of individual particles are measured rather than the displacement of small groups of particles (as done in PIV). PTV uses a mean concentration of particles so low that the probability is small that images from two different particles will overlap. Therefore, the field of view recorded by the camera consists basically only of images of individual (dispersed-phase) particles. Based on size and brightness information, the individual particle images can be identified and located, which is discussed in more detail in Section 2.4.5.

Particle tracking proceeds by segmenting the image plane into a set of isolated (particle) images corresponding to the bright spots assumed to be particles. If a segmented image looks like a legitimate particle image, i.e., approximately round in shape and of the predicted diameter, its centroid is calculated using the pixel graylevel data. If there is an overlap of two or more particle images, either these can be discarded or an effort is made to separate these particle images and find their

individual centroids.

To make the velocity measurements, a pair of particle images is identified that corresponds to the same physical particle, and the centroids of these two images are used to calculate the displacement between the particle images. With these particle displacements in the image plane, Δx and Δz, the velocities are then calculated using Eq. 2.2.

PTV methods work best when the particle concentration is low, and so vector fields obtained by means of PTV tend to be rather sparse. The PTV method was well suited to measure the dispersed phase in the dual-phase flows investigated in this study because the concentration of sediment particles in the flow was dilute. For a more comprehensive description of the PTV technique see Adrian and Westerweel [97]. Further details of the used PTV methods that are more specific to the experiments being performed are given in Section 2.4.5.

2.2.4 Simultaneous Dual-Phase PIV/PTV Measurements

In the dual-phase experiments, the flow fields of both of the flow phases had to be acquired simultaneously to be able to correlate any changes in the carrier phase to the action of the dispersed-phase particles in the flow. Furthermore, measurements of a contiguous time-history of the dual-phase flow were also a prerequisite to relate any possible changes in the properties or characteristics of the coherent flow structures to the action of the dispersed phase, i.e., to investigate the degree and nature of

any two-way coupling between the flow phases. Another goal of this work, which necessitated a time-history of the flow, was to find out which characteristics of the fluid flow (e.g., discrete flow structures and turbulence events) were responsible for sediment mobilization, uplift and entrainment from a sediment bed below the rotor.

Because of the need to obtain both flow phases simultaneously, the particles used to seed the continuous phase were much smaller than the sediment particles in the dispersed phase. The size of the seed particles (0.2 μm) and the sediment particles (mean diameter of $\approx$ 54 μm) was different by two orders of magnitude. Furthermore, the dispersed phase was dilute and consisted of well-defined objects (soda-lime glass microspheres) that had a round shape of known diameter, so enabling effective phase separation criteria to be set. Therefore, it was possible to record both of the flow phases simultaneously with a single camera, and then use image processing methods to separate the flow phases. The phase separation procedure is explained in Section 2.4.5.

2.2.5 Tracer Particles

For PIV measurements, the carrier phase (i.e., the air in this case) needs to be seeded with tracer particles that are small enough to follow the flow, i.e., the particles need to have an adequate dynamic response to the fluid acceleration. However, the particles also need to be large enough to scatter the (light) energy from the laser light source sufficiently to form bright images that are recorded by the camera. The

specific size and the properties of the seed particles that are used should (ideally) be determined by the experiment to be performed, e.g., by the carrier-phase medium and the type of flow.

In the present experiments, mineral oil based tracer particles with a relatively small diameter of 0.2 μm were used as seed. The seed comprised a dense white mineral fog. Mineral oil was vaporized by adding nitrogen under high pressure and heating it. Thereafter, the hot vapor exited the heat exchanger through a nozzle, where it rapidly cooled when mixed with the ambient air, the cooling resulting in a condensation process. 95% of the seed particles were 0.2 μm in diameter, which was found by a calibration from the manufacturer. These particles were small enough to minimize particle tracking errors for the velocity gradients measured in these experiments, as discussed by Leishman [98]. The size, quantity, and distribution of seeding particles in the flow are important criteria for obtaining good data when performing PIV. Only if the flow is properly (i.e., uniformly) seeded, can good cross-correlations be obtained by the PIV algorithm; see Section 2.2.2.

2.3 Single-Phase Near-Wall Flow Measurements (0.816 m-Diameter Rotor)

To examine the boundary layer and the near-wall flow at the ground below a rotor operating in ground effect conditions, experiments with a 0.816 m-diameter rotor were performed. This rotor setup along with the instrumentation allowed

the near-wall region to be resolved with greater spatial detail (i.e., a finer spatial resolution) than was possible with the smaller rotor used in the second experiment (described later). Although this (larger) rotor experiment did not allow for dual-phase measurements to be performed, it gave valuable insight into the mean flow and turbulence characteristics over a ground plane below a rotor.

2.3.1 Setup and Test Conditions

The first experiment used a single-bladed rotor system with a rotor radius, R, of 0.408 m (1.339 ft) and a rectangular blade shape (NACA 2415 airfoil) with a chord, c, of 44.5 mm (1.75 in). The rotor was operated with the rotor disk plane at a height of one rotor radius above a circular ground plane to simulate hover-in-ground-effect conditions. The rotor blade was set to a blade pitch angle of 4.5°.

Flow measurements were made with the rotor operating at a rotational frequency of 31 Hz (1,860 rpm) and an angular velocity, Ω, of 195 rad s^{-1}, yielding a rotor tip speed, V_{tip}, of 78.85 m s^{-1} (258.69 ft s^{-1}). This rotor tip speed (or blade tip speed) yielded a blade tip chord Reynolds number of

$$Re_c = \frac{V_{tip} c}{\nu} = 250,000 \tag{2.3}$$

where ν = 1.5395 x 10^{-5} $m^2 s^{-1}$ is the kinematic viscosity of air at an ambient temperature of 23°C and ambient static pressure of 101,300 Pa, i.e., the environmental conditions in the laboratory when the experiments were performed.

The rotor thrust, T, was measured using a force balance between the motor and its stand; see Fig. 2.1. The thrust produced by the rotor was then normalized to obtain the non-dimensional thrust coefficient, C_T, and the blade loading coefficient, C_T/σ.

The rotor thrust coefficient is defined as

$$C_T = \frac{T}{\rho_f A(\Omega R)^2} \tag{2.4}$$

where A is the rotor disk area, $\rho_f = 1.191$ kg m^{-3} was the density of the air when the measurements were done, Ω is the angular velocity of the rotor, and R is the rotor radius. With the rotor solidity, σ, defined as

$$\sigma = \frac{N_b c}{\pi R} \tag{2.5}$$

where N_b is the number of blades of the rotor, the blade loading coefficient of the rotor was calculated to be $C_T/\sigma = 0.08$ in ground effect operation. The blade loading coefficient is an important parameter in the measurements of rotor flows because these flows generally contain blade tip vortices, and the blade loading coefficient is proportional to the strength of the tip vortices trailing from the rotor blades. The equation linking the strength of the tip vortex, Γ_v, to the rotor operational parameters is

$$\Gamma_v = k \left(\frac{C_T}{\sigma} \right) \Omega \, R \, c \tag{2.6}$$

with $k = 2$ based on the ideal blade loading in hover, and $k = 2.3$ as found

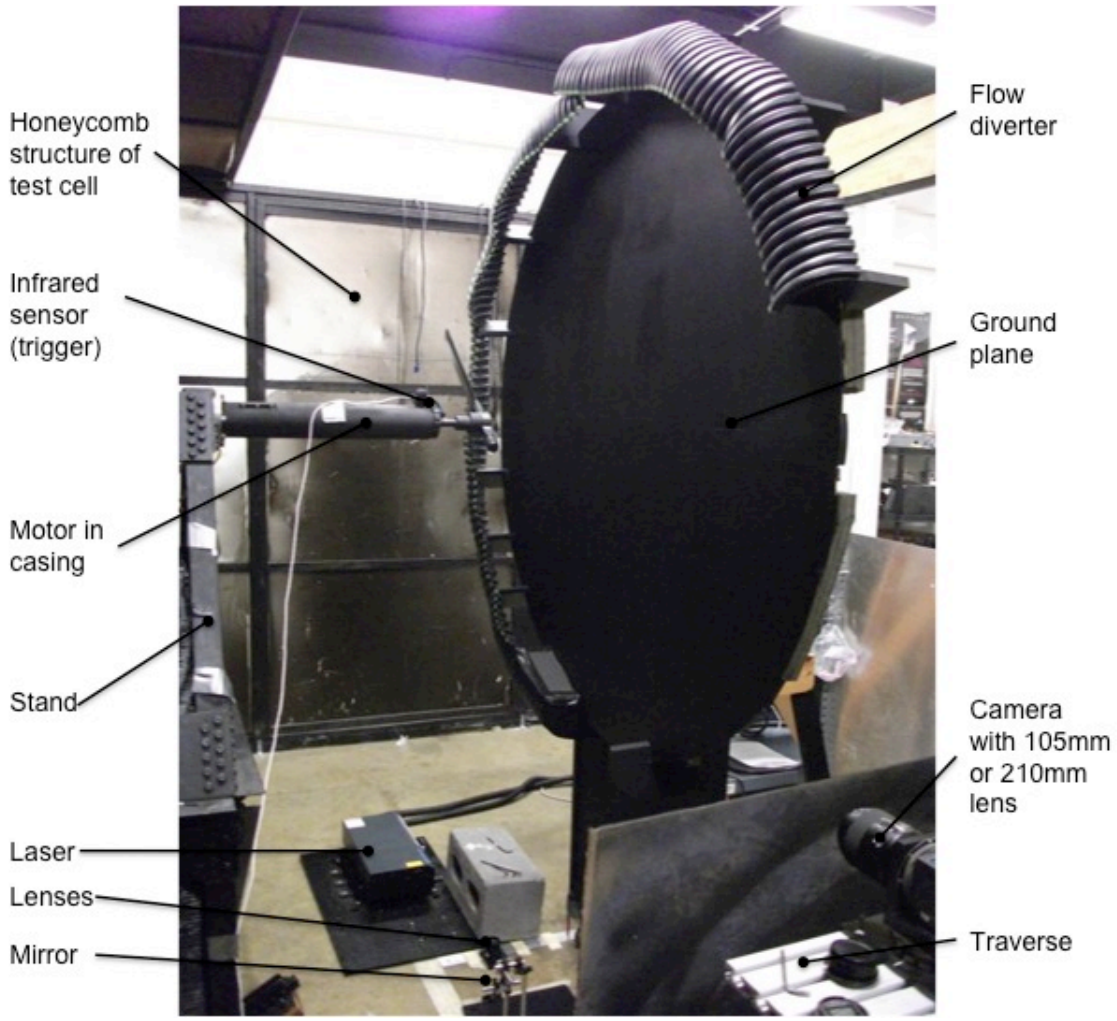

Figure 2.1: Photograph showing the test stand used for the 0.816 m-diameter rotor.

empirically [3].

One way to evaluate the vortex strength is by calculating the circulation from the measured velocity fields surrounding the tip vortices. The circulation, Γ_v, was calculated using

$$\Gamma_v = \oint_C \vec{v} \cdot d\vec{s} \tag{2.7}$$

In this case, C is the path completely enclosing the tip vortex in the plane in which the velocity field is measured, while also excluding any extraneous vorticity (e.g, induced by other vortices). The measured velocity field from the PIV results is $\vec{v}$, and $d\vec{s}$ is the directed line segment. The current blade loading coefficient produced a tip vortex with an estimated circulation (i.e., vortex strength) of $\Gamma_v = 0.5$ m^{2}s^{-1} (5.38 ft^{2}s^{-1}), giving a vortex Reynolds number, Re_v, of 32,000. The vortex Reynolds number was calculated using

$$Re_v = \frac{\Gamma_v}{\nu} \tag{2.8}$$

With the measured rotor thrust, the mean value of the hover induced velocity from rotor theory [3] was calculated using

$$v_h = \sqrt{\frac{T}{2\rho_f A}} \tag{2.9}$$

giving an average induced velocity, v_h, of 2.37 m s^{-1} (7.77 ft s^{-1}).

Because the mean flow over the ground plane at some distance away from the rotor shaft axis mimics a wall jet-like flow, the boundary layer Reynolds number in this case was defined as it is typical for a canonical wall jet, i.e., based on the maximum velocity of the wall jet, $u_{\max}$, and the wall-normal distance from the ground plane where this velocity maximum occurred, $z_{\max}$; see Fig. 2.2. Using these definitions, $u_{\max}$ and $z_{\max}$ were measured and the estimated boundary layer Reynolds

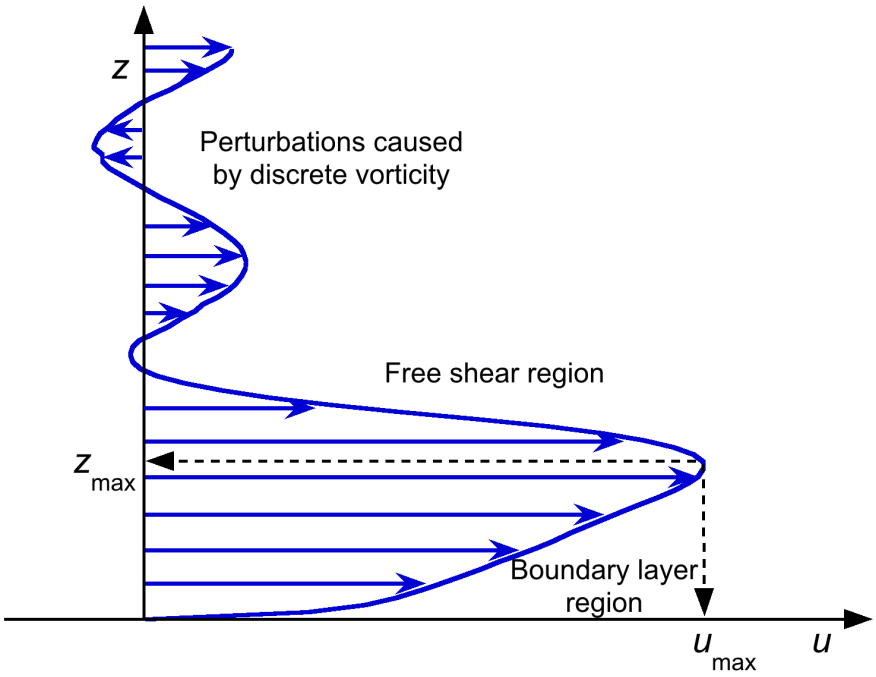

Figure 2.2: Representative mean flow profile in the near-wall region below a hovering rotor.

number at the ground below the rotor was

$$Re = \frac{u_{\max} z_{\max}}{\nu} = 3,000 \tag{2.10}$$

There are several reasons why a single-bladed rotor was used, and various authors have already pointed out the advantages of such a single-bladed rotor system for studying the characteristics of the tip vortex [57, 99, 100]. For the purpose of investigating single tip vortices and their behavior as they approach the ground, it is advantageous to avoid vortex–vortex interactions, at least in the first instance. This is best done using a single-bladed rotor system in such that there is no interference of

one vortex with another vortex generated by the other blade. Furthermore, a single helicoidal vortex is spatially as well as temporally much more stable than several interacting vortices. Because the vortices are more stable, they can persist in the flow to older wake ages, which is advantageous for the present studies where the behavior of the rotor wake near the ground at older wake ages was a primary focus.

The rotor was powered by a three-phase electric motor. Figure 2.1 shows the setup with the stand the motor was mounted on, and the rotor blade with its counter-weight being situated on the motor shaft. The counter-weight on the other side of the rotor hub was necessary to balance the mass of the single blade. Parts that could produce reflections were painted black to minimize these reflections.

2.3.2 Test Cell and Ground Plane

The test cell shown in Fig. 2.3 had a volume of approximately 250 m^3 (8,820 ft^3) and was large enough to avoid flow recirculation during the duration of the tests, as was confirmed by means of flow visualization. To further minimize flow recirculation in the test cell, flow diverters were mounted around the edge of the circular ground plane so as to control the radial flow when it exited off the surface. Honeycomb-structured flow conditioning screens were located upstream of the rotor to reduce incoming turbulence levels. The seeding (see Section 2.2.5) was delivered through a tubing system to the location where it was required, and it was introduced into the main rotor flow through small holes in a pipe to uniformly disperse the seed particles

Figure 2.3: Photograph showing the test cell for the 0.816 m-diameter rotor system.

in the flow.

The ground plane was made of plywood and painted with a flat black paint to minimize surface reflections. To alleviate these laser light reflections from the ground plane, tangential illumination was used, i.e., the light sheet was aligned such that the centerline of the sheet was parallel to the ground plane. Reflections can be an issue when high-energy laser light is directed at surfaces, producing flare and so making it difficult or even impossible to obtain high-quality flow measurements at or

near these surfaces. A photograph of the setup showing how the motor on the stand, the rotor, and the ground plane were arranged with respect to each other is given in Fig. 2.1.

The ground plane was oriented vertically and mounted on a gantry in this case. A vertical orientation has the advantage that the ground plane can be moved easily towards and away from the rotor plane, so as to decrease or increase the rotor height off the ground. In the present experiments, however, the distance between the rotor plane and the ground plane was held constant at one rotor radius.

2.3.3 Instrumentation

The light sheet from a double-pulse Nd:YAG laser with a wave length of 532 nm and an energy of 150 mJ per pulse was aligned with its plane parallel to the rotor shaft axis so as to illuminate the regions of interest (ROI). A schematic of the setup showing the most important hardware components is given in Fig. 2.4, also illustrating how the laser light sheet, camera, rotor, and ground plane are arranged with respect to each other.

The lasers were fired at a high-intensity-rated mirror, deflecting it by 90° into a cylindrical and a spherical lens connected in series; see Fig. 2.4. The cylindrical lens expanded the laser beam in one direction (i.e., into a plane) before the spherical lens reduced this laser sheet to the desired thickness. The ROIs all lie in the plane of this light sheet. The light sheet was measured to have a thickness of 1 mm in the

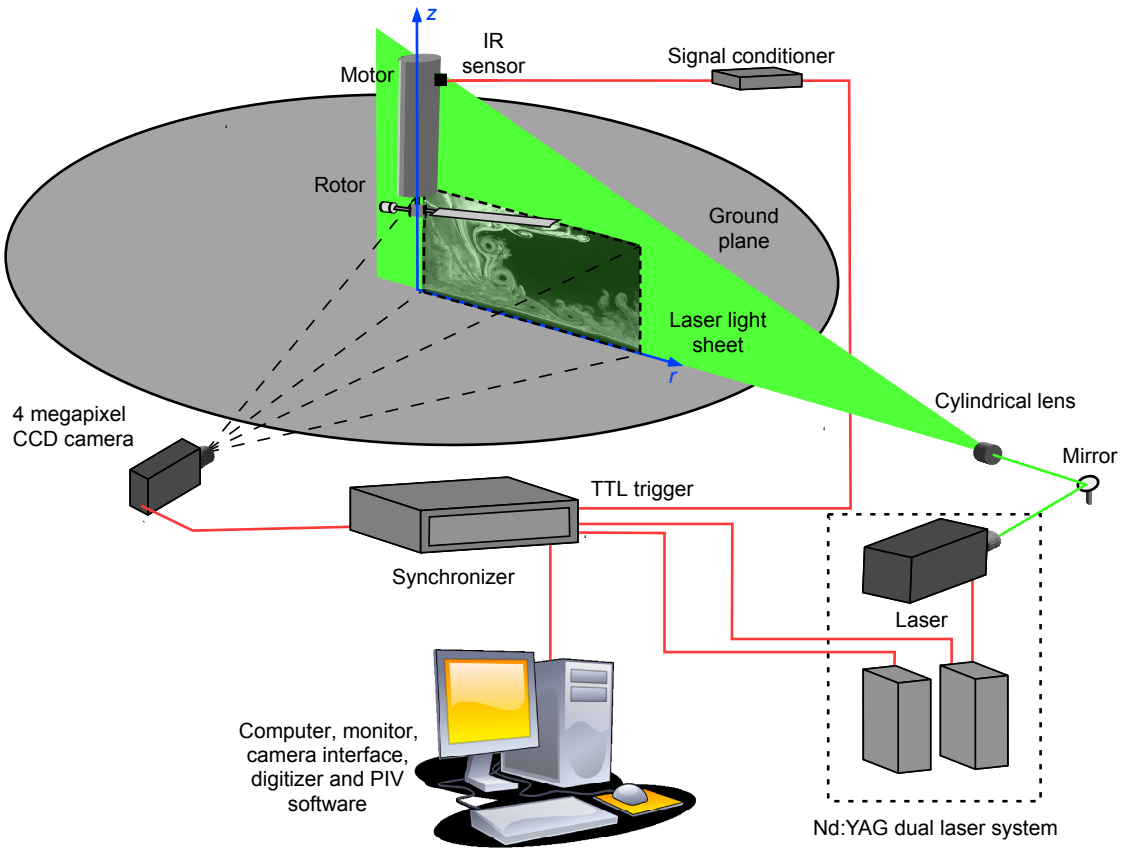

Figure 2.4: Schematic of the experimental setup showing the single-bladed rotor and the circular ground plane.

measurement domain (i.e., the investigated ROIs). A relatively thin laser light sheet is important for having a sufficiently concentrated light intensity, allowing the tracer particles to scatter enough light for successful cross-correlations in the PIV images.

The flow was seeded using mineral oil particles with a mean diameter of 0.2 μm; also see Section 2.2.5. The 4 Megapixel charge-coupled device (CCD) camera had the capability of capturing 15 frames per second (fps) at its maximum resolution of

2,048 x 2,048 pixels. The viewing axis of the camera was oriented to be orthogonal to the plane of the light sheet, which is also the imaging plane the camera was focused on. This 4 Megapixel CCD camera gave good spatial resolution well into the boundary layer regions at the ground, so that small-scale flow structures such as turbulent eddies in the near-wall flow could be resolved. In ROI 5, measurements could be obtained as close as 0.002 z/R off the ground when using a 105 mm lens with an f$^{\#}$ of 2.8. For ROI 6, a 210 mm lens set to an f$^{\#}$ of 5.6 was used, allowing for measurements as close as 0.001 z/R off the ground.

The spatial locations of the ROIs with respect to the rotor and the ground plane are shown in Fig. 2.5. Separate interrogation regions were needed to track the

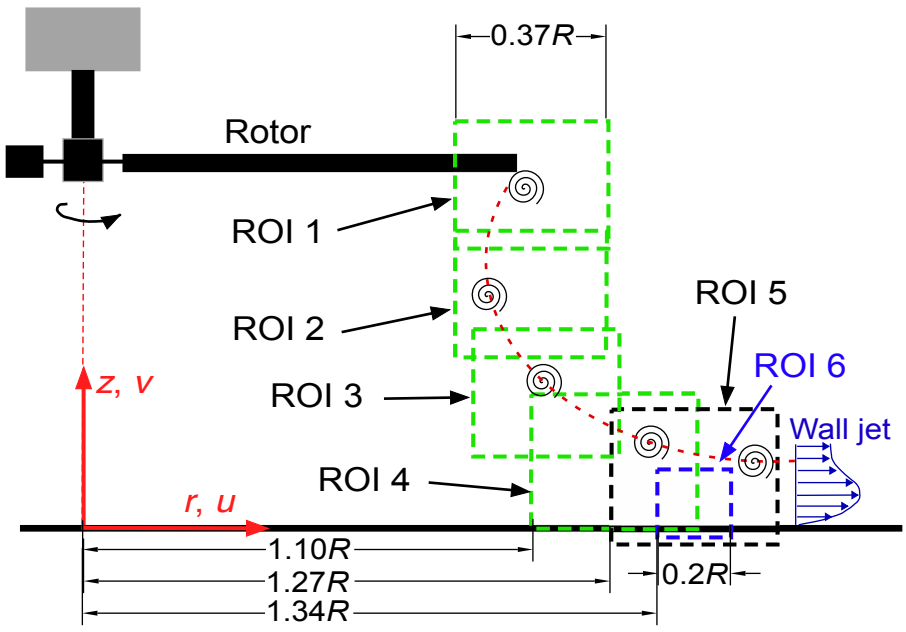

Figure 2.5: Schematic showing the regions of interest (ROIs) used to measure the single-phase flow produced by the 0.816 m-diameter rotor system.

rotor wake down to the ground plane so as to retain the necessary spatial resolution in the measurements. The regions analyzed in the present work were in ROI 5 and 6 (see Fig. 2.5) because these regions best exposed the rotor wake–ground interactions and the developing near-wall flow over the ground plane.

For ROI 5, the spatial resolution, L_m, was 73.53 μm per pixel, corresponding to a 0.882 mm vector spacing. A smaller 0.294 mm vector spacing was obtained in the wall-normal direction in the boundary layer region because of the smaller, rectangular-shaped interrogation windows used there. The spatial resolution for ROI 6 was 38.46 μm per pixel corresponding to a 0.308 mm vector spacing (0.154 mm in wall-normal direction in the boundary layer region). For accurate vortex measurements, the requirement of $L_m/r_c < 0.2$ was established [23]. This ratio was evaluated to be $L_m/r_c = 0.14$ for the measurements above the boundary-layer region at the ground plane below the rotor, and $L_m/r_c = 0.07$ inside the boundary-layer region. The root-mean-square (rms) error of the particle displacement was estimated to be 0.05 pixels in ROI 5 and 0.12 pixels in ROI 6.

2.3.4 Timing and Synchronization

Because the rotor operated at a rotational frequency of 31 Hz and the maximum imaging rate of the system was only 15 Hz, it was necessary to properly synchronize the rotor and imaging system. An infrared (IR) sensor was used as a tachometer to measure the rotational frequency of the rotor. Using an electronic circuit, the

one-per-rev signal produced by the rotor with the IR sensor was converted into a TTL pulse that was used by a digital synchronizer to synchronize the camera, laser, and rotor to each other. This instrumentation also allowed a phase delay to be introduced so that the rotor wake could be imaged at any desired azimuthal position of the rotor blade, ψ_b; see Fig. 2.6. In the present work, the blade azimuth angle is defined to be $\psi_b = 0°$ when the quarter-chord line of the blade axis passes through the plane of the laser light sheet; see Fig. 2.4.

The setup permitted the rotor wake and its blade tip vortices to be studied as a function of wake age, ζ. The wake age is a measure of time, and it is often referred to as "rotor time." By measuring ψ_b, the wake age of a single flow realization can be

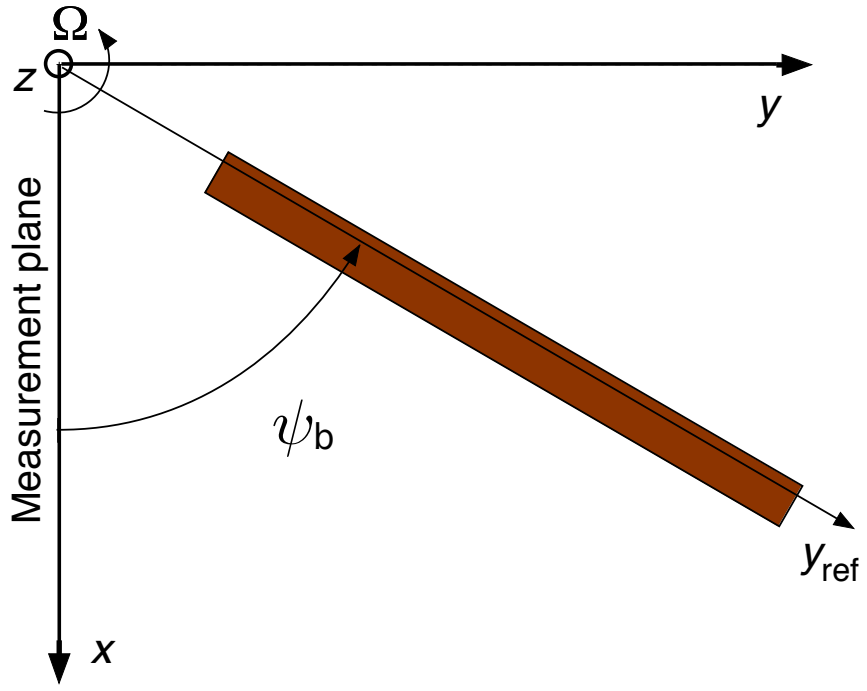

Figure 2.6: Schematic showing how the blade azimuth angle, ψ_b, is defined.

determined in degrees of blade rotation elapsed since the wake was generated by this rotor blade. For example, the wake age of a flow feature (e.g., a tip vortex) is the time (in degrees of rotor rotation) that has passed between the current realization and the point in time this flow feature was formed at the blade. The relation between ζ and ψ_b can be expressed by

$$\zeta = \psi_b + \left(\frac{360^\circ}{N_b}\right) i \ , \quad i = 0, 1, 2, 3, ... \tag{2.11}$$

with the index i indicating a segment of the tip vortex. In this case of the one-bladed rotor, as shown in Fig. 2.5, if the current blade azimuth angle (at which the image was taken) is $\psi_b = 30^\circ$, then the segment of the tip vortex located closest to the blade in this instantaneous realization has a wake age of $\zeta = 30^\circ$ (for $i = 0$), and the next segment of the older part of the vortex (further downstream in the flow) has a wake age of $\zeta = 390^\circ$ (for $i = 1$).

In the present experiment, phase-locked measurements were performed and the blade phase angle (or azimuth angle) was locked at eight azimuthal positions of the rotor blade (every 45°) with 100 PIV image pairs being recorded per azimuth, giving 800 image pairs for use in the time-averaging of the flow quantities.

2.3.5 PIV Image Acquisition and Processing

PIV was performed in the regions of interest (ROIs) indicated in Fig. 2.5. The dual laser system was fired such that the laser pulses were separated in time by

$\Delta t = 10\mu$s in ROIs 1, 2, 3 and 6, and by $\Delta t = 20\mu$s in ROIs 4 and 5. The reason for increasing the pulse separation time was that the flow velocities decreased when approaching the ground, and as a consequence, the tracer particles traveled a shorter distance between two consecutive PIV images that are correlated. Therefore, the value of Δt was increased, allowing for larger tracer particle displacements, and so giving an optimal displacement between the two consecutive images.

For a given interrogation window size, the chosen pulse separation time (reported previously) resulted in the desired maximum particle displacements (about one-quarter of the interrogation window size, following the well-established "one-quarter rule"). In general, the tracer particle displacement should be enough for the particles to move a small but distinguishable distance (i.e., > 1 pixel) in the flow. However, the average displacement should not be too large (i.e., smaller than one-quarter of the dimensions of the interrogation window), otherwise tracer particles moving out of the interrogation window can cause a significant loss of correlation in the PIV image pair. Furthermore, if the laser pulse separation time is set too large, flow curvature effects can introduce significant errors in the calculation of the velocities for a vortically-dominated flow. This outcome is because the local velocity vector is calculated based on the (shortest possible) distance a tracer particle traveled between the first and second image.

There were two reasons why multiple ROIs were needed to obtain the measurements in the rotor wake (see Fig. 2.5). First, with the 4 Megapixel CCD camera, the field of view had to be reduced to obtain fine enough spatial resolution. Second, the laser was not powerful enough to produce a light sheet with sufficiently high

intensity if covering the whole rotor wake at one time. Therefore, the measurements had to be performed in smaller areas of the flow.

The position of the ROIs (i.e., the fields of view of the camera) were measured with respect to the rotor coordinates, and so the images were spatially calibrated. Measurements were taken in all six ROIs, but only ROIs 5 and 6 were analyzed in detail because in these regions the most intense rotor wake–ground interactions were observed; the near-wall flow and its turbulence characteristics were a major focus of the present study. As mentioned in Section 2.3.3, the better spatial resolution of the flow obtained in ROI 6 was made possible by using a 210 mm lens instead of the 105 mm lens used for ROI 5, yielding about twice the magnification for ROI 6 (compared to ROI 5). The 105 mm lens (ROI 5) was set to an $f^{\#}$ of 2.8, while the 210 mm lens used with ROI 6 was set to an $f^{\#}$ of 5.6.

The final interrogation window size was chosen to be 24 x 24 pixels for ROI 5, yielding a spatial resolution with enough measurement points within the tip vortex core to spatially resolve the steep velocity gradients. An image deformation method [101] with a 50% window overlap was used. Each image pair was processed so that the whole image, i.e., the whole region of interest, was split into interrogation windows of the size of 48 x 48 pixels, with a final window size of 24 x 24 pixels. A standard multigrid, multipass, cross-correlation PIV algorithm was used with two passes on each of the mentioned interrogation grid sizes.

In processing the data, the Rohaly-Hart method [102] was implemented and a local vector validation, using 3 x 3 neighboring vectors with a universal median test was applied. Thereafter, the data were processed through intermediate vector

conditioning, using 3 x 3 neighboring vectors as well, but with a local mean in this case. Spurious vectors were determined using a Gaussian peak with a signal-to-noise ratio of 1.5. To avoid distorting the results, images containing more than 5% of spurious or interpolated vectors were removed from further analysis. However, rejected images were found to be less than 2% of the total images that had been acquired.

To adequately resolve the higher velocity gradients in the wall-normal direction, the length of the wall-normal edge of the interrogation windows near the wall (or ground plane) was adjusted to 8 pixels. This process allowed for a higher spatial resolution in the wall-normal direction, i.e., where it is needed to fully resolve the velocity gradients in the boundary layer over the ground plane. Furthermore, the refined spatial resolution permitted the small spatial variations in the flow quantities to be resolved within the boundary layer. The wall-parallel particle displacements were much higher than those in the wall-normal direction, which is the result of the near-wall flow being largely aligned in wall-parallel direction. The relatively large wall-parallel particle displacements (of about 6 pixels) made it necessary to use a wall-parallel length of 24 pixels for the interrogation windows, resulting in rectangular-shaped interrogation windows of 8 x 24 pixels.

In ROI 6, the PIV images were processed with the same settings as previously described for ROI 5, except that the grid for the near-wall zone was reduced to a size of 8 x 16 pixels for each interrogation window, and the vortical region of the flow (i.e., the outer flow) used a 16 x 16 pixel window size. The reason for decreasing the window sizes was to better resolve the flow with its small-scale turbulent

flow structures in this smaller ROI, also using twice the optical magnification and so yielding about twice the spatial resolution compared to ROI 5. As reported previously, the spatial resolution in ROI 5 was 73.53 μm per pixel compared to 38.46 μm per pixel in ROI 6. The pulse separation time, Δt, was reduced to 10 μs in ROI 6 (compared to 20 μs used in ROI 5) to achieve optimal particle displacements.

2.4 Dual-Phase Rotor Flow Measurements (0.17 m-Diameter Rotor)

The previously described experimental setup with the 0.816 m-diameter rotor system gave good insight into the near-wall flow. However, experimental size constraints with this setup did not permit dual-phase flow measurements. Therefore, another set of experiments was performed using a smaller rotor system to perform comparative single-phase and dual-phase measurements. A rotor of relatively small dimensions was chosen because of the need to confine the particle flow within a test cell while avoiding recirculation of the flow (i.e., wall effects); see Section 2.4.2. With this 0.17 m-diameter rotor system, flow measurements were performed using PIV for the single-phase flow and for the carrier phase in the dual-phase experiments. PTV methods were used to measure the displacements and velocities of the sediment particles in the dispersed phase, as described in Sections 2.2.3 and 2.4.4.

2.4.1 Setup and Test Conditions

A two-bladed rotor system with a rotor radius, R, of 0.085 m (0.279 ft) was used for these experiments. The rotor blades used thin airfoils (with camber and a sharpened leading edge) of rectangular planform with a chord, c, of 0.018 m (0.059 ft). The rotational plane of the rotor was located at a height of $1R$ above a ground plane. The ground plane was covered with a mobile sediment bed for the dual-phase tests; see Fig. 2.7.

Comparative single-phase (i.e., carrier flow without sediment particles) and dual-phase (i.e., flow with particles) experiments were performed with the rotor being run at the same operational conditions. These conditions were chosen so as

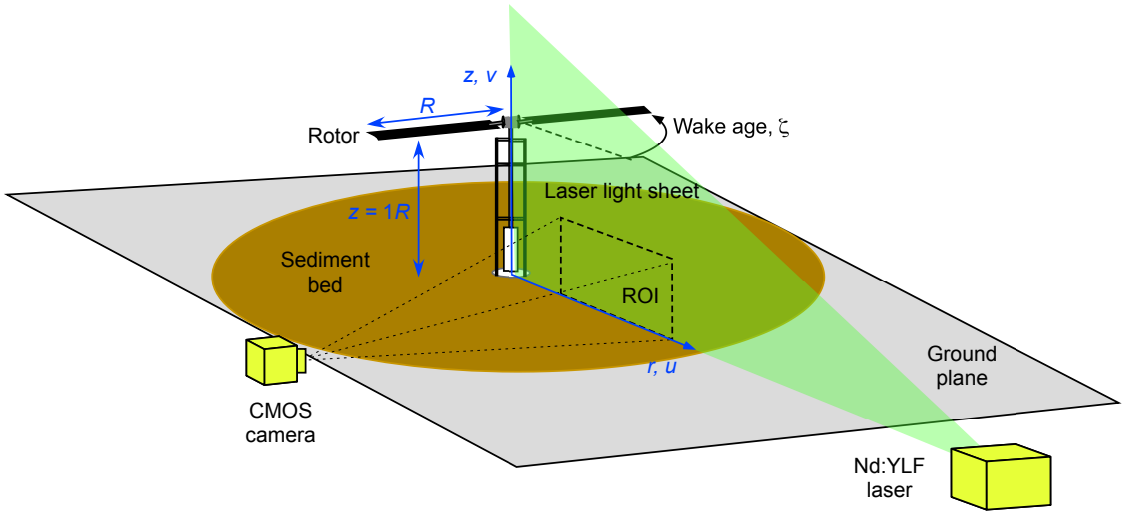

Figure 2.7: Schematic of the experimental setup used with the 0.17 m-diameter rotor system to conduct both single-phase and dual-phase flow measurements.

to generate a rotor wake with high enough flow velocities to mobilize and uplift particles of sufficient size to allow for good discrimination of the flow phases in the resulting dual-phase flow. However, the flow velocities produced by the rotor still had to be small enough to avoid significant depletion of the sediment bed, although some erosion of the bed surface is inevitable. However, because of the small amplitude and long wavelength of the bed deformations, together with the relatively short testing (or recording) period (i.e., 1.38 s), these bed deformations were small.

The rotor was operated at a rotational frequency of 60 Hz (3,600 rpm), which corresponded to a blade tip speed of 32.04 m s^{-1} (105.12 ft s^{-1}) and a chord Reynolds number, Re_c, at the blade tip of approximately 35,000 using Eq. 2.3. The collective blade pitch of the rotor was set to 12° to produce a representative rotor wake and a rotor thrust that allowed for good dual-phase measurements (e.g., mobilizing sediment particles while avoiding rapid bed depletion by operating at too high a thrust). A microbalance was used to measure the rotor thrust, T. The blade loading coefficient, C_T/σ, was determined to be 0.156 using Eqs. 2.4 and 2.5.

With the measured rotor thrust, the hover induced velocity from rotor theory [3] was also calculated using Eq. 2.9, giving a velocity, v_h, of 3.3 m s^{-1} (10.8 ft s^{-1}). The circulation of the tip vortices (used to characterize the vortex strength) was determined to be $\Gamma_v = 0.0172$ $m^2 s^{-1}$ using Eq. 2.7. With this circulation, the vortex Reynolds number could then be calculated from Eq. 2.8, giving $Re_v = 1{,}100$ for the tip vortex generated by the 0.17 m-diameter rotor system.

Because the mean flow over the ground plane generated by the rotor is essentially a wall jet-like flow (as will be discussed), the boundary layer Reynolds number in this

case was defined as for a canonical wall jet; see previously in Fig. 2.2. The estimated boundary layer Reynolds number over the ground plane with the 0.17 m-diameter rotor system was

$$Re = \frac{u_{\max} z_{\max}}{\nu} = 7,000 \tag{2.12}$$

The motor powering the rotor was a precision brushless direct current (DC) motor. A Hall-effect sensor was mounted on the support structure and a magnet attached to the rotor shaft. When the Hall-effect sensor passed through the magnetic field, it generated a one-per-rev signal. This signal was used to control the rotational speed of the rotor (i.e., serving as a tachometer) by adjusting the input voltage to the motor. Furthermore, the signal from the Hall-effect sensor was also used to synchronize the rotor, camera, and laser to each other, so as to allow the rotor wake to be studied in terms of wake age. The wake age was previously explained in Section 2.3.4 and it is also depicted in Fig. 2.7. The motor was placed inside a flat-black cowling to protect it from the heat produced by the laser light and also to minimize laser reflections.

To simulate ground-effect conditions, a flat circular ground plane made of hardened thermoplastic resin was mounted on a support; see Fig. 2.8. The ground plane was painted flat black to reduce reflections form the incident laser light, which can hinder PIV measurements near solid surfaces. This experimental challenge is discussed in more detail in Section 2.4.5. The height of the rotor was held constant at one rotor radius above the ground plane; see Fig. 2.7.

2.4.2 Dust Chamber

The experiments with this (smaller) rotor setup were performed inside a test cell or "dust chamber," as shown in Fig. 2.8. This chamber provided a controlled environment for conducting both the single-phase and the dual-phase flow experiments, and it also fully contained any suspended dust particles during the dual-phase tests. All sensitive optical instrumentation (i.e., laser, camera, etc.) was operated outside of the dust chamber so that it would not be contaminated or damaged by the sediment particles; see Fig. 2.9.

The dust chamber used slotted aluminum beams for the frame, and optically clear plexiglas walls for the windows; see Fig. 2.8. The dimensions of the dust chamber were 2 m x 2 m x 2 m. Clear plexiglas walls on all sides provided good optical access to the test section, giving minimal laser light attenuation and an unobstructed view of the test section. Some sections inside the dust chamber were covered with thick, non-reflective black cloth to minimize background laser light reflections.

The dust chamber was equipped with a ventilation system so as to control the concentration of seed particles within the chamber, and to evacuate suspended dust particles between experiments; see Figs. 2.8 and 2.9. The seeding input vent was installed at the center of the ceiling. When entering the chamber, the tracer particles passed through a honeycomb flow straightener to reduce turbulence in the

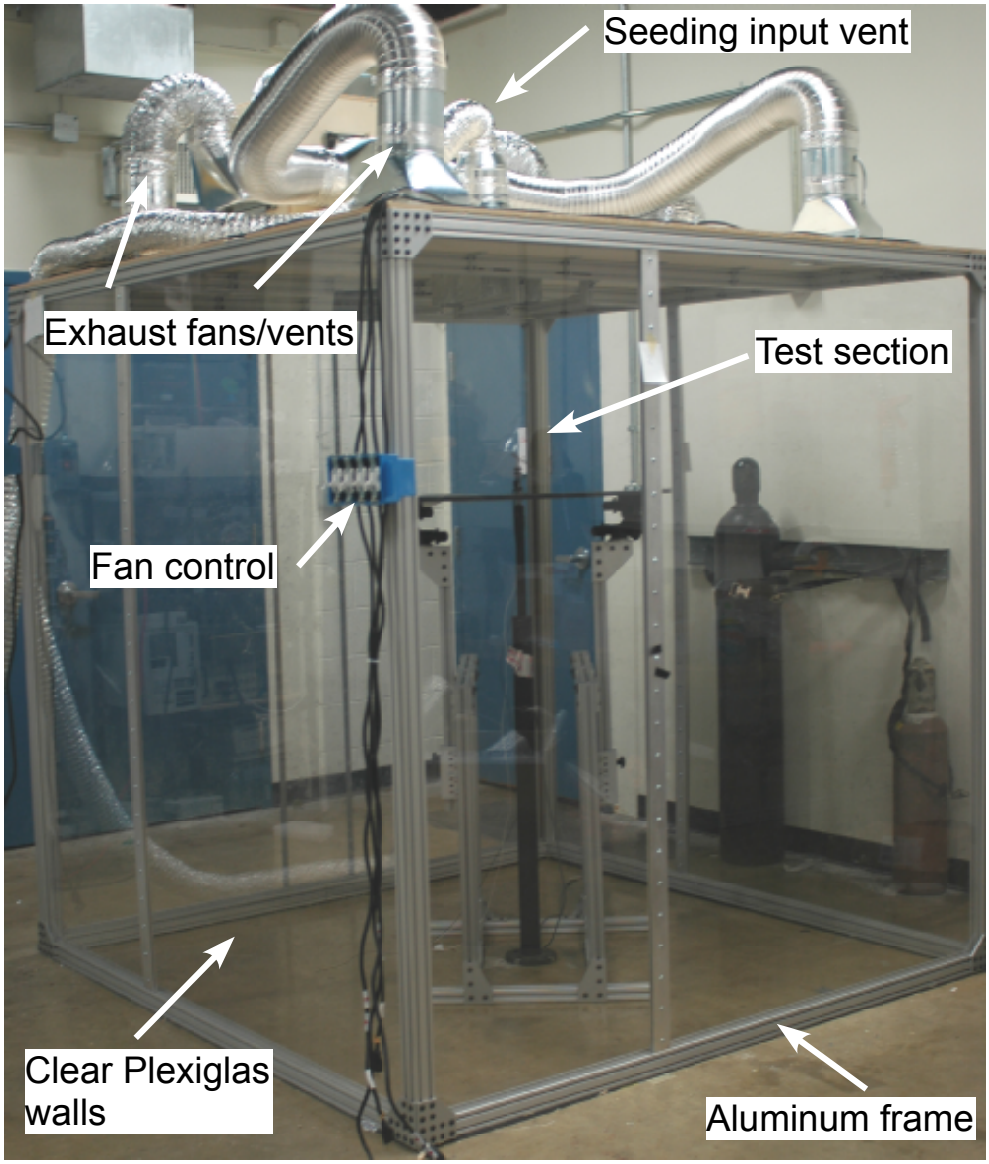

Figure 2.8: The dust chamber inside which both the single-phase and dual-phase flow experiments with the 0.17 m-diameter rotor were performed.

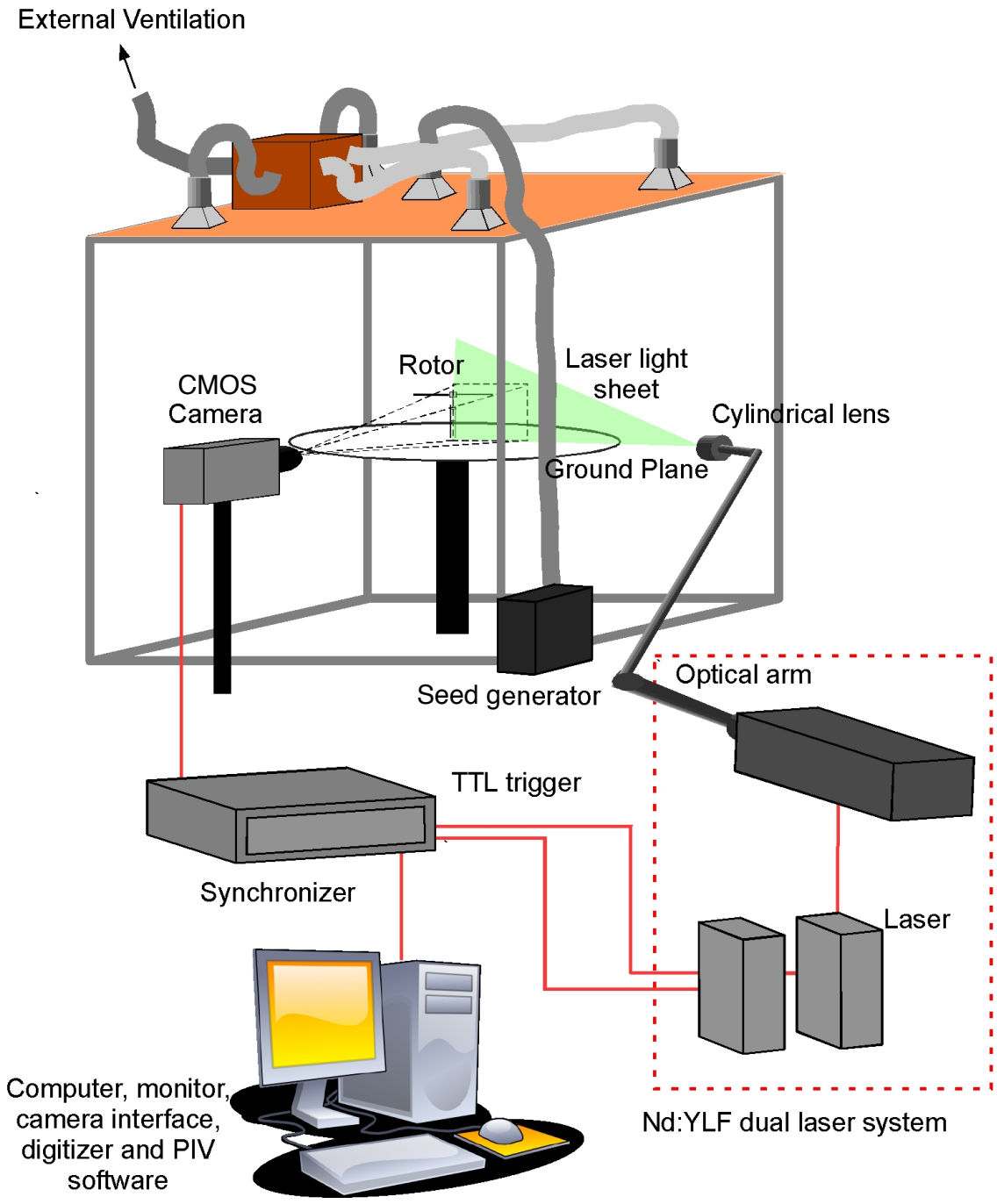

Figure 2.9: Schematic of the dust chamber and the instrumentation that was used with the 0.17 m-diameter rotor setup.

flow. For ventilation and evacuation of the seed particles from the test cell, four exhaust fans/vents were installed on the ceiling of the dust chamber.

The ratio of the length of one edge of the dust chamber (i.e., 2 m) to the rotor radius was approximately 24. That is, the rotor was located at a distance of about $12R$ from each of the walls. The relatively small size of the rotor (and so a relatively small wake flow field) relative to the 8 m^3 volume of the test cell was sufficient to minimize flow recirculation for the duration of each test, and so wall interference effects could be neglected.

2.4.3 Dispersed-Phase (Sediment) Particles

For the dual-phase flow experiments, sediment particles consisting of well-characterized soda-lime glass microspheres ($\rho_p = 2,238$ kg m^{-3}) were loosely deposited on the ground plane in a bed below the rotor. This sediment bed had a thickness of about 10 mm and the surface was made smooth with a scraper. The glass microspheres had diameters in the range of $d_p = 45$–63 μm because these sizes are representative of the sizes of uplifted particles typically found in the dust cloud produced by a helicopter encountering brownout conditions [103]. These particles were also previously found [2] to have good mobility such that they could be uplifted by the laboratory-scale rotor flow and produce a dusty flow environment that was qualitatively similar to the brownout dust clouds seen in the field [103].

Spherical particles were used for the experiments, so that numerical simulations

could be validated by the experimental results; most numerical brownout simulations use spherical particles in their assumptions. The particle size distribution of the sediment particles was further characterized using laser light scattering measurements that gave a mean diameter of 54.61 μm [104]; see also Fig. 2.10.

The Stokes number is defined as

$$St = \frac{\tau_p}{\tau_f} \tag{2.13}$$

where τ_f is the characteristic fluid time scale. In this case, τ_f was based on the peak-to-peak velocity across the vortex and the diameter of the vortex core, d_c, before the vortex significantly interacted with the ground plane ($d_c \approx 6$ mm). τ_p is the Stokes time scale or particle relaxation time, i.e., the time a particle at rest needs to reach $1/e$ of the velocity of the surrounding fluid. τ_p was calculated using

$$St = \frac{\rho_p d_p^2}{18 \rho_f \nu} \tag{2.14}$$

with the mean particle diameter, d_p, which was measured to be 54.61 μm. The carrier-phase medium was air with $\nu = 1.5395$ x 10^{-5} $\mathrm{m^2 s^{-1}}$ and $\rho_f = 1.191$ kg $\mathrm{m^{-3}}$ at an ambient temperature of 23°C and ambient static pressure of 101,300 Pa. The Stokes number was estimated to be 60, and the particle Reynolds number was less than 30. A particle Reynolds number in this order of magnitude is too low for vortex shedding to occur behind the particles, which was previously reported to produce additional turbulence in the flow [105].

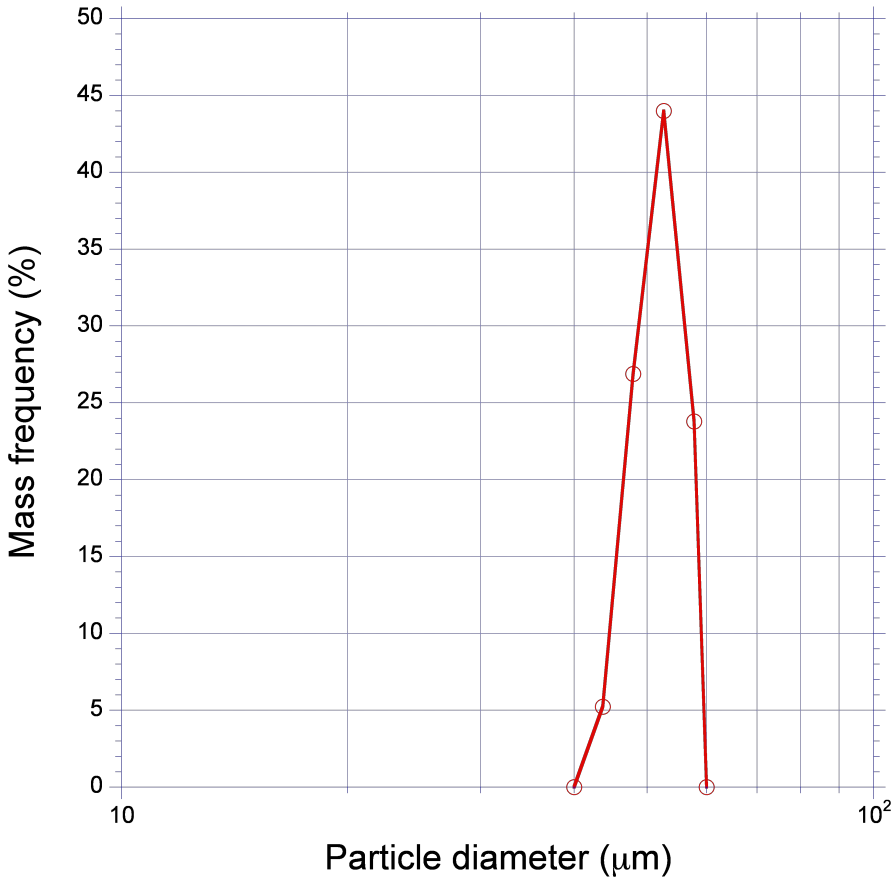

Figure 2.10: Particle size distribution of the sediment particles being used.

2.4.4 Optical Measurement Equipment and Image Acquisition

A Nd:YLF double-pulsed laser system was used as the light source to illuminate the flow in the desired ROI; see Fig. 2.7. The laser beam was directed through a series of cylindrical and spherical lenses to diverge into a thin laser light sheet with a thickness of about 1 mm. This light sheet was aligned with the ground plane so as to minimize reflections from the ground plane and the sediment bed. In all cases, tangential illumination proved to be most beneficial, i.e., the light sheet was aligned

such that the centerline of the sheet was parallel to the ground plane. The viewing axis of the camera was then aligned to be orthogonal to the plane of the laser light sheet and it was focused on the desired ROIs in this plane; see Figs. 2.7 and 2.11. All of the optical measurement equipment was located outside of the dust chamber to avoid contamination by the particles; see Section 2.4.2.

The high-repetition rate Nd:YLF laser (20 mJ per pulse) was operated at a repetition rate of 1,000 Hz together with a 1 Megapixel complementary metal-oxide semiconductor (CMOS) camera, which allowed for a contiguous time-history of the flow to be recorded. The CMOS chip of the camera had a size of 1,024 x 1,024 pixels. Both of the flow phases were recorded by the same camera before the raw images containing the two phases were processed separately; see Section 2.4.5.

Temporally resolving the flow is essential to the understanding of the turbulent

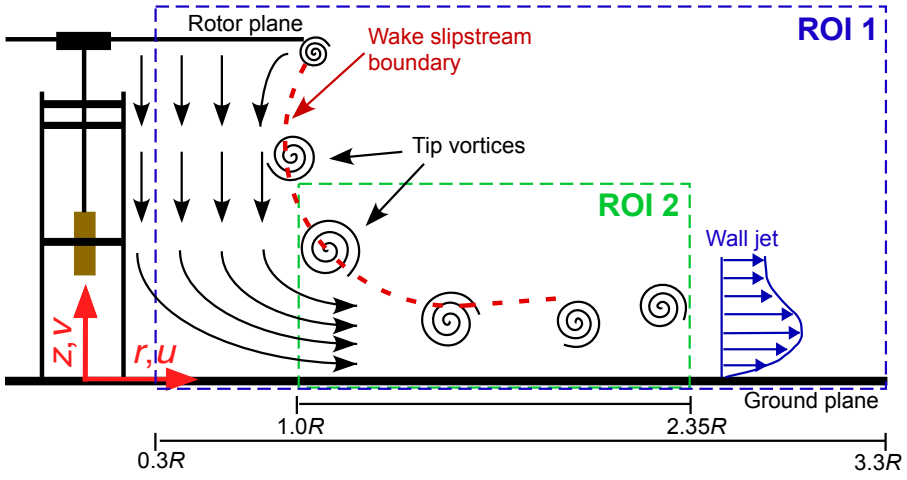

Figure 2.11: Schematic showing the ROIs used to measure both the single-phase and the dual-phase flows produced by the 0.17 m-diameter rotor system.

nature of the vortical flow present in the wake of a rotor operating in ground effect. The chosen temporal resolution for interrogating the flow was ultimately a balance between the temporal resolution needed to track the individual vortical structures and sediment particles, and the image intensity that was needed to enable successful cross-correlations with the PIV measurements. In this case, 500 contiguous image pairs were obtained for the single-phase flow (without the sediment) and for the dual-phase flow under the otherwise identical external flow conditions; this recording time corresponded to 30 revolutions of the rotor.

A 105 mm lens (set to an $f^{\#}$ of 2.8) was used to obtain a field of view that was large enough to track the vortices from their formation at the blade tips, through their interactions with the sediment bed, and to their further evolution as they convected away from the rotor near the ground plane. To capture the incipient particle motion, transport, uplift and suspension, the significant ROI was ROI 1; see Fig. 2.11. For more detailed investigations, the camera was focused on a subregion of ROI 2 that produced good evidence of the vortex flow–particle bed interactions. In this case, a 200 mm lens with an $f^{\#}$ of 4 was used.

The spatial resolution of the measurements obtained with the (larger) 0.816 m-diameter rotor setup (described previously) had to be traded (to some extent) for good temporal resolution while still obtaining a large enough field of view to capture the incipient motion, transport, uplift and suspension of the particles. The spatial resolution was 78.13 μm per pixel (0.938 mm vector spacing) for the region of interest on which the 1 Megapixel CMOS camera was focused (ROI 2); see Fig. 2.11.

With the current instrumentation, the rms error of the particle displacements

was estimated to be 0.04 pixels, which is in the same order as the measurement accuracy reported in comparable time-resolved dual-phase PIV measurements [106]. The measurement accuracy of the single-phase and dual-phase PIV measurements were the same because the same setup, instrumentation, test conditions, and analysis algorithms were used. Because of a relatively dilute distribution of dispersed-phase particles the overall noise levels did not increase significantly. Furthermore, any blockage effects in the interrogation windows by the dispersed particles and the subsequent loss of correlation in the PIV measurements could be considered negligible.

The laser pulse separation time was set to 70 μs for ROI 1 and 50 μs for ROI 2, which, in this case, was a good compromise for measuring accurately both the particle displacements in the dispersed phase and the carrier-phase (tracer particle) displacements, while also minimizing the out-of-plane loss of correlation. The acquisition time scale was more than six times smaller than the fluid time scale for the measurements made in ROI 2, and more than four times smaller for the measurements made in ROI 1.

A second set of single-phase and dual-phase flow measurements were obtained using the test facility (dust chamber) and 0.17 m-diameter rotor system that were described previously in Section 2.4.1, also running at identical rotor operational parameters. The same Nd:YLF laser was used (20 mJ per pulse), but in this case with a 4 Megapixel CMOS camera. This CMOS camera allowed for a greater spatial resolution to be obtained in the measurements while maintaining the relatively large size of the ROIs to measure the flow fields (as shown previously in Fig. 2.11). The 4 Megapixel CMOS camera had the capability to record PIV image pairs of 2,560 x

1,600 pixels at a rate of 725 frames per second. A 105 mm lens (set to an f# of 2.8) was used to obtain the measurements in ROI 1, and a 200 mm lens (set to an f# of 4) was used with ROI 2; see Fig. 2.11.

In this case, 1,000 contiguous image pairs were obtained for both the single-phase and the dual-phase measurements, which gave a time-history of the flows corresponding to 83 rotor revolutions. Again, the single-phase and the dual-phase flow measurements were performed under identical external flow conditions and identical rotor operational parameters (see Section 2.4.1) to have a valid comparison of the two flows (i.e., with and without sediment particles in the flow). Such identical experimental conditions are a prerequisite for a proper assessment of the detailed flow phase couplings, and possible mean flow and turbulence modifications to the fluid flow by the dispersed particles.

Because the rotor was operating in ground effect, the vortices formed at the tips of the rotor blades persisted in the rotor wake by virtue of vortex stretching [25] until they were relatively old, i.e., wake ages of 4–6 rotor revolutions and until they were at downstream distances over the bed of 2–3R. Therefore, the use of a rectangular 2,560 x 1,600 pixel chip size (10μm pixel pitch) of the 4 Megapixel CMOS camera proved to be very beneficial, i.e., an optimum spatial resolution could be achieved for the regions of current interest. This camera and the size of the interrogated fields of view yielded a spatial resolution of 99.108 μm per pixel (0.793 mm vector spacing) in ROI 1, and a finer spatial resolution of 45.788 μm per pixel (0.366 mm vector spacing) in the smaller ROI 2; see Fig. 2.11.

For a rotor flow such as the one investigated in the present study, the rotor-

generated blade tip vortices are the dominant flow features and they are also the largest eddies in this flow, containing much more kinetic energy than any smaller vortical structures. Therefore, the diameter of the tip vortex core, d_c, is the characteristic length scale of the energy-containing eddies (or turbulence length scale), l_e. The ratio of the acquisition length scale to the characteristic length scale of the energy-containing eddies, L_m/l_e, was evaluated to be $L_m/l_e = 0.06$ for the measurements made in ROI 2, and $L_m/l_e = 0.13$ for the coarser ROI 1. Ratios of this order were previously found to be sufficient to resolve similar dual-phase flows [71, 107].

Using the 4 Megapixel CMOS camera, the rms error in the particle displacements was estimated to be 0.04 pixels, with a corresponding uncertainty of 0.057 m s^{-1} in the velocity measurements in ROI 1, and 0.06 pixels (0.055 m s^{-1}) in ROI 2, respectively. These values are of the same order as the measurement accuracy reported in Ref. 106.

2.4.5 Dual-Phase PIV Image Processing

After the raw images containing both phases of the flow had been acquired, they were first pre-processed to minimize the effects of reflections from the ground plane or the sediment bed by masking out the static parts that were outside of the flow domain. Because the boundaries can contribute to the correlations obtained, the grey levels of the pixels that contained substantial wall flare were zeroed out. A sliding minimum intensity over each three contiguous raw images for the individual pixels

was determined, and then subtracted from these images to remove the background noise. Because the sensor noise floor was found to be at approximately 20 intensity counts, a minimum intensity threshold of 25 counts was used to filter out the sensor noise and so to further increase the signal-to-noise ratio. A two-dimensional 3 x 3 median filter was then applied to the images to obtain the carrier-phase-only images [108].

Because the sizes of the sediment particles (45–63 μm diameter) and the tracer particles (0.2 μm diameter) were different by two orders of magnitude, the sediment particles (the dispersed phase) also had much higher intensity counts and could be distinguished from the carrier-phase tracer particles by a thresholding method based on size and brightness; see Fig. 2.12. The dispersed phase was identified by first constructing an object identification mask. A binary template was produced by following the method developed by Khalitov and Longmire [109], which employs two-dimensional intensity gradients in addition to saturation threshold criteria to identify the location of the particle images.

The object detection algorithm is relatively sensitive to high-frequency noise because it uses second-order spatial derivatives, which can amplify noise and potentially identify erroneous particles. To avoid such issues, a low-pass spatial filter was applied to each image prior to the computation of the derivatives. The mask was constructed by applying a Gaussian smoothing function with a radius of 1.25 pixels to the median-filtered image to smooth the edges of the large and bright dispersed-phase particle images [110]. After the potential objects in the original image were identified, the size and brightness of each identified object (i.e., a pixel

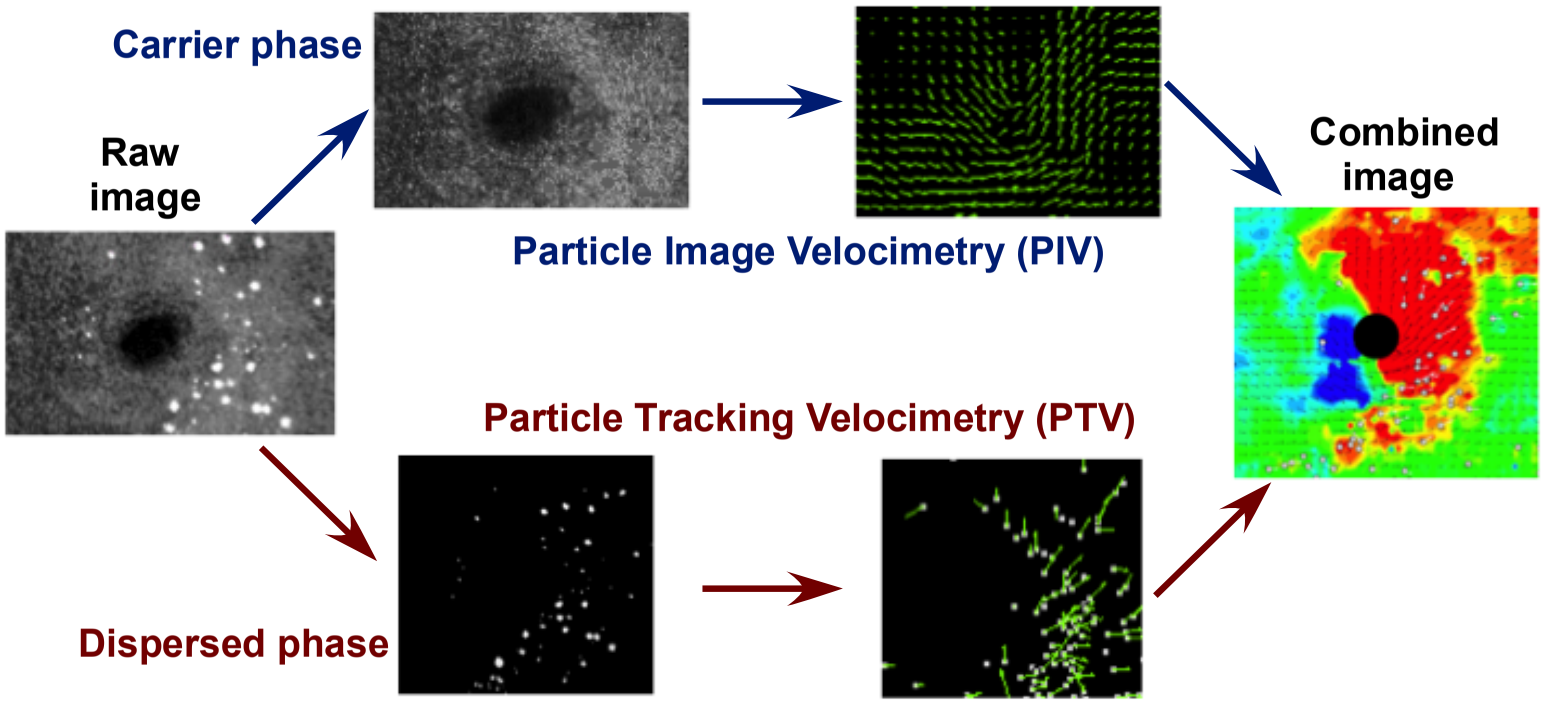

Figure 2.12: Flow chart showing the principal steps of the dual-phase image analysis.

cluster) was used as discrimination criteria to identify the actual sediment particles. A dispersed-phase-only image was then generated, and the intensity values from the original image were copied onto the identified locations; see Fig. 2.12.

Sample images with carrier-phase-only and dispersed-phase-only information were used to identify reliable separation criteria for the respective imaging conditions so as to maximize the number of correctly identified dispersed-phase particles. The same phase separation procedure was also tested on synthetic images. Using a size criteria with a minimum area of 20 pixels (per sediment particle) in ROI 1 and 40 pixels in ROI 2 (greater optical magnification), and an average brightness criteria of $I > 400$ intensity counts, was found to give the best results, identifying about 90% of the particles in a single flow realization. The undetected particles were mostly located on or near to the sediment bed (i.e., they were moving along the sediment bed in wall-parallel direction but not yet high enough from the bed surface to be identifiable) or in regions where a higher concentration of particles made it difficult to distinguish individual particles.

After the phase separation, the carrier phase containing the submicron seed particles was analyzed by applying standard PIV techniques using cross-correlation multigrid, multipass algorithms with interrogation window shifting, 50% overlap, and window deformation. Initial interrogation window sizes of 32 x 32 pixels and final window sizes of 16 x 16 pixels were used, with two passes on each of the interrogation window sizes. The interrogation area size was chosen to get an optimum spatial resolution while retaining a sufficiently high percentage of correctly measured vectors ($> 95\%$ in each vector field).

The applied interrogation window shifting prevented the in-plane loss of correlation and hence bias towards smaller pixel displacements. Relatively small interrogation windows and window deformation techniques minimized gradient bias errors. Also, relatively small values of Δt, the time elapsed between the two consecutive images of a correlated PIV image pair, were used to yield small pixel displacements of no more than one-quarter of the interrogation window size, thus minimizing the out-of-plane loss of correlation. Parallax errors were minimized by using a large object distance (i.e., the distance between the camera lens and the plane of the laser light sheet in which the ROIs are located). Furthermore, by examining the tracer particle displacements, there were no signs of peak-locking effects, i.e., no bias towards integer pixel displacements. Measures taken to prevent peak-locking included using high image densities, i.e., multiple tracer particles inside the correlation window that contributed to the correlation peak.

A local median filter was employed on each pass to remove erroneous velocity vectors and to iteratively replace these vectors by the median of the surrounding 3 x 3 vector grid. The resulting vector fields were post-processed using two passes of the universal outlier detection algorithm of Westerweel and Scarano [111], which was applied in a 3 x 3 filter region to further reduce the number of possible erroneous vectors. Finally, the carrier-phase velocity vector fields from the PIV measurements and the dispersed particle images were recombined to produce a holistic measurement of the dual-phase flow environment; see Fig. 2.12.

In the dual-phase measurements, the carrier-phase images contained some masked holes, which are an inevitable consequence of the subtraction of the dispersed

phase. Furthermore, the flow under investigation was vortically dominated, so using vector validation based on the global mean flow is not that useful because it does not take the local coherent motion of the flow into account. For these reasons, a local median test was performed in each of the passes by the PIV algorithm, not only to assess the validity of the fluid velocity vectors but also to resupply some masked holes with the median vector based on a local 3 x 3 grid, if found to be necessary. However, in the present experiments the particle flow was dilute, the particle sizes relatively small, and the PIV interrogation window sizes large enough to contain enough carrier-phase tracer particles. For these reasons, the respective fluid velocity vectors were mostly obtained based on the first correlation peak. Even in regions with higher sediment particle concentrations, the loss of information in the carrier-phase cross-correlations was negligible and no interpolation was needed.

It was only if no valid first, second, or third displacement peaks could be found (validated by the local median test), that a median interpolation based on the eight neighboring vectors was used at the particle position. Also note that in some cases, lower seeding densities from small but finite centrifugal forces in the core region of the younger vortices could lead to some loss of correlation. However, low seeding densities that required vector interpolation were only detected in a region relatively far upstream and closer to the rotor, which was not a primary focus of the present investigation. These challenges in performing rotor tip vortex measurements with PIV has drawn significant attention and is adequately discussed in the literature [23].

2.5 Two-Dimensional Wall Jet

The mean flow over the ground plane produced by a rotor is reportedly a wall jet-like flow [39]. A nozzle-generated wall jet experiment was conducted to resemble the mean flow over the ground plane produced by the rotor, although this flow did not contain the concentrated vorticity conveyed by the tip vortices and the vortex sheets. Therefore, the wall jet experiment was used with the purpose to separate the unsteady effects of concentrated vorticity (mainly from the tip vortices) from other characteristics of the developing wall flow produced by the rotor. By means of a comparison of the nozzle-generated wall jet and the rotor-generated flow over the ground plane, the goal was to further the understanding of the similarities and differences between these two flows, and so to investigate the effects of the rotor flow structures on the mean flow.

Besides the complexity of the rotor flow itself, simplified assumptions and approximations must be used to model particle mobilization and transport from an underlying sediment bed. Such so-called threshold or "pickup" models [49, 50] are, in general, semi-empirical integral descriptions based on the assumptions of steady, uniform, turbulent boundary layer flows [80, 81]. However, the validity of such models is certainly more questionable for the nonequilibrium flows found below a rotor. If the underlying carrier flow is modeled inaccurately, then the predicted particle motion will also be affected. Therefore, detailed comparisons of the rotor flow measurements to those of more canonical wall jet flows were performed.

2.5.1 Setup and Test Conditions

A dual-exit nozzle was placed adjacent to a ground plane to produce a nominally two-dimensional wall jet along the surface; see Fig. 2.13. The nozzle design (see Fig. 2.14) had the capability of producing both a lower and upper jet, although for the present work the upper nozzle was closed. The jet of the lower nozzle with an aspect ratio of 44:1 had an exit height of $h = 14$ mm (0.551 in) and a measured exit velocity of $u_{\text{jet}} = 3.3$ m s^{-1} (10.8 ft s^{-1}) corresponding to a jet Reynolds number of

$$Re_{\text{jet}} = \frac{u_{\text{jet}} h}{\nu} = 3,000 \tag{2.15}$$

The bottom edge of the nozzle was placed flush with a ground plane; see Fig. 2.13. These operating conditions of the nozzle were chosen so as to produce

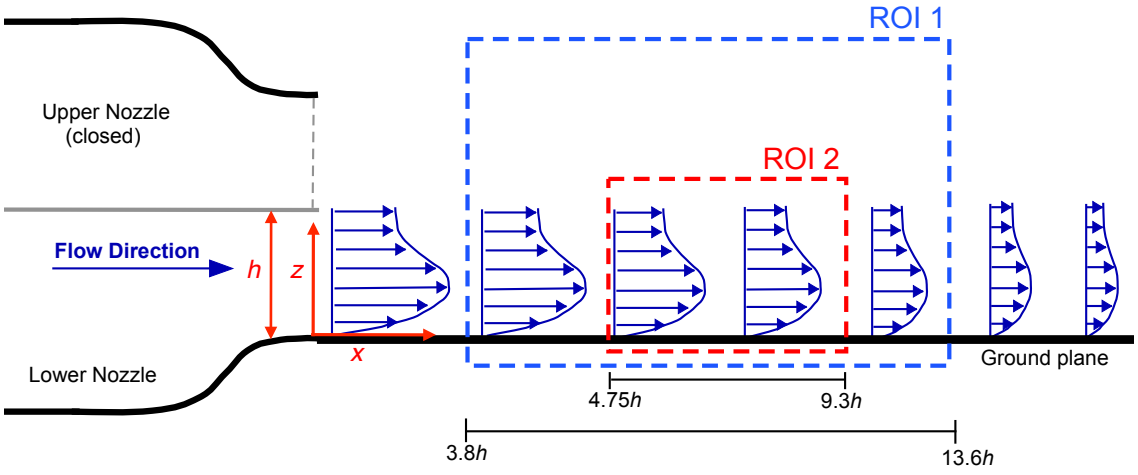

Figure 2.13: Schematic showing nozzle, ground plane, and ROIs for the wall jet experiment.

a wall jet over the ground plane that had similar velocities as the rotor-generated wall jet-like flow (see Section 2.3), and so enabling a valid comparison between these flows.

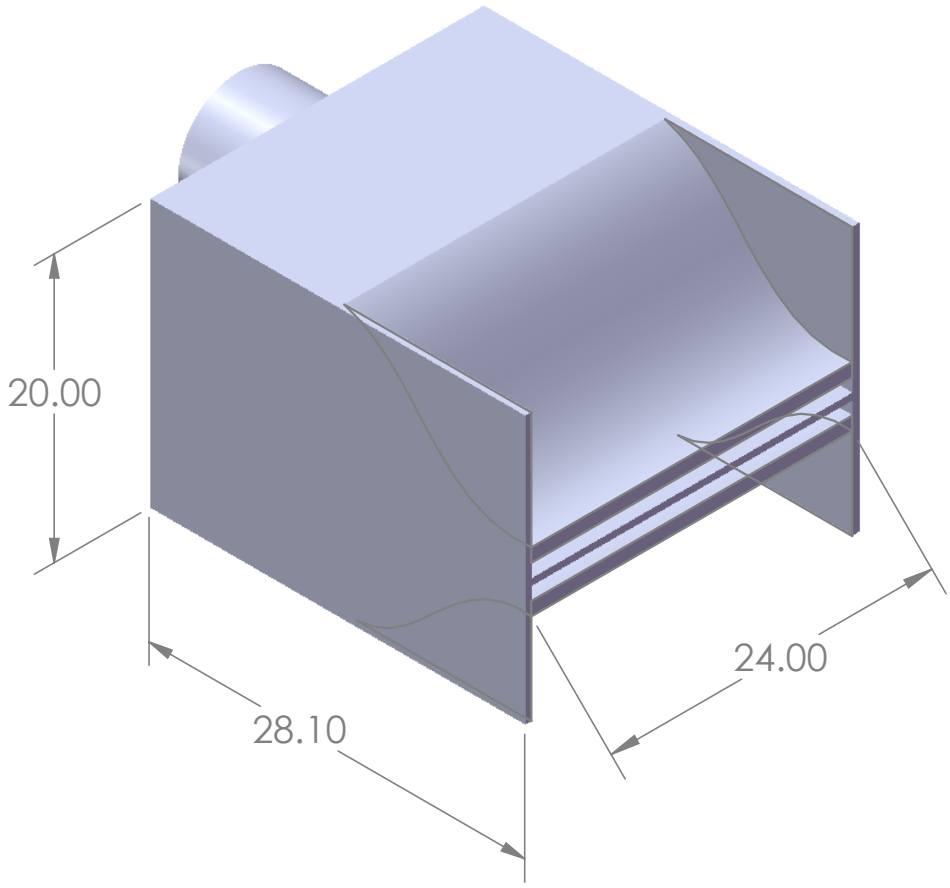

Figure 2.14: Drawing showing the nozzle producing a two-dimensional wall jet. (All dimensions are in inches.)

2.5.2 Measurement Equipment, Image Acquisition and Processing

PIV measurements were performed along the downstream flow direction at the centerline of the jet using the Nd:YLF laser and the 1 Megapixel CMOS camera, as previously described in Section 2.4.4. The flow was seeded with submicron mineral oil particles with a mean diameter of 0.2 μm; see Section 2.2.5. To obtain a contiguous time-history of the flow, PIV image pairs were obtained at a frame rate of 1,000 fps in this case. A schematic of the setup with the hardware components used is shown in Fig. 2.15.

The thin, diverging laser light sheet was oriented vertically, bisecting the midline of the nozzle; see Fig. 2.15. Tangential illumination of the ground plane was used to minimize laser reflections. This ground plane also was painted a flat black to further minimize surface reflections of the laser light. The camera axis was aligned to be orthogonal to the light sheet so that its focused field of view was in the plane of the laser light sheet; see Fig. 2.13.

The ROIs that used to study this wall jet flow are shown in Fig. 2.13. ROI 1 was used to gain a global understanding of the flow as it developed over the ground plane. For this purpose, a 105 mm lens (set to an $f^{\#}$ of 2.8) was used to obtain the PIV images in this relatively large ROI. A 200 mm lens (set to an $f^{\#}$ of 4) was focused on the smaller ROI 2, allowing for a greater magnification of the flow field and so yielding a finer spatial resolution in this ROI. Therefore, the measurements in ROI 2 were used to resolve the details of the boundary-layer flow.

The laser pulse separation time was set to 70 μs for ROI 1 and 50 μs for ROI 2.

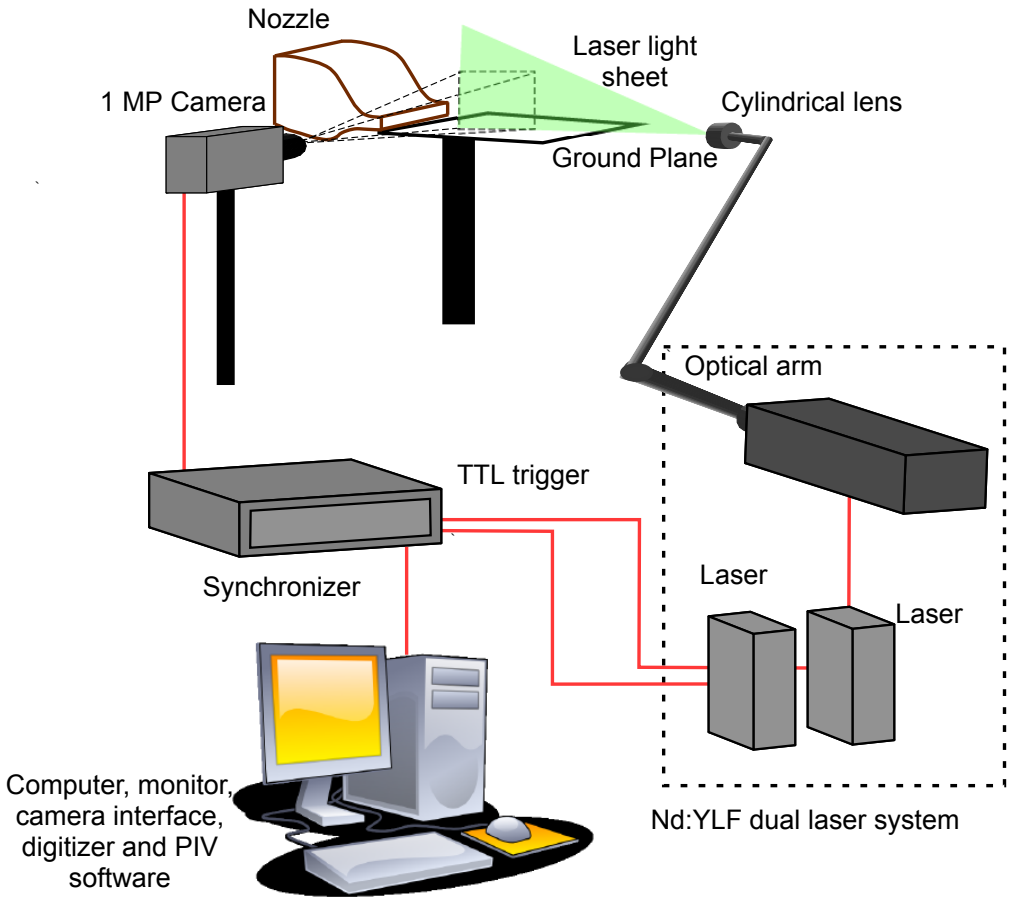

Figure 2.15: Schematic showing the experimental setup for the wall jet experiments.

The spatial resolution for these measurements was 147.06 μm per pixel (1.176 mm vector spacing) in ROI 1, and a finer resolution of 67.57 μm per pixel (0.54 mm vector spacing) was obtained in ROI 2. The estimated measurement accuracy for the displacement in ROI 1 and 2 was 0.03 pixels and 0.04 pixels, respectively. 1,000 contiguous PIV image pairs were obtained and used for the calculation of the mean

flow quantities, and the PIV image processing procedure was the same as used for the investigation of the rotor flow, as previously described in Section 2.3.5.

2.6 Summary

In the present chapter, detailed descriptions were given of the three experiments that have been performed, along with the methodology used to obtain the measurements. The experimental setups were shown and explained, and the specific test conditions and operating parameters for each of the experiments were reported. The PIV and PTV measurement techniques were also introduced, as these techniques were used to measure the single-phase and the dual-phase flow fields. Image acquisition and data processing procedures were also described. The results from the analyses of the single-phase and the dual-phase flow field measurements are discussed in the following chapter.

Chapter 3: Results and Discussion

The dual-phase flow measurements were analyzed to examine how the mean flow properties, turbulence fields, and coherent vortex structures (e.g., the rotor blade tip vortices) affected the onset of particle motion and the subsequent transport of particles along and away from the sediment bed. Furthermore, the near-wall flows including the boundary layers were examined to gain new insight into the flow and turbulence structure of rotor-generated near-wall flows, including the Reynolds stress distributions. The single-phase flow results obtained using the larger (0.816 m-diameter) rotor were also compared to the measurements made for the nozzle-generated wall jet flow to better understand the similarities and differences between these two flows. Coherent vortices and smaller-scale turbulence structures could be detected, and in conjunction with the measured sediment fluxes could be correlated to the movement and pickup of particles from the sediment bed. The quadrant analysis method developed by Wallace et al. [59] was also employed to help better understand the nature of the turbulent, dual-phase flow environment near the bed.

The results from separate single-phase (i.e., without particles) and dual-phase (i.e., with particles) experiments were also analyzed comparatively to understand

how the addition of the particle (dispersed) phase affected the fluid (carrier) flow, i.e., to investigate the extent and nature of potential two-way coupling of the flow phases. The relatively high spatio-temporal resolution of the present measurements made it possible to resolve accurately the flows induced by the helicoidal tip vortices that were trailed from the blades as well as their associated smaller-scale turbulent structures, and to track the individual flow structures as they convected through the flow toward the ground plane. The contiguous time-history of the measurements enabled detailed assessments as to how the coherent vortex structures were influenced by the presence of sediment particles, and also how these particles may have modified the mean flow and turbulence characteristics of the carrier flow.

3.1 Single-Phase Near-Wall Flow Measurements

Understanding the detailed fluid dynamic characteristics of the complex rotor flow at the ground, even at the absence of sediment particles, is a prerequisite to establish and validate mathematical models for bedload transport and particle uplift models that may be applicable to such rotor flows. For these purposes, measurements of the instantaneous characteristics of the flow and the velocity excursions at the ground are key [2, 44, 45]. Nevertheless, the mean fluid motion also gives much insight into the flow and exposes certain flow characteristics that could be useful as inputs to numerical flow simulations, such as the prescription of characteristic boundary-layer profiles at the ground and/or sediment bed [53].

The coherent vortical structures at the ground below the rotor have their initial source in the tip vortices and vortex sheets trailed from the rotor blades. However, after ensemble-averaging to find the mean flow quantities, many distinct aspects of the rotor flow become otherwise ameliorated. The spatial resolution of the boundary-layers over the ground plane and sediment bed that were obtained in the present measurements allowed for the viscous sublayer to be resolved; in this near-wall layer the velocity gradient is constant. With this measured velocity gradient at the wall, the wall shear stress, τ_w, and the friction velocity, u_τ, were then estimated. These values were used to normalize the velocity u and the wall-normal distance z to obtain results in so-called wall coordinates, u^+ and z^+, i.e., the inner scaling, which is a useful form for comparisons with other types of boundary-layer measurements.

3.1.1 Mean Flow Velocity Distributions

Representative profiles of the time-averaged and phased-averaged (periodic) wall-parallel velocity for three downstream distances from the rotor centerline are shown in Fig. 3.1. The phase-averaged results were ensemble-averaged over consecutive PIV flow field realizations with the rotor blade in the same azimuthal position, i.e., the blade position was phase-locked. The mean velocity profiles obtained for the rotor near-wall flow, which are shown in Fig. 3.1, appeared to be qualitatively very similar to those of a developing turbulent wall jet [112]. Canonical flows, such

as channel or pipe flows, contain organized turbulence structures in the near-wall region [60]. However, the initial source of turbulence in such flows is not the more concentrated vorticity as is produced in this case with the rotor flow. Therefore, at least some differences in the near-wall turbulence structures are to be expected for these foregoing reasons alone.

A comparison of the mean velocity fields generated by the rotor versus the wall jet is shown in Fig. 3.2. When time-averaging of the rotor flow was performed, the resulting mean characteristics of the flow indeed showed many of the features seen with the wall jet. In Fig. 3.2, the background contours are the mean wall-parallel velocity components, $\overline{u}$. Note that the length scales for the rotor were normalized by the rotor radius, R, while for the nozzle they were normalized by the nozzle exit height, h, which is by convention. The corresponding velocities were normalized by rotor tip speed, V_{tip}, and nozzle exit velocity, u_{jet}, respectively. The time-averaged velocity distribution far downstream from the rotor (i.e., the region shown) and the velocity distribution produced by the nozzle are seen to be similar. Both flows also show a well-defined slipstream boundary directly above the wall jet. Viscous shearing and diffusion in the flow also occurs further downstream in both cases.

To examine further the mean flow produced by the wall jet, the average wall-parallel velocity profiles were extracted at several downstream distances from the nozzle exit; see Fig. 3.3. Notice that the flow decelerates with increasing distance along the wall because of a thickening of the boundary layer. Comparing the time-averaged wall-parallel velocity profile generated by the rotor to that of the wall jet for a corresponding location far downstream shows how similar the mean flows at

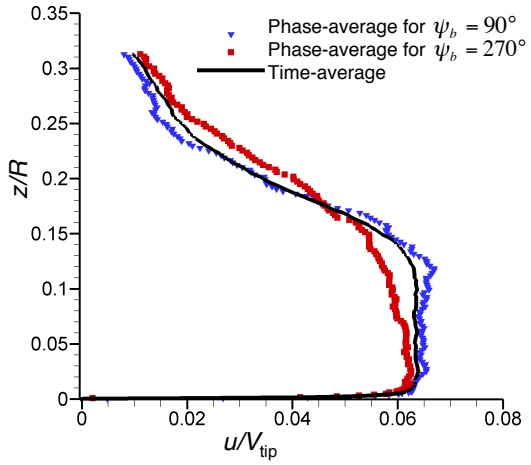

(a)

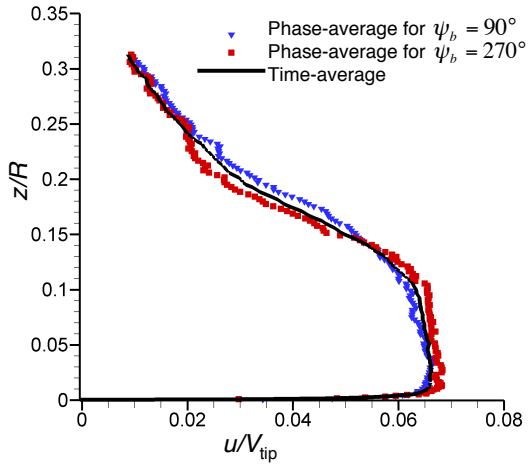

(b)

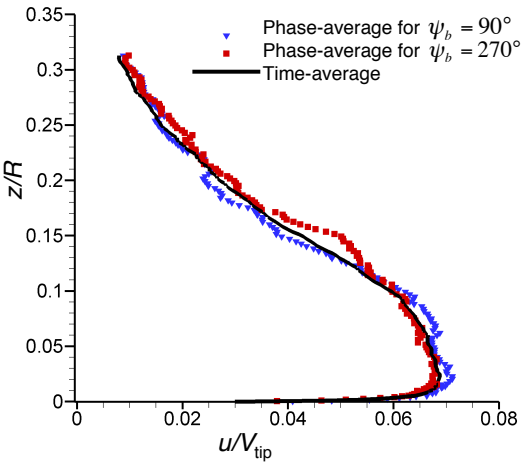

(c)

Figure 3.1: Time-averaged and phase-averaged wall-parallel velocity at the ground plane below the 0.816 m-diameter rotor operating at 1,860 rpm and $C_T/\sigma = 0.08$ for: (a) $r/R = 1.29$, (b) $r/R = 1.40$, (c) $r/R = 1.60$.

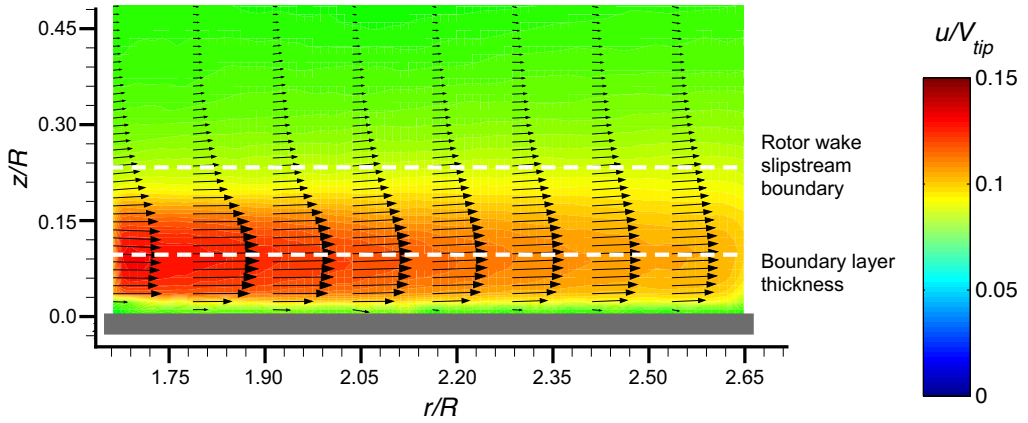

(a) Rotor-induced flow at the ground below the smaller (0.17 m-diameter) rotor system operating at 3,600 rpm and $C_T/\sigma = 0.156$.

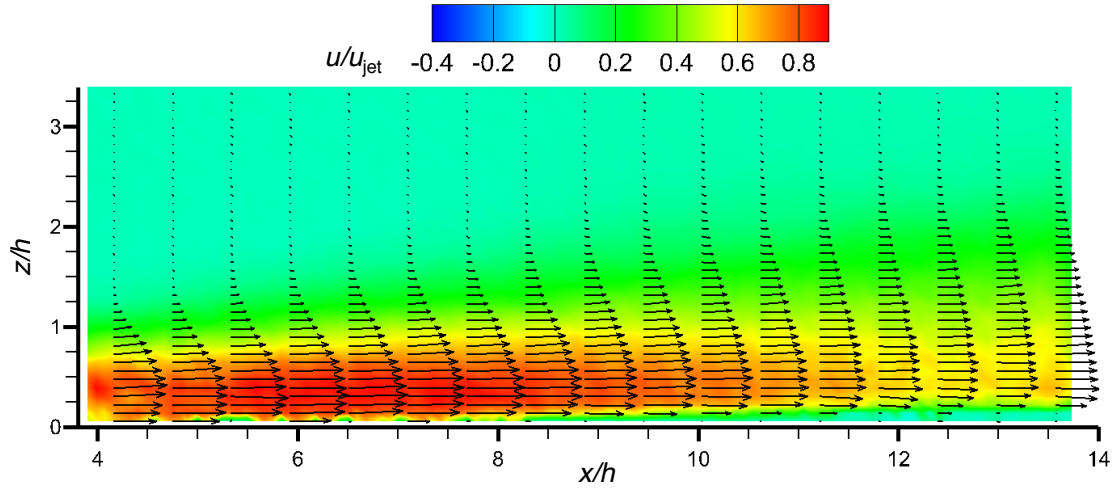

(b) Wall-jet flow produced by the nozzle for a jet exit velocity of $u_{\text{jet}} = 3.3\ \text{m}\,\text{s}^{-1}$.

Figure 3.2: Comparison of the time-averaged single-phase flow as produced by: (a) the rotor, (b) the two-dimensional wall jet.

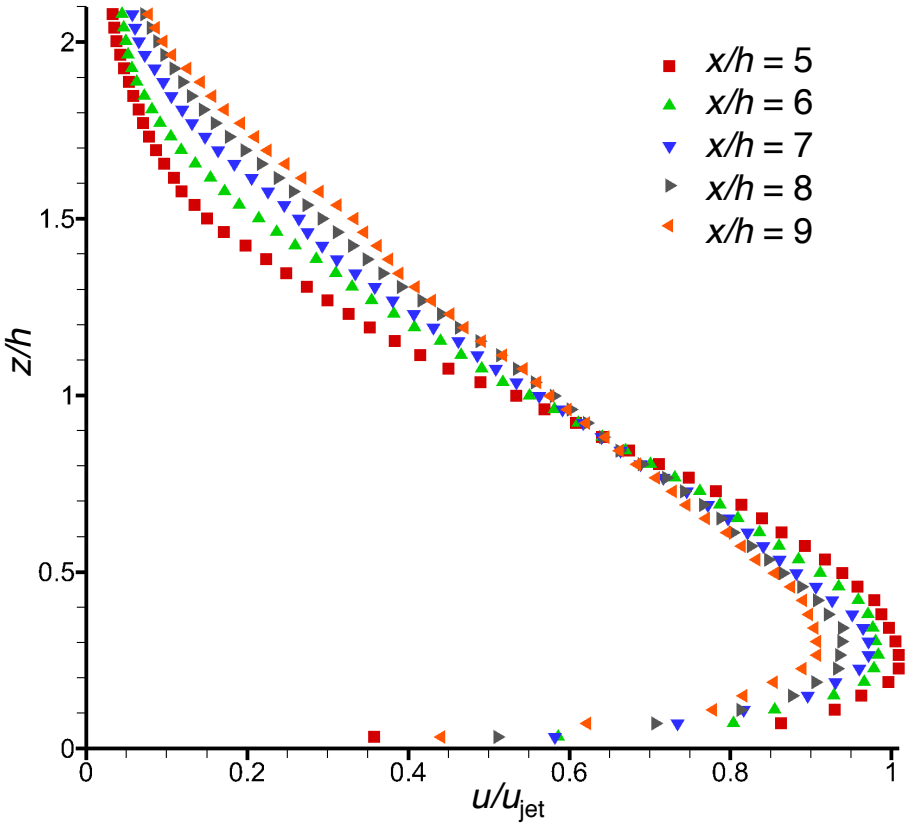

Figure 3.3: Measured velocity profiles at five downstream locations from the exit of the nozzle used to generate the wall jet.

the ground actually are; see Figs. 3.1 (c) and 3.3. An inflection point in the velocity profiles occurs as the flow transitions more into a fully developed turbulent wall jet. A pronounced velocity peak close to the surface is also apparent in both flows. However, for the rotor-induced flow there are clearly differences in the regions further upstream.

This latter behavior becomes apparent when the boundary-layer profiles are plotted in the inner scaling, u^+ for the normalized streamwise velocity and z^+ for the normalized distance from the wall; see Fig. 3.4 for the rotor and Fig. 3.5 for the

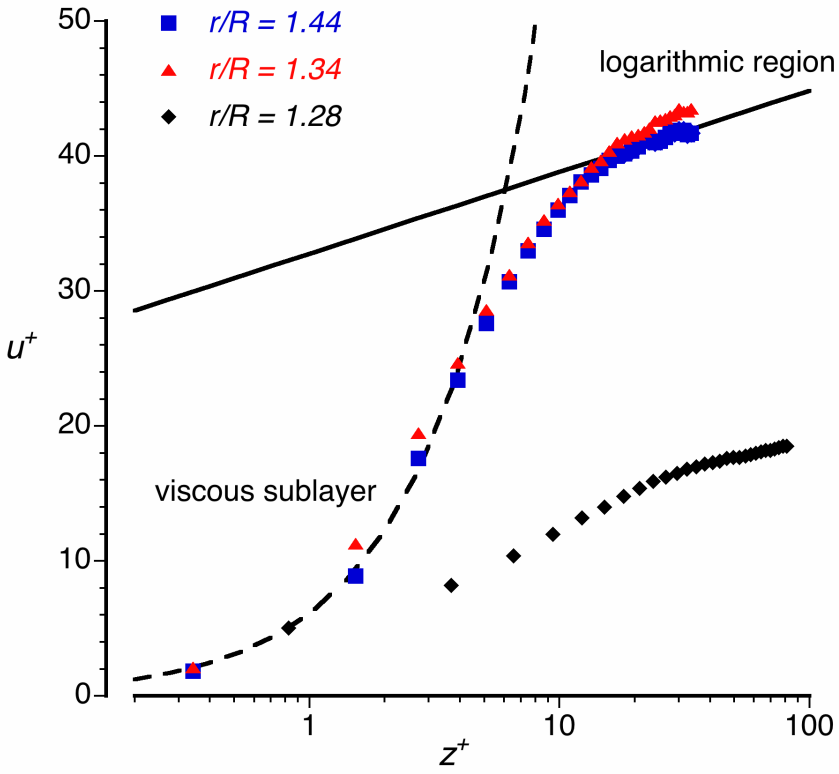

Figure 3.4: Semi-logarithmic boundary-layer profiles at the ground produced by the rotor flow in terms of wall units. The viscous sublayer region and the logarithmic region were approximated using curve-fits to the measured data.

wall jet measurements. While the two locations further downstream from the rotor showed a velocity profile typical of a fully developed turbulent boundary layer or the inner layer of a turbulent wall jet, which are qualitatively the same [113], the profiles measured further upstream did not show this behavior (e.g., for $r/R = 1.28$ in this case). The Reynolds number of the boundary layer over the ground plane as generated by the rotor flow was $Re = 3,000$ using Eq. 2.15.

The approximately constant velocity gradient measured close to the wall suggested that the corresponding measurement points were in the viscous sublayer.

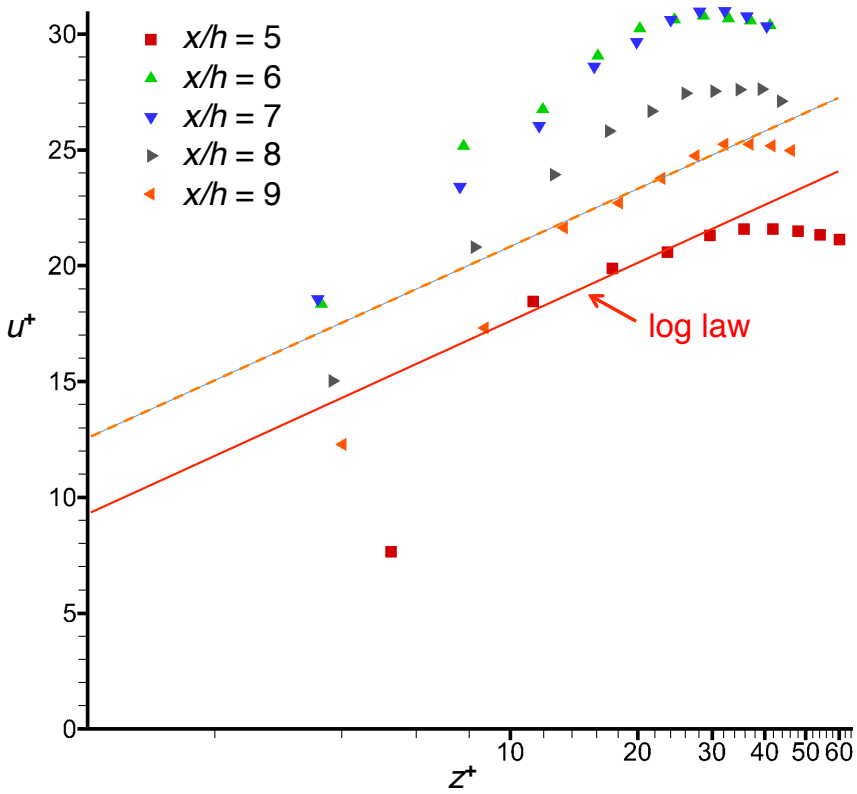

Figure 3.5: Semi-logarithmic boundary-layer profiles for five downstream distances from the nozzle exit. The logarithmic region was approximated by a curve-fit to the measured data.

This result can also be seen in Fig. 3.4, which suggests that the four measurement points closest to the wall were within the viscous sublayer. The values of u^+ were not equal to z^+ in this region, which may be because the velocity gradient was measured too far away from the wall where it is not strictly constant. Obviously, the calculated value of the friction velocity, u_τ, is extremely sensitive to the measured velocity gradient at the wall. As z^+ approached about 20 wall units, the flow transitioned to a more logarithmic velocity profile.

These findings are important because they have implications on the modeling

of the rotor flow at the ground as well as for verifying the validity of particle mobility and uplift models, e.g. [49, 50], where a velocity profile at the wall may be prescribed. The measurements further downstream have revealed the approximate wall-normal expansion of the viscous sublayer, and they confirm that the use of a logarithmic velocity profile [53] is a good assumption between the viscous portion of the flow and the fully turbulent outer flow. The same conclusion, however, cannot be as easily drawn for the near-wall locations that are further upstream and closer to the rotor. This latter finding is attributed to the relatively complex flow regime closer to the rotor, where the vertical velocity components were significant and the flow was still in the process of turning from a mostly axial direction to a flow that was expanding radially outward over the ground plane; see Fig. 1.5. The turbulent boundary layer on the ground was also not yet fully developed so close to the rotor.

For the wall jet experiment, measurements could not be obtained as deeply into the boundary-layer regions because of the lower spatial resolution of the 1 Megapixel CMOS camera used in this case, and the need to capture a relatively large field of view. The linear region in the semi-logarithmic graph (Fig. 3.5) indicated the logarithmic region of the boundary layer, with the measurement point closest to the ground being at least in the buffer layer or just touching the edge of the viscous sublayer. The Reynolds number based on the measured nozzle exit velocity and the nozzle height was $Re_{\text{jet}} = u_{\text{jet}}h/\nu = 3,000$. For flows with such low Reynolds numbers, the log law does not extend very far from the wall [114, 115], as confirmed by the measurements shown in Fig. 3.5. Depending on the distance downstream from the nozzle exit, the log law region in this case only extended to $z^+ \approx 35$.

3.1.2 Turbulent Flow Environment Near the Ground Plane: Viscous and Turbulent Shear Stresses

The vortically-dominated flow below a rotor contains distinct unsteady flow features such as the discrete blade tip vortices and the turbulent vortex sheets; see Fig. 1.5. Shown in Fig. 3.6 is an instantaneous flow realization of the region at the ground below the rotor, which illustrates the influence of the discrete blade tip vortices on the boundary-layer region. These results show the locally higher induced flow velocities at the ground that are induced by the passing vortices. There is also a local thickening of the boundary layer, which is a consequence of the adverse pressure gradient produced by this vortex flow. In fact, the results in this case suggested that the boundary layer immediately below the vortex was in a state of incipient separation. In fact, it can be expected that the boundary layer on the ground plane may thicken or even separate in proximity to vortices of sufficient strength. In this regard, such outcomes can also affect the process of sediment uplift and entrainment, as shown for channel and riverine flows by Nelson et al. [62] and for a rotor flow by Johnson et al. [41].

Notice the good detail in the measurements shown in Fig. 3.6. Measurements in this case were made to as close as $0.001R$ above the ground plane. Below that height, issues associated with surface reflections of the incident laser light sheet became problematic and the PIV measurements became more challenging. To avoid

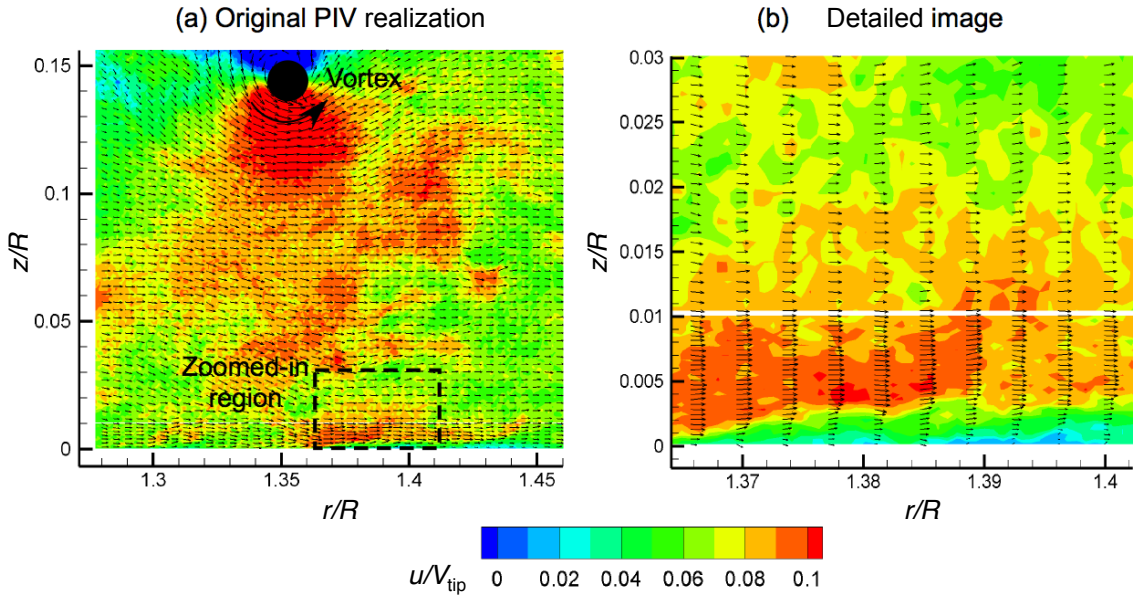

Figure 3.6: Examples of the instantaneous flow near the wall produced by the 0.816 m-diameter rotor. Instantaneous flow vectors are plotted on background contours of wall-parallel velocity. Area of detailed image shown by the dashed line.

image congestion in Fig. 3.6(b) only every fifth vector is shown in the horizontal direction, although every vector is shown in the wall-normal direction up to $z/R = 0.01$.

The time-averaged velocity fluctuations, $\overline{u'}$ and $\overline{v'}$, are by definition zero. The time-averages of the squares and mixed products, however, are non-zero, and are the source of the Reynolds stresses. Although Reynolds-averaging techniques do not explicitly account for coherent motions in the turbulence, some instantaneous organization is apparent even in the averaged terms. Otherwise, $-\rho\,\overline{u'v'}$ (the most important closure term for the incompressible RANS equations) would be zero if the turbulent motions were purely random without preferred correlations between the

velocity components. The Reynolds stresses are also a measure for the turbulence intensity and the effect turbulent structures have on the mean flow. The motion of sediment particles arises, at least in part, from the shear stresses produced on the sediment bed by the external flow [49]. When a threshold condition is reached, sediment is initially transported downstream and can then be entrained and uplifted into the outer flow by turbulent eddies and/or vortices [65].

The fluctuating parts of the flow velocities were extracted from the present measurements, which were then used for the computation of the normal and shear Reynolds stress components. By performing a classic Reynolds decomposition, the fluctuation (or perturbation) velocities are

$$u'_{i,j} = u_{i,j} - \overline{u_{i,j}} \tag{3.1}$$

$$v'_{i,j} = v_{i,j} - \overline{v_{i,j}} \tag{3.2}$$

In this case, $u'_{i,j}$ is the perturbation velocity at a single interrogation point, $u_{i,j}$ is the instantaneous velocity at this point, and $\overline{u_{i,j}}$ is the average u velocity. The average velocity components were calculated using

$$\overline{u_{i,j}} = \frac{1}{N} \sum_{k=1}^{N} u_{i,j}(k) \tag{3.3}$$

where N is the number of contiguous PIV realizations. A similar equation holds for the v component.

The Reynolds stress tensor in some instances is divided by the fluid density,

ρ, giving $\overline{u'v'}$ for the shear component and $\overline{u'^2}$ and $\overline{v'^2}$ for the streamwise and wall-normal turbulent stress components, respectively. The corresponding instantaneous values of the Reynolds stresses are $u'v'$, u'^2, and v'^2, respectively.

The measured Reynolds shear stress components for the rotor shown in Fig. 3.7 revealed significant differences to both a turbulent wall jet [112] and also to a fully developed turbulent boundary layer [113]. In this case, all of the data were normalized by the same local length and velocity scales. At the same normalized distance from the wall, the wall-nearest measurement points (below $0.4\,z_{\max}$) at the two locations further downstream from the rotor were in the viscous sublayer (indicated by the decreasing Reynolds stresses; also see Fig. 3.4), while they were well above the viscous sublayer in the turbulent wall jet measurements [112]. Similarly, the point where the Reynolds shear stresses changed sign was located further away from the wall for the measurements below the rotor compared to the wall jet. These comparative results suggest that different length scales and turbulence intensities are indeed involved with the rotor flow.

It is also shown in Figs. 3.7–3.9 that there were significant fluctuations in the Reynolds stresses near the ground that are not present in the simpler wall jet flows. These different effects result from the more complex flow environment at the ground induced by the rotor, which contains not only regions of concentrated vorticity (such as from the tip vortices) but also the vortex sheets trailed from the inner parts of the rotor blades.

Besides the differences in the general nature of rotor flows and wall jet or turbulent boundary-layer flows over a surface, the present experiments were not

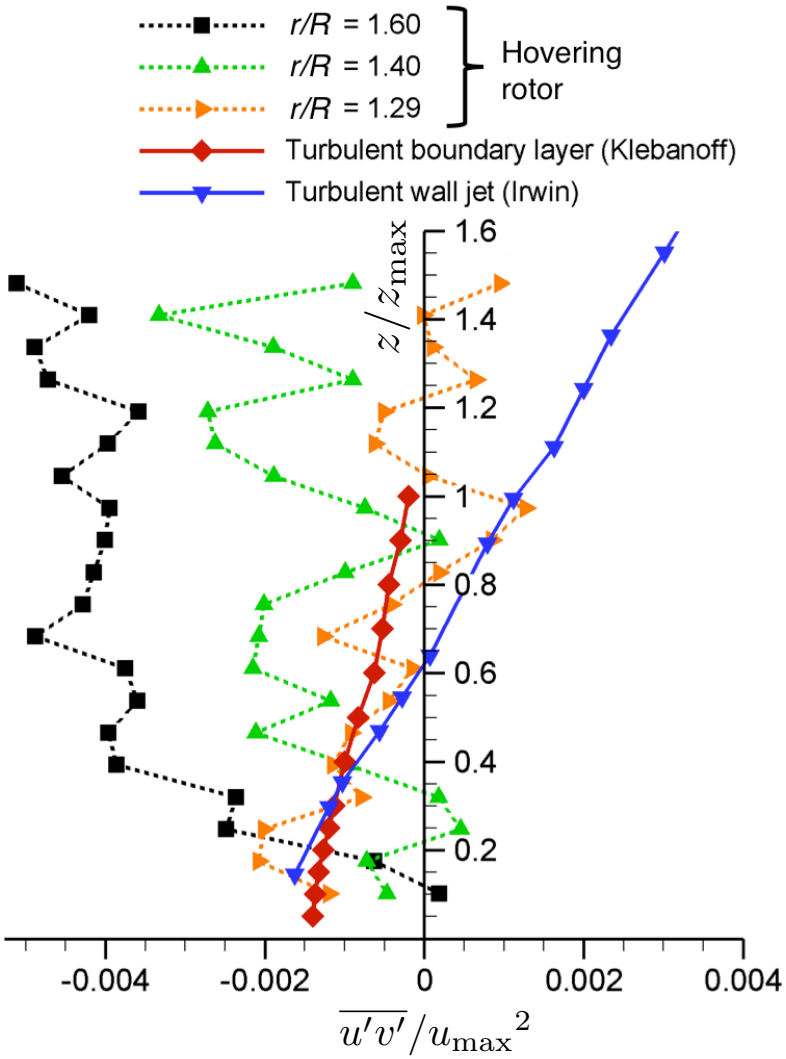

Figure 3.7: Comparison of the boundary-layer flow in terms of Reynolds shear stress, $\overline{u'v'}$, measured at the ground below the 0.816 m-diameter rotor to two more canonical flows.

conducted at the same Reynolds numbers. The boundary-layer Reynolds number over the ground plane for the rotor flow measurements was $Re = u_{\max} z_{\max}/\nu = 3,000$, while it was 74,000 for Klebanoff's experiment [113] and 24,000 for Irwin's wall jet experiment [112]. It is acknowledged that Reynolds number effects may change the structure of the turbulence, length, and time scales to some extent [114–116], which will affect the Reynolds stress distributions. Therefore, the different length scales obtained, which are apparent from Fig. 3.7, could still be influenced by the different Reynolds numbers of the experiments, and this issue is worthy of future study.

The total shear stresses were decomposed into their viscous and turbulent parts to examine how the contribution of turbulence structures to the total shear changes with wall-normal distance, and to determine whether they may be neglected very close to the surface, i.e., deep in the boundary layer. The shear stress decomposition uses

$$\tau = \tau_v + \tau_t = \mu \left(\frac{\partial u}{\partial z} \right) - \rho \, \overline{u'v'} \tag{3.4}$$

where $\tau_v = \mu(\partial u/\partial z)$ is the viscous shear stress and $\tau_t = -\rho \, \overline{u'v'}$ is the turbulent shear stress (or Reynolds shear stress), both in two dimensions in this case.

Because the flow at the ground is highly turbulent, the Reynolds stresses τ_t are the dominant source of shear stresses in the boundary-layer region and also in the outer flow, which can be concluded from the results shown in Fig. 3.8. Notice that the maximum of Reynolds shear stress coincides with the slipstream boundary between the accelerated flow inside the rotor wake and the more quiescent outer flow. In the case of the rotor flow, the tip vortices also travel downstream along the slipstream

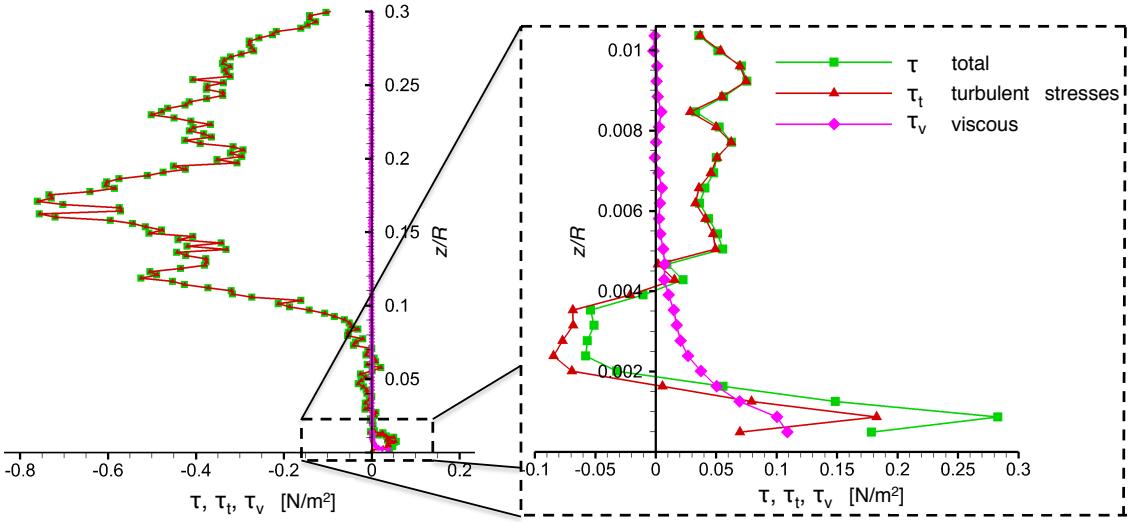

Figure 3.8: Contribution of the viscous and turbulent shear stresses to the total shear stress in the outer flow (left) and the boundary layer (right) for single-phase flow measurements at $r/R = 1.44$ from the axis of the 0.816 m-diameter rotor.

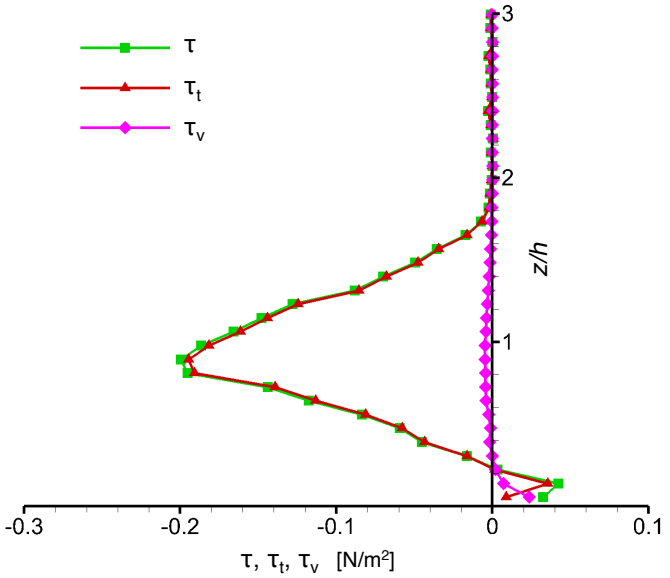

Figure 3.9: Contribution of viscous and turbulent shear to the total shear stress in the outer flow for the wall jet at $x/h = 6$.

boundary, generating additional turbulent stresses in the process; see Fig. 1.5. The turbulent shear stresses, $-\rho\,\overline{u'v'}$, become positive near the wall, this observation having also been made with wall jet flows [117], and can be explained with the aid of Prandtl's mixing length theory [118]. Although the viscous contributions increased for wall-normal distances of $z/R < 0.004$ when moving toward the ground plane, the turbulent stresses there were still significant.

While Fig. 3.8 shows the contribution of the viscous and the turbulent shear to the total shear stress for the rotor at a radial location of $r/R = 1.44$ (i.e., well downstream from the rotor), Fig. 3.9 shows the same decomposition for measurements obtained with the wall jet at a streamwise location of $x/h = 6$ from the nozzle exit. This downstream distance was chosen because the wall jet profile was developed but had not yet begun to expand significantly; see the complete flow field shown in Fig. 3.2(b). For the wall jet experiment, the lower spatial resolution available in the measurements did not permit the stresses in the boundary-layer region to be resolved to the same level of detail.

Overall, the general trends in the ensemble-averaged Reynolds shear stress profiles measured with the wall jet were noted to be similar to those found for the rotor-induced flow. The change in sign of the turbulent shear stresses near the wall was observed, as well as the secondary (positive) peak in the near-wall region; see Fig. 3.9. However, there were also distinct differences between the two flows. For example, the rotor flow showed significant small-scale and large-scale spatial variations in the stresses, both with wall-normal distance (Fig. 3.8) and also with downstream distance (Fig. 3.7). The wall-normal spatial variations in the shear

stress profile were not found in the wall jet flow; see Fig. 3.9. For both flows, the global maxima of the total shear stresses were located in the shear layer between the accelerated flow closer to the wall and the more quiescent flow further away from the wall. The distinctly shaped peak at $z/R = 0.17$, as shown in the rotor flow, is an artifact of the blade tip vortices that convect downstream, which contribute additional turbulent stresses there.

3.2 Dual-Phase Flow Measurements: Particle Mobilization and Sediment Pickup from the Particle Bed

The single-phase measurements give considerable insight into the fluid dynamics at the ground below the rotor. However, to understand the mobilization and uplift of sediment, a detailed analysis of the dual-phase measurements was conducted. Such measurements provide essential results that expose the key relationships between the effects of flow features contained in the carrier phase and the resulting particle motions. Single-phase measurements (without sediment) have also been conducted under the same conditions to examine what conclusions might be drawn about the potential behavior of the dispersed phase from single-phase flow measurements. The single-phase measurements can also help to understand the differences in the flow properties that may arise from the addition of a dispersed phase, i.e., the extent of two-way coupling between the flow phases.

3.2.1 Dual-Phase Flow Environment Below the Rotor

Figure 3.10 shows an instantaneous flow realization of the dual-phase flow environment generated by the smaller (0.17 m-diameter) rotor. Also shown here are the coherent tip vortices. The tip vortex seen further downstream at $r/R = 2.0$ reveals the distinct quadrupole structure that is associated with coherent vortices when shearing stresses (or strain rates) are analyzed in a Cartesian coordinate system [119, 120]. Beside the concentrated vorticity, smaller-scale $u'v'$ correlations that indicate small vortex structures, eddies, and other secondary flow structures, were seen to be contained in the flow at the ground.

The secondary flow structures near the ground plane were induced by the

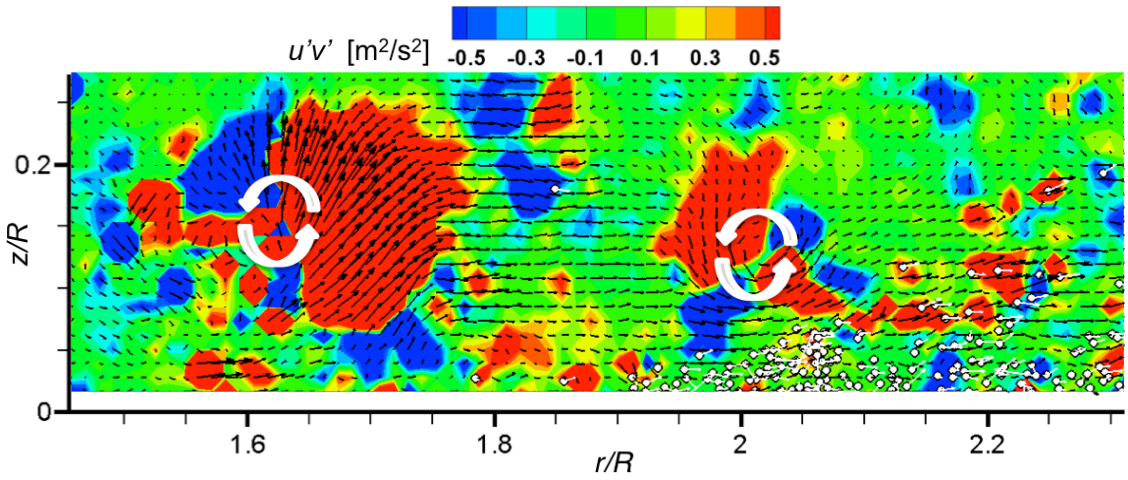

Figure 3.10: Dual-phase flow realization above the sediment bed showing instantaneous velocity vectors of the carrier and dispersed phases on a background contour of instantaneous Reynolds shear stress. White arrows denote location of vortex cores.

interaction of the coherent primary vortex structures with the ground, or by interactions between the vortices themselves. The occurrence of such small-scale vortical structures was observed to be relatively frequent in the dual-phase flow near the sediment bed, but also at greater wall-normal distances. Furthermore, the tip vortices were seen to expose a less pronounced quadrupole structure in the dual-phase flow environment as compared to the single-phase flow. Such observed differences in the flows raise the question as to whether the particles altered the flow properties of the carrier phase. This potential coupling of the flow phases is discussed in detail later in Section 3.3.

The time-histories of the flow fields near the ground plane were obtained from the time-resolved single-phase and dual-phase measurements. While Fig. 3.10 is only one representative example, it shows that despite an intense upwash region (i.e., positive wall-normal velocity) at $r/R = 1.7$ in this instance, sediment is not picked up from the bed there and is instead uplifted further downstream. In fact, the dual-phase measurements revealed that most particles constituting the sediment bed below the rotor were picked up and suspended relatively far downstream from the rotor, i.e., at $r/R = 2.0$ and further; see Fig. 3.10 for one instantaneous flow realization. This finding was not initially expected because the vortex structures are more coherent upstream of this location before they are diffused through the action of viscous shearing and turbulence as they interact with the ground plane further downstream.

3.2.2 Time-Averaged Particle Flux

Because of the interesting qualitative observation of sediment pickup occurring mostly at greater downstream distances from the rotor (see the exemplary instantaneous dual-phase flow field shown in Fig. 3.10), the particle motion was quantified by measuring particle fluxes in the radial and wall-normal directions. The particle fluxes were calculated by dividing the ROI up into grid cells. At each time-step (i.e., each instantaneous flow realization) the location of a given particle at the next time-step is projected by the measured particle velocity from the PTV algorithm. If the particle has crossed the border of a cell in the wall-normal or in the wall-parallel direction (i.e., it has entered an adjacent grid cell), the count is advanced appropriately.

From the instantaneous particle flux measurements, the time-averaged values were obtained by performing an ensemble-average over the total quantity of instantaneous flow realizations. The results in the radial (streamwise) direction are shown in Fig. 3.11, with the corresponding vertical (wall-normal) fluxes being shown in Fig. 3.12. The grid size for the particle flux measurements was dictated by the concentration of particles in the flow; too fine a grid will result in too few particles per grid cell to be statistically meaningful.

From Fig. 3.11, it is apparent that the streamwise particle flux just above the sediment bed has increased sharply downstream of $r/R \approx 1.8$ and reached a maximum between $1.9R$ and $2.0R$. After this point, the flux decreased slightly but was still relatively high. Particles need to be mobilized before they can be detected by the PTV algorithm. Therefore, the root cause for initial mobilization of particles

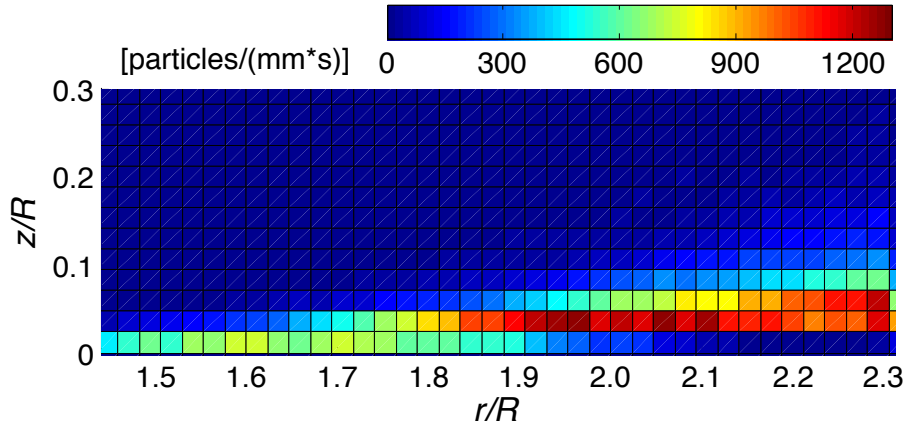

Figure 3.11: Time-averaged wall-parallel particle flux as produced by the 0.17 m-diameter rotor in the ROI shown in Fig. 3.10.

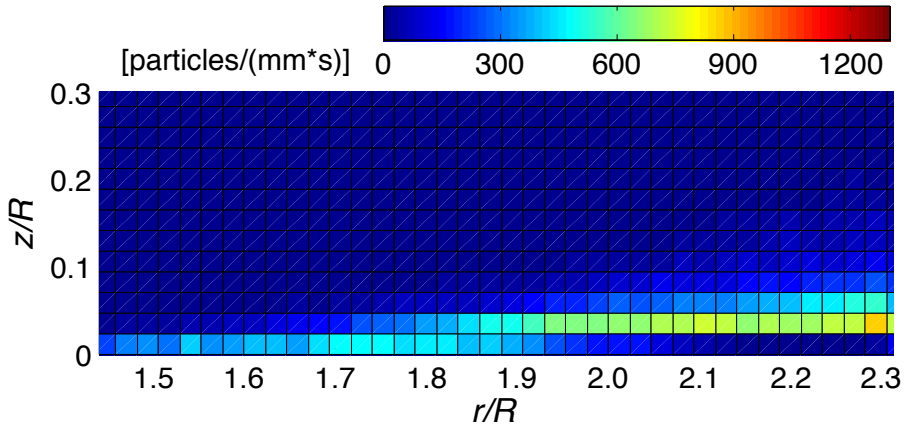

Figure 3.12: Time-averaged wall-normal particle flux as produced by the 0.17 m-diameter rotor in the ROI shown in Fig. 3.10.

(and so the reason for particle flux along the bed) lies upstream of the region where the streamwise sediment flux is measured to be most intense, i.e., upstream of $1.9R$.

For $r/R > 1.9$ the particle fluxes could not be measured close to the sediment bed because of image saturation, i.e., the PTV algorithm could not detect the individual particles in the dispersed phase. This latter problem also makes it difficult to extract carrier-phase information because the PIV interrogation windows will be saturated with sediment particles, making it impossible to cross-correlate the carrier-phase tracer particles. Therefore, carrier-phase data could not be obtained further downstream near the wall, i.e., for $r/R > 2.2$.

Figure 3.12 shows the time-averaged particle flux in wall-normal direction. If such a vertical particle flux is measured at or just above a sediment bed, it is often referred to as dust or particle emission rate, i.e., it is a measure of the number of particles that are picked up from the sediment bed and entrained into the flow. Because of image saturation, the particle flux in wall-normal direction just above the sediment bed could not be measured for downstream distances greater than $1.9R$.

Although Fig. 3.10 only shows an instantaneous flow realization, it illustrates one mechanism as to how particles can be entrained above the sediment bed at greater downstream distances, which is by the effects produced by a coherent vortex structure. It can be seen from Fig. 3.12 that the wall-normal particle flux is almost negligible at locations relatively far upstream, i.e., closer to the rotor. However, the wall-normal particle flux builds up with increasing distance from the rotor, and has its most intense region between $r/R = 2.1$–2.3 with a global maximum in this ROI at $r/R = 2.28$.

3.2.3 Reynolds Stress Distributions near the Ground

Figures 3.13 and 3.14 show the radial distributions of all components of the ensemble-averaged Reynolds stress tensor as well as the turbulent kinetic energy, k, for the single-phase flow, and for the carrier phase in the dual-phase experiment when using the smaller (0.17 m-diameter) rotor system. The turbulence intensities were all normalized by the hover induced velocity, v_h, and they are plotted as a function of downstream distance from the rotor centerline for several heights above the ground, z/R. For the carrier phase, measurements could not be made to as close to the ground as for the single-phase flow. Again, for $r/R > 2.2$, image saturation in the dual-phase flow environment made it impossible to extract good results for the points nearest to the wall.

The two trends shown in the single-phase and the dual-phase flow were: 1. The turbulence intensities in the fluid flow increased with wall-normal distance, and 2. That the turbulence intensities also decreased with radial distance after they reached their maximum values, which was upstream of $r/R = 1.9$ in both cases. However, all ensemble-averaged turbulence quantities of the carrier phase (Fig. 3.14) revealed remarkable differences to their corresponding values in the single-phase flow results (Fig. 3.13). The carrier phase showed significantly greater spatial excursions in the turbulence properties near the sediment bed.

The streamwise Reynolds stresses, $\overline{u'^2}$, were found to be the predominant

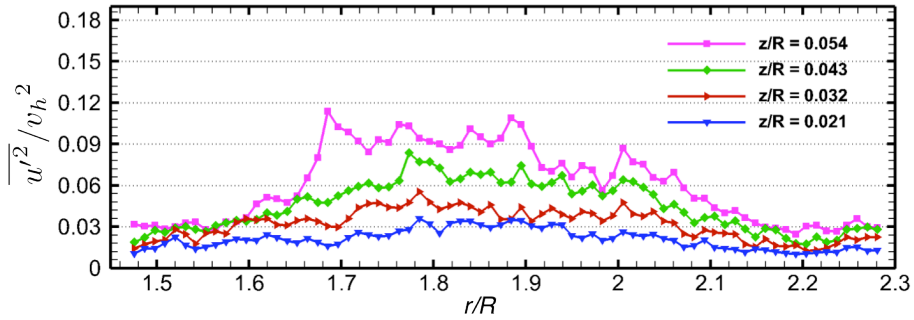

(a) Streamwise Reynolds stress

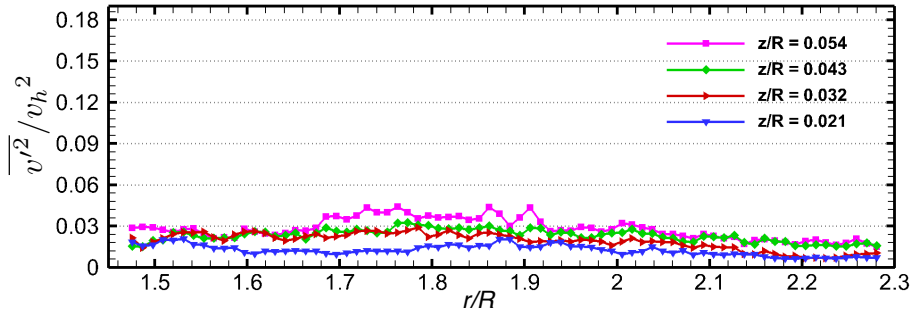

(b) Wall-normal Reynolds stress

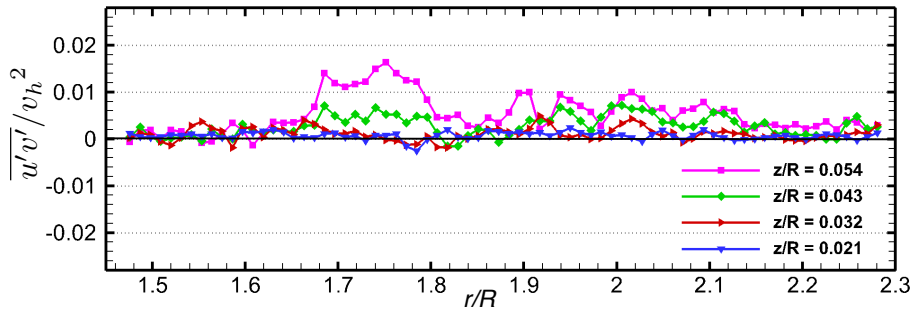

(c) Reynolds shear stress

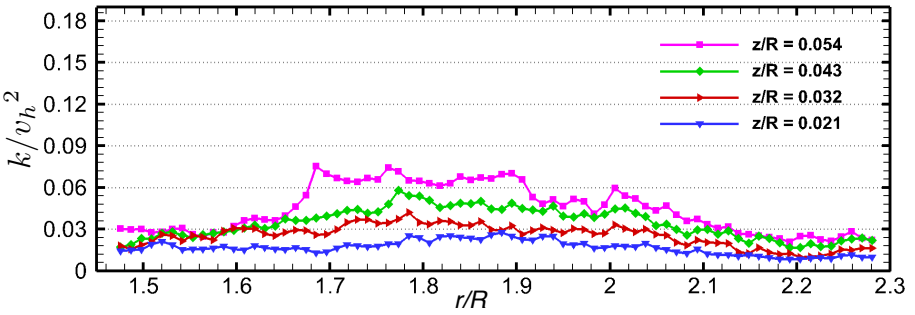

(d) Turbulent kinetic energy

Figure 3.13: Components of the Reynolds stress tensor and turbulent kinetic energy normalized by the theoretical hover induced velocity, v_h, for several heights above the ground plane, z/R, in the single-phase flow.

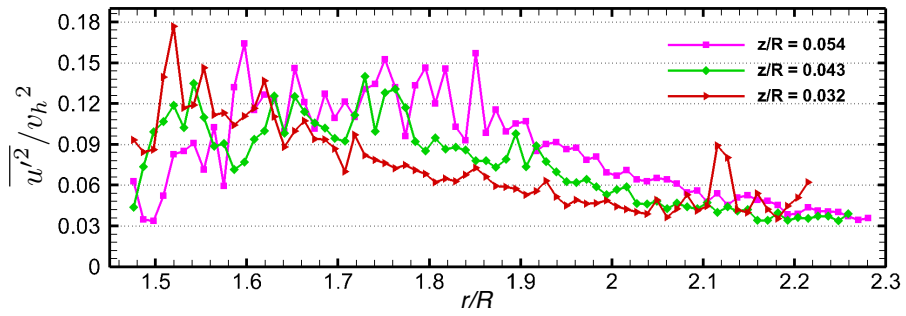

(a) Streamwise Reynolds stress

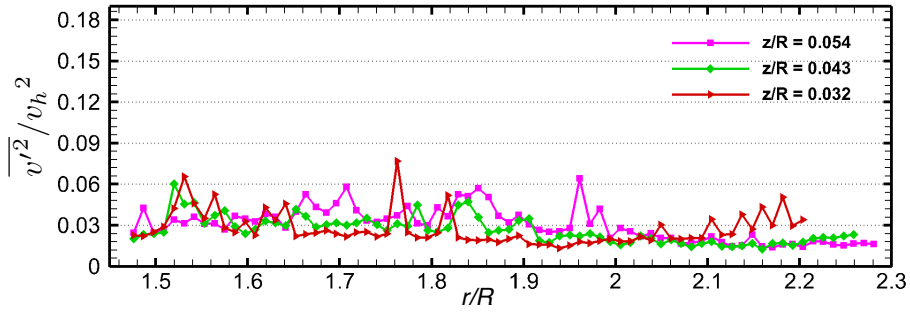

(b) Wall-normal Reynolds stress

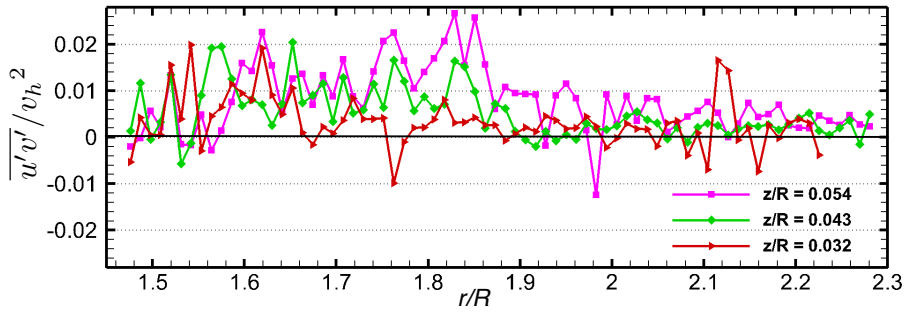

(c) Reynolds shear stress

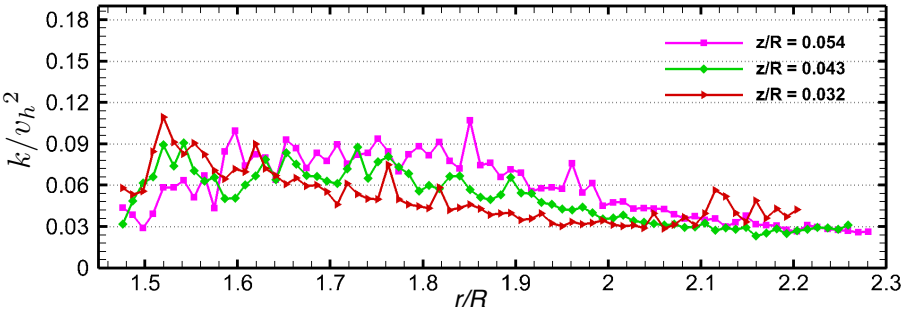

(d) Turbulent kinetic energy

Figure 3.14: Components of the Reynolds stress tensor and turbulent kinetic energy normalized by the theoretical hover induced velocity, v_h, for several heights above the sediment bed, z/R, for the carrier in the dual-phase flow.

turbulent stresses in the near-wall region above the ground plane or near the sediment bed. Therefore, they were also the primary source of turbulent kinetic energy, i.e., $k = 0.5(\overline{u'^2} + \overline{v'^2})$ in this case. This outcome is readily seen when comparing the results for the turbulent kinetic energy to the corresponding $\overline{u'^2}$ distribution that was measured in both the single-phase and the dual-phase flow environments; the general trends shown in these two turbulence quantities were the same. In light of the very small wall-normal Reynolds stresses, especially for the single-phase flow measurements, this outcome was expected. Notice (in both cases) that the magnitudes of the shearing components of the Reynolds stresses were significantly smaller than the streamwise and wall-normal Reynolds stresses, being about one order of magnitude smaller than the prevailing normal Reynolds stresses in the streamwise direction, i.e., $\overline{u'^2}$.

Compared to the other components of the Reynolds stress tensor, the streamwise turbulent perturbations and the associated streamwise Reynolds stresses correlated best with the observed particle mobilization and sediment transport along the bed. This result is consistent with the findings of Nelson et al. [62] and Sterk et al. [52], who investigated channel and aeolian flows, respectively. Such a conclusion can be drawn from a comparison of the time-averaged streamwise particle flux (Fig. 3.11) to the time-averaged (or ensemble-averaged) streamwise Reynolds stress in both the single-phase and dual-phase flow; see Figs. 3.13 and 3.14, respectively.

In both cases, the streamwise Reynolds stresses were noted to be greatest upstream of $r/R \approx 2.0$ and decreased downstream. Recall that the distribution of streamwise particle flux (Fig. 3.11) showed a sharp increase downstream of $r/R = 1.8$, the location of the maximum particle flux being at $r/R = 1.9$–2.0. As stated earlier,

the root cause for the initial mobilization of particles (and so the reason for particle flux along the bed) must lie upstream of the region where the streamwise sediment flux is measured to be the most intense, i.e., upstream of $1.9R$. Therefore, the streamwise Reynolds stresses were found to correlate well with sediment mobilization on the bed. Although the Reynolds stresses are, in part, induced by the concentrated vorticity in the tip vortices, the onset of sediment motion was found to be associated with the higher levels of streamwise turbulent stresses and not with the local action of the coherent vortex structures themselves.

The average stress component $-\rho\,\overline{u'v'}$ gives the two-dimensional turbulent shear stress and has often been directly correlated to the sediment transport dynamics [121]. Therefore, sediment uplift models usually consider only this component of the Reynolds stress tensor while neglecting the other components. However, in more recent studies it has been shown that such assumptions are questionable for riverine flows [52, 121] because of the predominant component of streamwise turbulent stress, $\overline{u'^2}$.

It was also shown by the present measurements that the normal Reynolds stress in the streamwise direction is the most significant component of the Reynolds stress tensor for the region at the ground below the rotor, and in both the single-phase and dual-phase flow environment; see Figs. 3.13 and 3.14, respectively. Therefore, the streamwise Reynolds stress cannot be neglected in the development of sediment mobilization and entrainment models that will be applicable to rotor flows. Furthermore, in existing sediment transport and uplift models [75, 80, 81] only the ensemble-averaged Reynolds stresses have been considered, but the particles will also

experience the consequences of the fluctuating velocities and instantaneous stress components.

The Reynolds stresses are unlikely to be responsible for the pickup of particles further downstream because all components of the Reynolds stress tensor decrease downstream of $r/R = 2.0$, while the vertical particle flux increases; see Fig. 3.12. This is the case for both the single-phase flow and the carrier in the dual-phase experiment; see Figs. 3.13 and 3.14, respectively.

3.2.4 Time-History of Turbulence Events Related to Particle Uplift

Because the shown ensemble-averaged turbulence quantities cannot help explain the occurrence of sediment pickup, the instantaneous turbulence quantities, namely the instantaneous fluctuation velocities and the corresponding instantaneous Reynolds stresses, were examined. Of particular interest was the region further downstream ($r/R > 2.2$) because this region had the greatest particle flux in the wall-normal direction; see Fig. 3.12.

The time-history of the instantaneous Reynolds stress components for a measurement point located at $r/R = 2.28$ just above the sediment bed was examined, as shown in Fig. 3.15. In fact, at this radial distance from the rotor centerline the global maximum of the time-averaged wall-normal sediment flux was measured. Also shown is the instantaneous wall-normal particle flux at the same spatial location. This component of the particle flux is used to correlate any particle uplift with

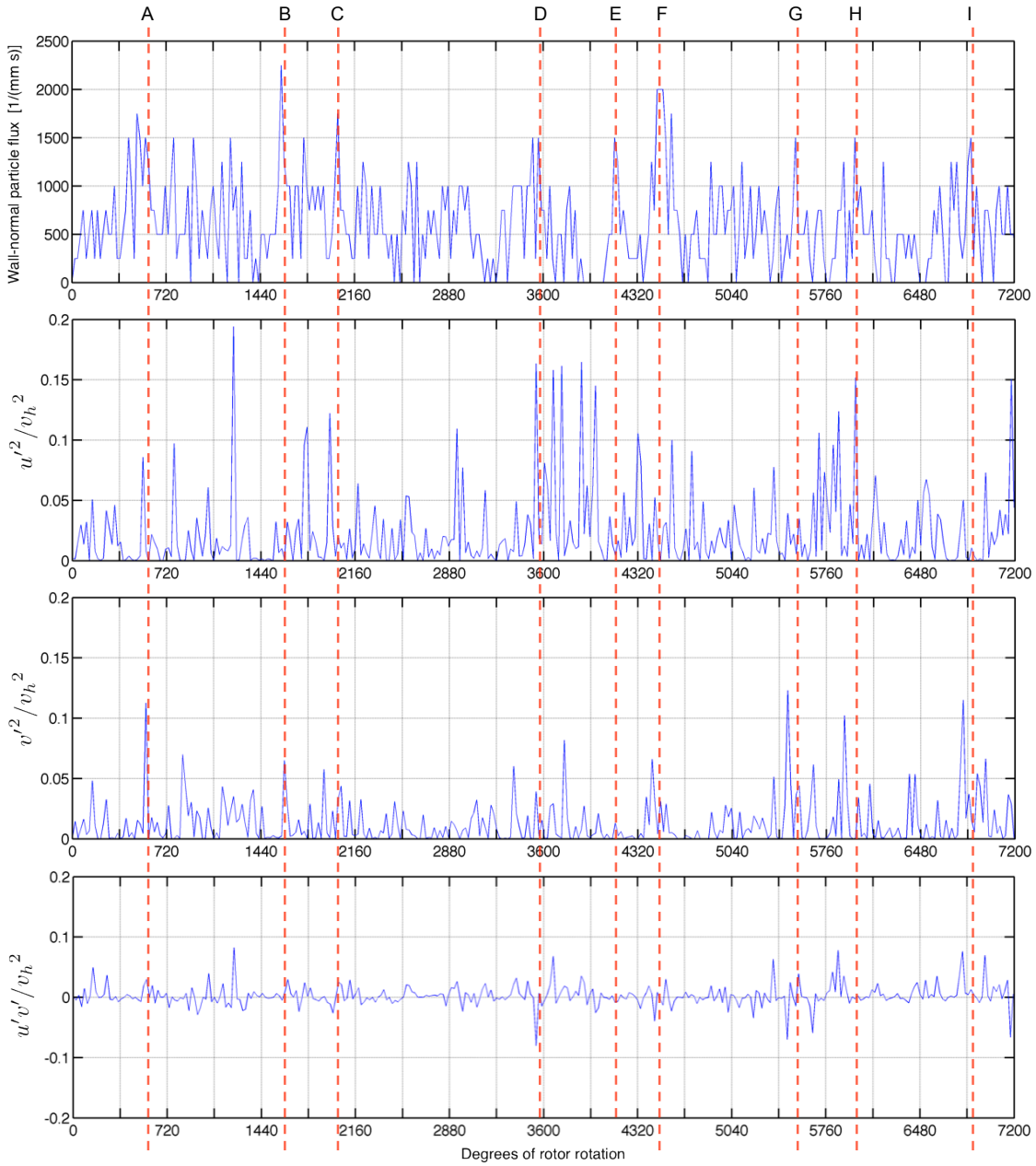

Figure 3.15: Instantaneous wall-normal particle flux, and components of the instantaneous Reynolds stress tensor for the carrier phase in the dual-phase rotor flow experiment, all measured at $r/R = 2.28$ just above the sediment bed and normalized by the theoretical hover induced velocity, v_h.

the instantaneous turbulent stresses, i.e., with the discrete turbulence events that occurred mostly in phase with the periodic passage of the tip vortices over the particle bed.

Peak values of wall-normal particle flux (or particle uplift) were seen to correlate well with discrete turbulence events in the carrier flow. Such turbulence events are represented by pronounced peaks in the time-histories of the instantaneous Reynolds stresses, as shown in Fig. 3.15. The particle bursts that could be correlated to carrier-phase turbulence events are marked by lines A–I. All components of the two-dimensional instantaneous Reynolds stress tensor contributed to such a particle burst, i.e., the two normal stress components as well as the shear stress. In most instances, more than one of the Reynolds stress components was noted to contribute to the pickup of particles from the sediment bed. A delay in the particle response to the turbulence events was also noticed, which in some instances was very pronounced. Recall that the measurement sampling rate in this experiment was 1,000 Hz, and so what may appear as a relatively large shift of a peak in the time-histories is actually only few milliseconds of time.

3.2.5 Quadrant Analysis and Joint Frequency Distributions of Turbulence Events

Further insight into the structure of the turbulence at the ground may be gained by using the quadrant analysis method. This technique can further characterize

the turbulence based on organized turbulence structures that are present in wall-bounded turbulent flows. The quadrant analysis shows the correlative structure of the perturbation velocities u' and v', which have been described previously. Wallace et al. [59] showed that there were four kinds of turbulence events, namely sweeps, ejections, outward and inward interactions, and these four distinct turbulence events each had a more or less pronounced contribution to the Reynolds stresses. The four types of motion are classified by the signs of the perturbation velocities, u' and v'. The measurements are then plotted on a quadrant map, as shown in Fig. 3.16. A quadrant map essentially shows the main directions of the turbulent momentum transfer relative to the bulk movement of the fluid.

For the near-wall region of channel flows [83, 89, 122] and other canonical

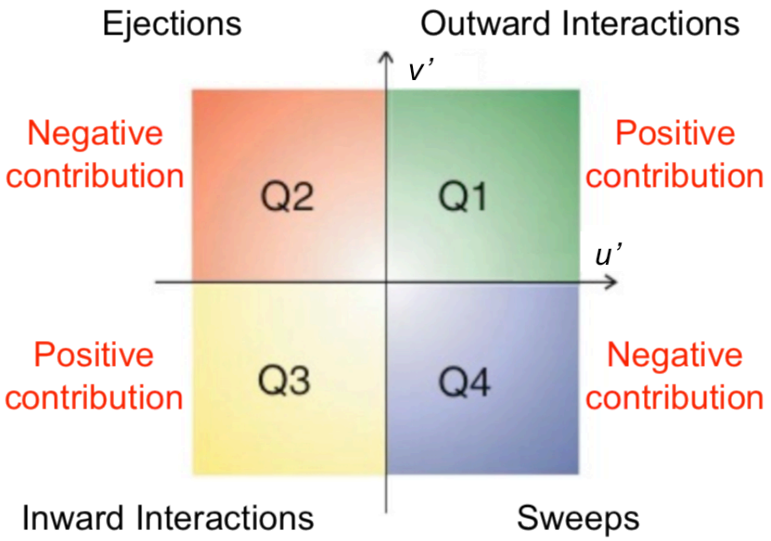

Figure 3.16: A quadrant map showing the four types of motion (turbulence events) belonging to the quadrants and their contribution to the Reynolds shear stresses, $\overline{u'v'}$.

flows such as the turbulent boundary-layer flow over a flat plate [59, 60], a certain organized structure of the fluid turbulence events into the quadrants has been reported. These organized turbulent motions have also been seen in atmospheric boundary layers [52, 64, 67] and riverine flows [121], with particle transport being correlated to discrete turbulence events in some instances. The interactions between sediment motions and the turbulence structure of the carrier phase and how they correlated to the four types of turbulence events, has been studied by Nelson et al. [62] for riverine flows. There are significant differences in the time scales, turbulence levels, Reynolds numbers, and spatial dimensions between channel flows or riverine flows and the rotor flow (i.e., the brownout problem). However, the quadrant analysis is still useful for examining the turbulence characteristics of the carrier phase as it pertains to the sediment uplift, entrainment, and suspension mechanisms that may contribute to the development of a brownout dust cloud.

An example of a quadrant plot is shown in Fig. 3.17. Each data point represents a turbulence event for one spatial location and for one point in time. In this case, the measurement point was located at $r/R = 1.70$ just above the sediment bed, and the data obtained from this location were extracted from the carrier phase over time and then plotted on the quadrant map. The advantage of this form of presentation is in that every single measurement point is represented. However, it may still be difficult to distinguish a pattern or any organization of flow events. Because information about a preferred statistical organization of turbulence events is of more interest, the probability density for the turbulence events is shown; see Figs. 3.18 and 3.19. Such probability density distributions (or joint frequency distributions) show the

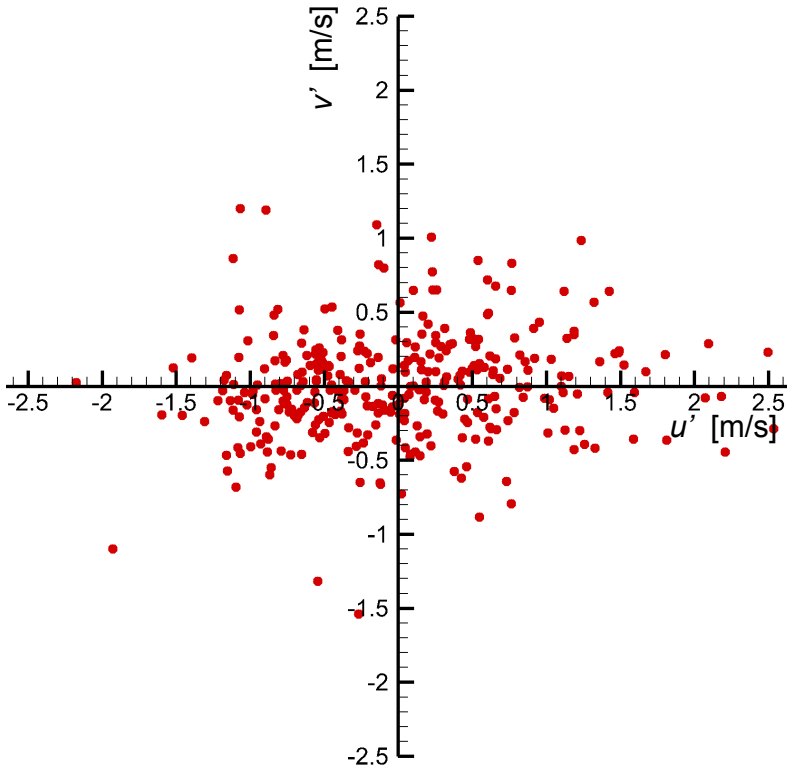

Figure 3.17: Scatter quadrant plot showing combinations of the carrier-phase velocity fluctuations obtained from contiguous PIV realizations at $r/R = 1.70$, $z/R = 0.03$.

frequency or likeliness with which turbulence events occur.

It has been pointed out [52] that the sampling frequency of the data recorded may have a significant effect on the distribution of turbulence events into the quadrants, i.e., on the likeliness that a turbulence event will fall into one quadrant or another. The reason is that the organized turbulence motions have certain time scales and recur at a certain frequency, depending on the nature of the flow being investigated. Therefore, the nature of turbulence in the flow cannot be resolved accurately with inadequate sampling rates. For example, aliasing may occur if too

low a sampling frequency is used. Ultimately, the specific nature of the flow in question will always dictate the optimum sampling rate for the measurements to be performed.

While the quadrant analysis method has been mostly applied to data measured at much lower sampling rates than $1,000$ Hz, the flows that have been previously investigated were mostly open channel flows, riverine flows, and atmospheric boundary layers (which can have a thickness of the order of 10 m or more). These latter flows have considerably larger time and length scales, and so the measurements must be acquired at a much lower rate and for a longer period. Because the present work gives much insight into the actual structure of the turbulence phenomena occurring in this case, including information about the time and length scales associated with the rotor flow in the laboratory environment, the outcomes may enable future measurements at judicious sampling rates more suitable for the specific flows under investigation.

A preferred organization of turbulence events is not apparent from Figs. 3.18 and 3.19. However, an elongated or stretched distribution in the streamwise direction was observed in the joint frequencies of the turbulence events for some downstream distances where most of the particles on the bed were mobilized, i.e., between $1.9R$ and $2.0R$; see Fig. 3.11. Downstream of this region, the turbulence appears more isotropic, which is because of the more homogeneous organization of turbulence events in the four quadrants. Upstream of the position of maximum wall-parallel sediment motion ($r/R \leq 1.7$) the turbulence was more isotropic in the single-phase flow. However, for the carrier phase in the dual-phase flow, the streamwise fluctuation velocities (positive and negative) near the sediment bed prevailed throughout the

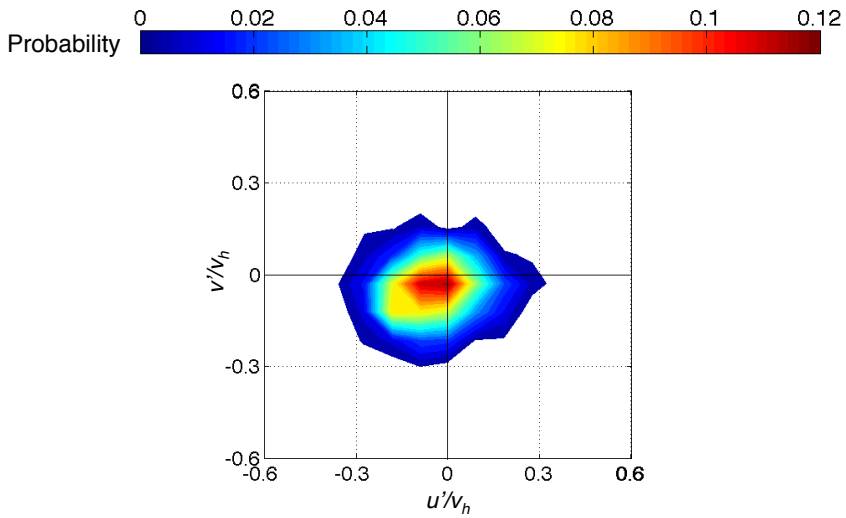

(a) $r/R = 1.70$

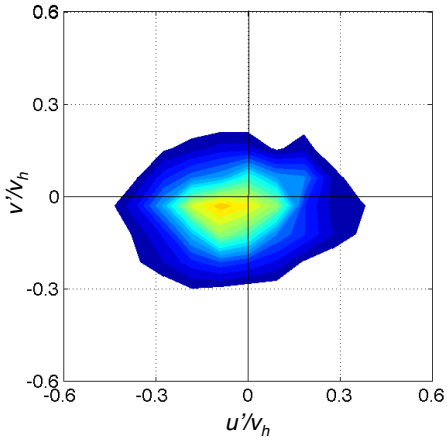

(b) $r/R = 1.90$

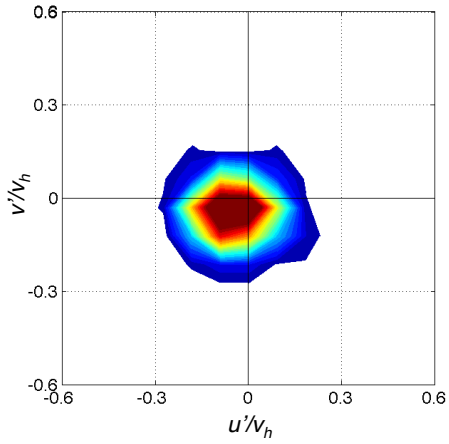

(c) $r/R = 2.20$

Figure 3.18: Joint frequency distributions of turbulence events for the single-phase flow at $z/R = 0.03$.

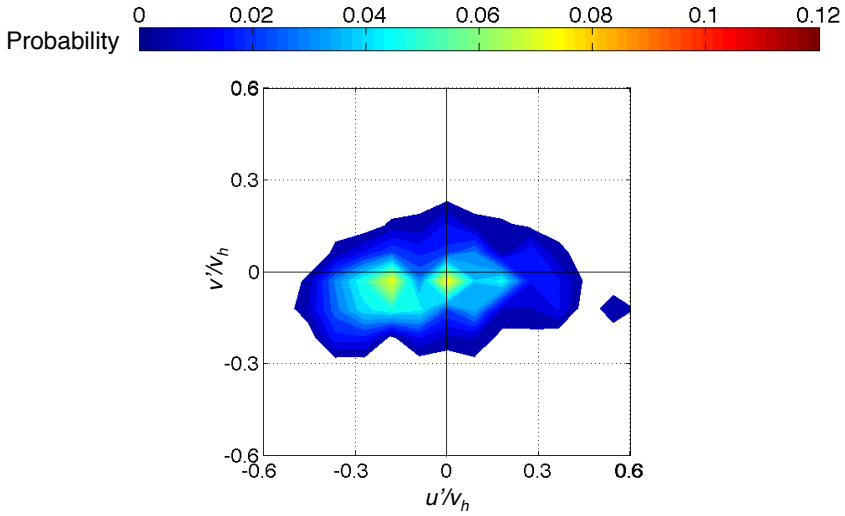

(a) $r/R = 1.70$

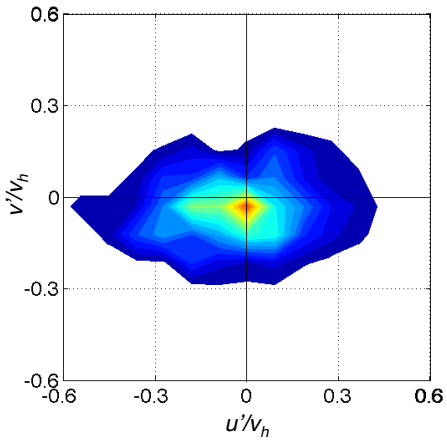

(b) $r/R = 1.90$

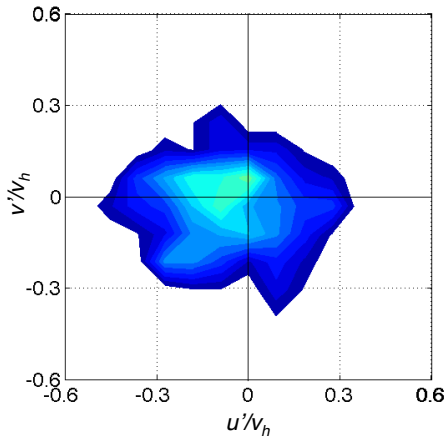

(c) $r/R = 2.20$

Figure 3.19: Joint frequency distributions of turbulence events for the carrier in the dual-phase flow at $z/R = 0.03$.

entire ROI. This outcome was also seen in the ensemble-averaged Reynolds stress distributions for the wall-nearest measurement points, as shown in Fig. 3.14.

3.3 Flow Phase Couplings and Turbulence Modifications

Single-phase and dual-phase flow experiments were conducted under the otherwise same external flow conditions. The results were then analyzed comparatively to understand how the addition of the dispersed particle phase affected the fluid (carrier) flow, i.e., to investigate the extent and nature of potential two-way coupling of the flow phases. A contiguous time-history of the rotor-induced flow could be obtained from the blades through the interaction of the flow with the ground or sediment bed, and to the eventual distortion of the vortices and diffusion of the wake further downstream.

The relatively high spatio-temporal resolution of these measurements allowed not only an investigation of the modulation of the carrier mean turbulence quantities by the dispersed particles, but it also enabled an assessment as to the cause of the turbulence modifications, i.e., the mechanisms by which the individual flow structures were influenced by the action of the particles were investigated. All of the present results are planar (two-dimensional) realizations of the flow in the plane of the laser light sheet, which was aligned to be perpendicular to the ground plane and intersecting the rotor shaft axis; see Fig. 2.7.

3.3.1 Carrier Mean Velocities in the Single- and Dual-Phase Flows

Figure 2.11 shows how the initially downward flow (toward the wall) induced by the rotor is sharply turned radially outward when it approaches the ground plane (or sediment bed), as it is typical for the mean rotor flow in ground effect operation [3, 39, 44]. The flow then develops into a type of turbulent wall jet as it develops along the ground plane, although such a flow still contains significant discrete vorticity that was carried there by the blade tip vortices and vortex sheets.

Figure 3.20 shows the mean streamwise (wall-parallel) single-phase (identified by SP) and dual-phase (identified by DP) flow velocity profiles for the carrier phase (i.e., the air flow) normalized by the standard (theoretical) hover induced velocity, v_h, as given by Eq. 2.9. In this case, the results are shown for two radial locations away from the rotational axis of the rotor. These measurements were taken in ROI 2 because this region could be interrogated in more detail with higher spatial resolution. Closer to the rotor (r/R = 1.2 in this case), the flow was still in the process of turning from a mostly vertical (wall-normal) to a radial flow along the wall (more parallel to the ground plane); see Fig. 2.11. For locations further downstream (r/R = 2.2 in this case), the flow along the ground plane appeared to develop in a manner similar to that of a classical wall jet [112, 116]. The mean values of the wall-parallel velocity, $\overline{u}$, represent ensemble time-averages that used 1,000 contiguous vector fields that were calculated from the 1,000 corresponding PIV image pairs recorded every 30° of blade rotation.

Upstream and closer to the rotor, the enhanced mixing caused by the mobilized

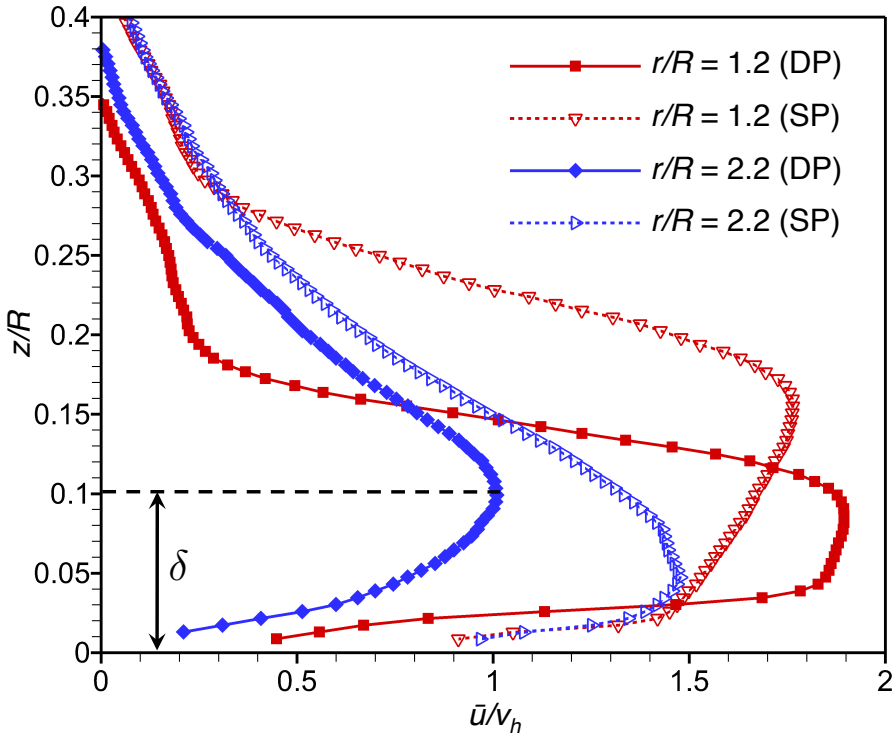

Figure 3.20: Mean wall-parallel velocity profiles for the single-phase (SP) and the carrier of the dual-phase (DP) flow at two radial distances from the rotor.

particles in the flow leads to a quicker momentum transfer between the higher-velocity outer layers of the wall jet and the lower velocity of the inner layers, these being also decelerated by the presence of particles near the wall. The enhanced mixing yielded a somewhat quicker development of the boundary layer, so that the maximum velocities were located closer to the bed compared to what was found in the single-phase flow measurements without the sediment. Additionally, the accumulation of mobilized particles near the sediment bed further downstream (see Fig. 3.21) may also influence the flow upstream ($r/R = 1.2$ in this case), in that significant particle concentrations downstream may introduce a blockage effect that alters the flow further upstream.

Note that the boundary layers thickness, δ, was defined as for a canonical wall jet, i.e., the wall-normal distance of the position where the maximum (wall-parallel) velocity occurred; see Fig. 3.20.

Further radially downstream from the rotor, the streamwise velocities of the carrier phase in the dual-phase measurements were found to be much lower than those measured in the single-phase flow. Also, the wall-normal extension of the region containing decelerated fluid was greater, i.e., the boundary layer at the ground in the dual-phase flow was significantly thicker after it had developed. In some cases this boundary layer was up to 50% thicker, depending on the downstream location.

The measured particle concentrations in the flow indicated that the preponderance of particles that were suspended in the main flow were in regions relatively far downstream from the rotor; see Fig. 3.21. Therefore, the lower streamwise components of the mean velocities produced in the dual-phase flow for regions further downstream can most likely be attributed to the momentum exchange between the carrier and dispersed phases of the flow.

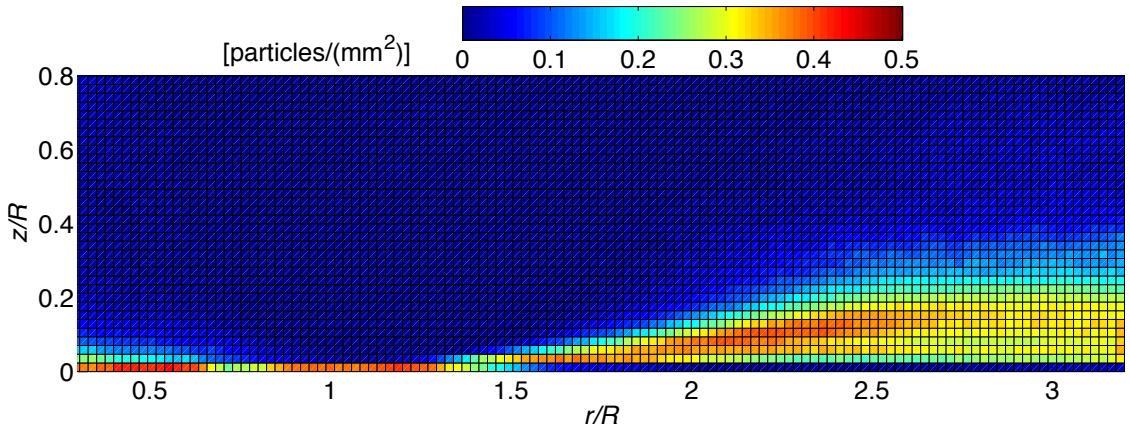

Figure 3.21: Time-averaged particle concentration in ROI 1.

3.3.2 Vortical Structure of the Flow

A contiguous time-history of the developing rotor wake in the single-phase and dual-phase flow is shown in Figs. 3.22 and 3.23, respectively. Instantaneous fluid velocity vectors for every other vector field realization, i.e., for every other time-step, are shown on background contours of the out-of-plane vorticity, ω_y, as defined in Eq. 2.1. Any high vorticity regions very close to the rotor plane (at $z/R \approx 0.9$ for $r/R < 0.9$) are an artifact of laser light reflections from the rotor blades. In the actual experiments a greater field of view was obtained than it is shown here; see previously in Fig. 2.11. Notice also that the particle sizes in these and in any following images are exaggerated for clarity.

The tip vortices contain high levels of positive vorticity (shown in dark red). The high spatial resolution of these instantaneous realizations of the flow also allowed for the vortex sheets to be resolved as they trailed from the rotor blades. These vortex sheets (or turbulent wake sheets) contained a type of Taylor–Görtler vortices [119], their counter-rotating characteristics being indicated by the alternating positive/negative (red/blue) vorticity contours. The eddies contained in the vortex sheet also increased the turbulence in the near-wake behind the blade, a behavior that will be discussed later in Section 3.3.3.

Notice that the turbulent vortex sheets convected faster downstream than the associated tip vortices, although the actual behavior of the sheet will be a function of the blade geometry and its operational state [3, 119]. In this case, the vortex sheets were partially entrained into the tip vortex that they were initially associated

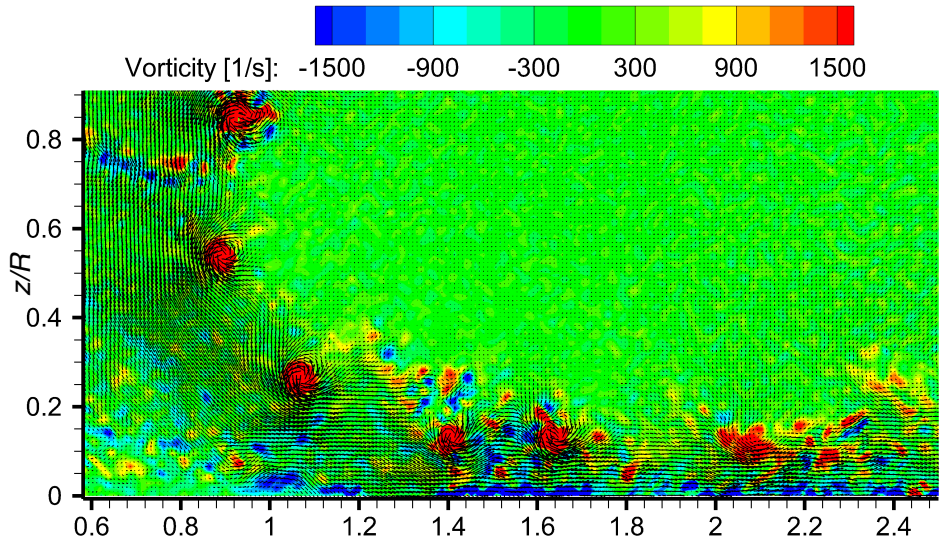

(a) Blade azimuth angle $\psi_b \approx 30°$

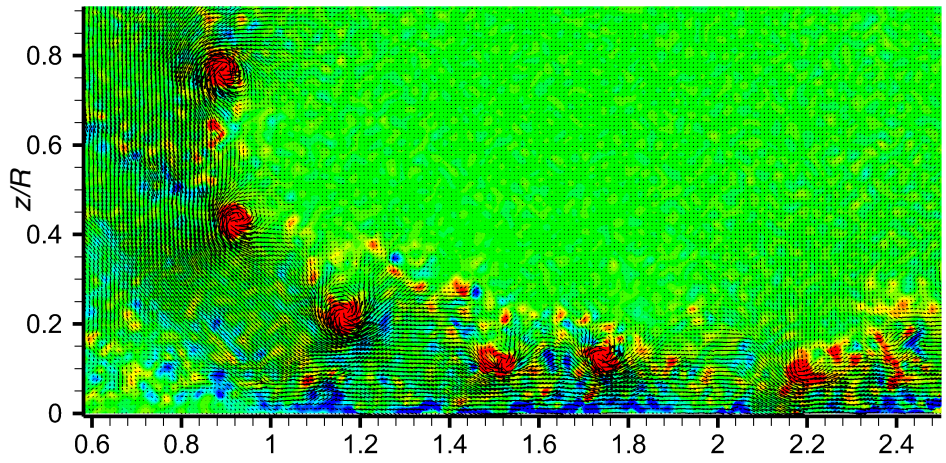

(b) Blade azimuth angle $\psi_b \approx 90°$

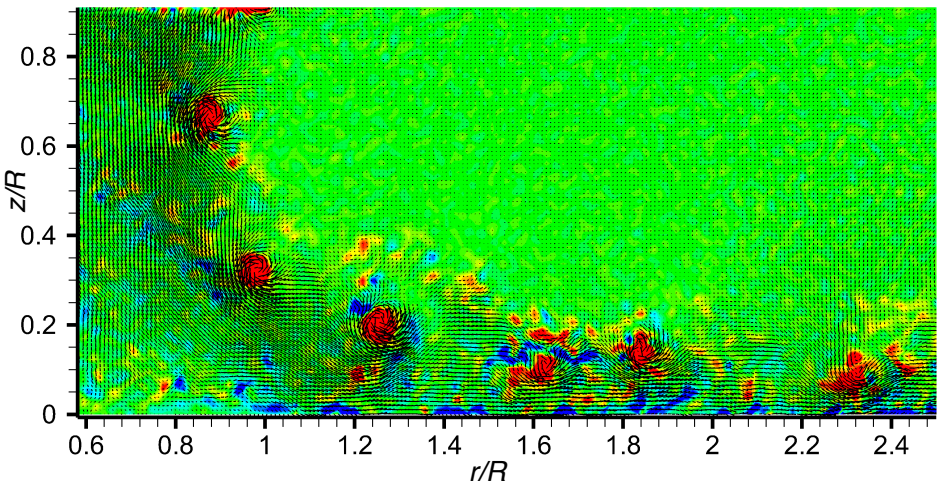

(c) Blade azimuth angle $\psi_b \approx 150°$

Figure 3.22: Contiguous time-history of the single-phase flow measured below the rotor, showing every second velocity vector field.

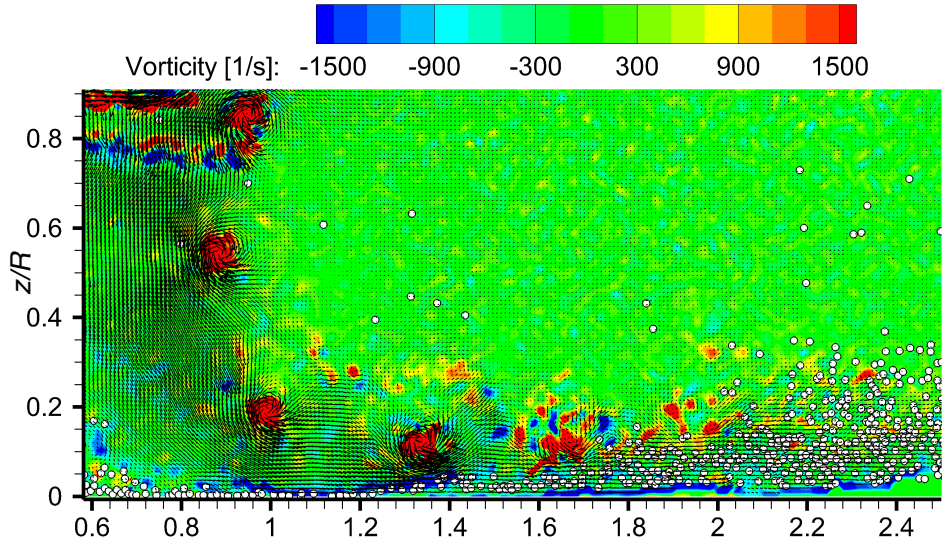

(a) Blade azimuth angle $\psi_b \approx 30°$

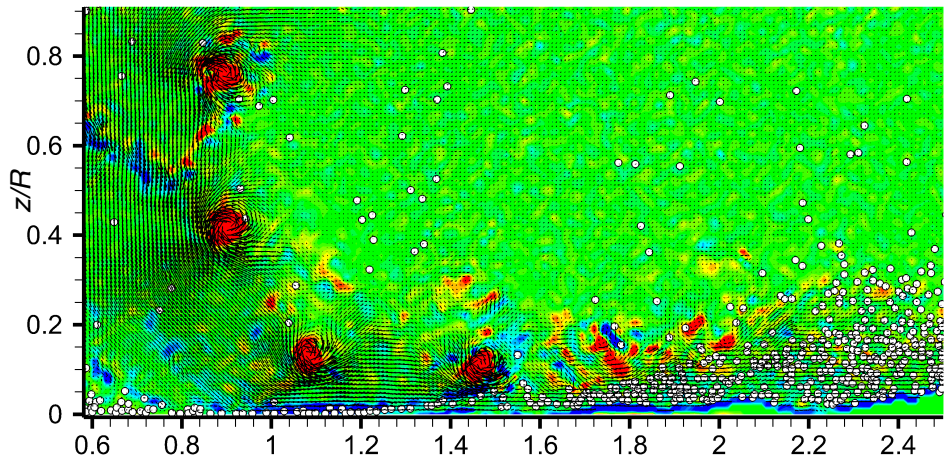

(b) Blade azimuth angle $\psi_b \approx 90°$

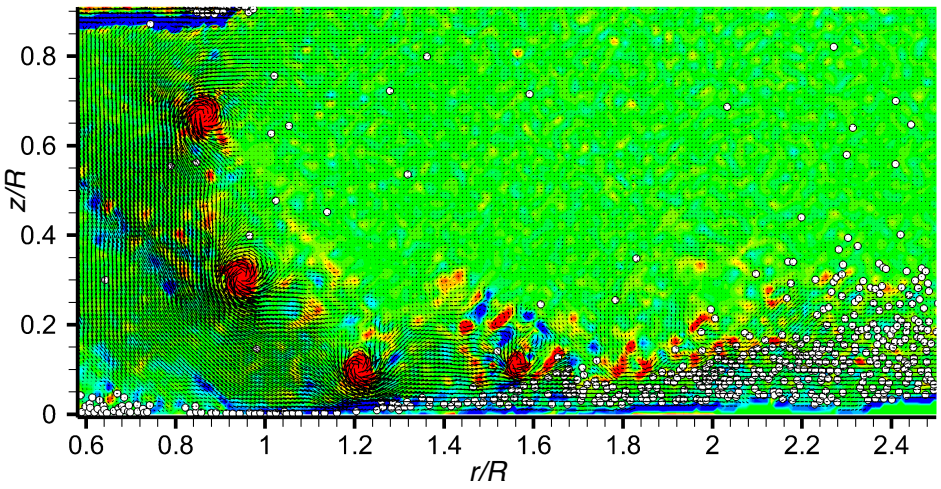

(c) Blade azimuth angle $\psi_b \approx 150°$

Figure 3.23: Contiguous time-history of the dual-phase flow measured below the rotor, showing every second velocity vector field. Particle sizes exaggerated for clarity.

with (i.e., the tip vortex that was produced at the same blade azimuth angle), and partially into a tip vortex that had been produced by the preceding rotor blade; see Figs. 3.22 and 3.23. The turbulent eddies in these sheets appeared to have little effect on the younger tip vortices that were only one or two rotor revolutions old, but in some cases it was seen that the eddies were stretched and relaminarized when they were entrained into the vortex cores [44, 119, 123].

As the vortex sheet was convected further downstream, its predominantly negative vorticity was entrained into the near-wall flow; see Figs. 3.22 and 3.23. In some instances, the negative vorticity from the ground was picked up by the tip vortex that contained positive vorticity; see Figs. 3.23 and 3.24. This behavior was observed to affect the older vortices closer to the ground, leading to their quicker diffusion (e.g., Fig. 3.24), which will be discussed in more detail in Sections 3.3.3 and 3.3.4.

The increased local flow velocities that were induced by the tip vortices as they approached the ground induced higher velocity gradients and shear on the sediment bed, which generally correlates to more mobilized particles. The production of secondary (negative) vorticity directly below the tip vortices was observed in both the single-phase and the dual-phase flows; see Figs. 3.22 and 3.23, respectively. This negative vorticity, together with the entrained negative vorticity from the turbulent wake sheet as previously described, was a source of initial uplift of the particles, often resulting in sudden discrete bursts of particle ejections upward away from the bed; see Figs. 3.23 and 3.24. It has been observed previously that any negative vorticity produced near a sediment bed can contribute to the processes of

particle mobilization and pickup [110], however, this effect has not been previously documented for rotor-induced flows.

The instantaneous realizations of the flow in Fig. 3.23 indicated that the initial pickup of particles from the bed occurred mostly between $r/R = 1.2$–1.5, which can also be compared to the measured particle concentrations shown in Fig. 3.21. Although the initial pickup was observed at $r/R = 1.2$–1.5, it was not until greater downstream distances that the particles were actually convected to significant heights above the bed and into the main rotor flow. The region $r/R = 1.2$–1.5 on the bed also appeared to be where the negative vorticity contained in the carrier phase was convected away from the bed by the (still at this stage) coherent tip vortices.

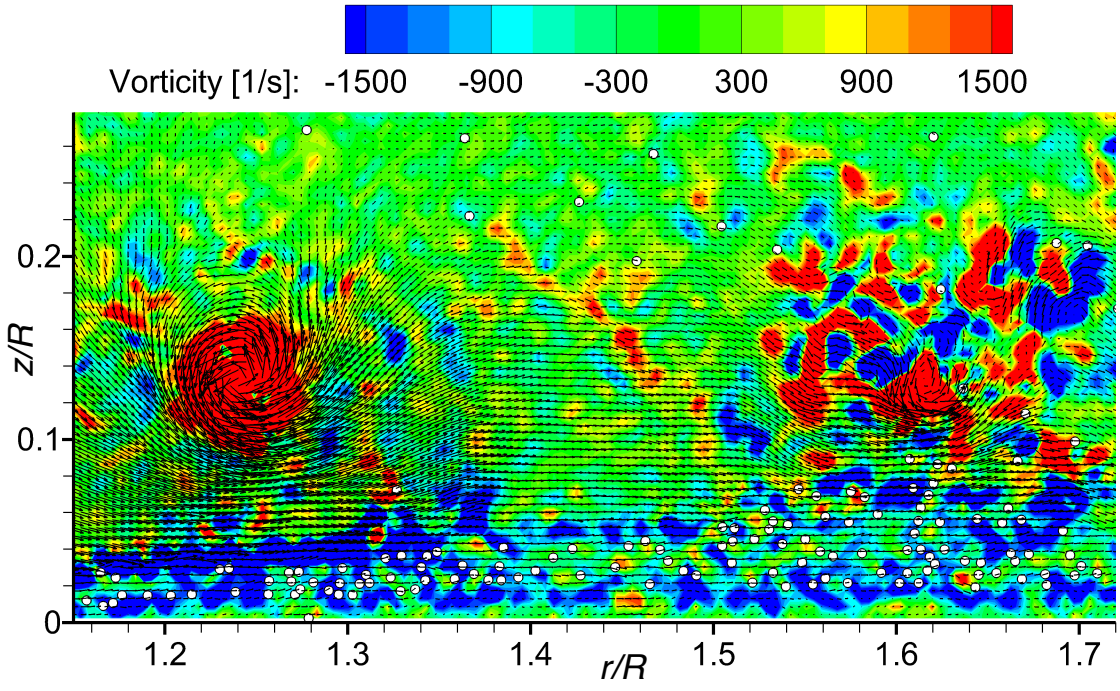

Figure 3.24: Instantaneous dual-phase flow realization in ROI 2, contouring the out-of-plane vorticity and illustrating the distortion of the coherent tip vortex near the ground. The younger vortex has a wake age of $\zeta = 540°$.

To further understand this behavior, the corresponding region was analyzed more closely in a smaller field of view (ROI 2), thereby giving a much finer spatial resolution in the measurements; see Fig. 3.24. These results show how the particles were entrained into the vortex flow and how the negative vorticity from the ground (when entrained into the vortices) acted to distort the viscous cores; in this case this distortion was initiated adjacent to the bed at a downstream distance of $r/R \approx 1.4$. This location also coincided with the approximate downstream location where the tip vortices were closest to the bed, thereby causing the initial pickup of particles near this location; see Figs. 3.21, 3.23(a) and (b).

Downstream of $r/R \approx 1.4$ in the dual-phase flow, it was observed that the vortices diffused, eventually breaking up into smaller vortical structures; see Figs. 3.23 and 3.24. This behavior was followed by the relatively quick diffusion of most of the remaining vorticity, a process that was accelerated by the presence of suspended particles downstream of $r/R \approx 1.8$; see Fig. 3.23. However, without the sediment particles in the flow, the vortices stayed coherent to older wake ages (i.e., to greater downstream distances from the rotor); see the corresponding single-phase flow realization in Fig. 3.25 compared to the dual-phase realization at the same wake age, as shown in Fig. 3.24.

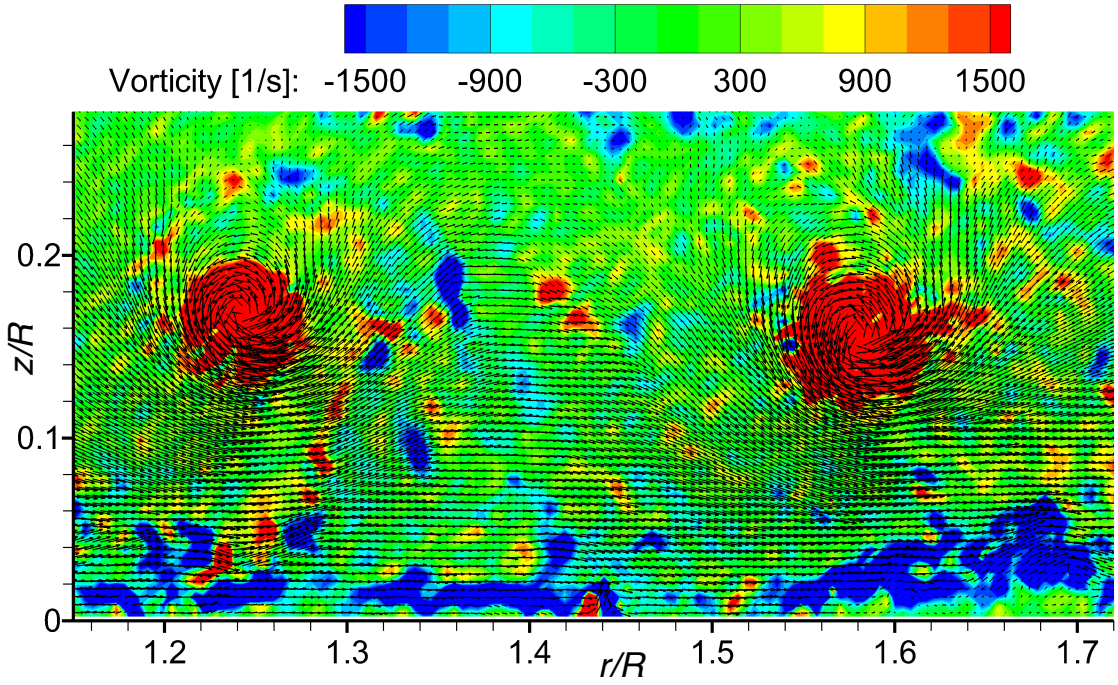

Figure 3.25: Instantaneous single-phase flow realization in ROI 2, contouring the out-of-plane vorticity. The younger vortex has a wake age of $\zeta = 540°$.

3.3.3 Turbulence Intensities in the Flow Field below the Rotor

The turbulence intensity is one measure of the effect of turbulent structures, such as eddies and larger coherent vortical structures. Although Reynolds-averaging techniques do not explicitly account for coherent motions in the flow, some instantaneous organization is apparent in the averaged terms. It is known that sediment motion arises, at least in part, from the effects of turbulence intensities and turbulent (Reynolds) stresses [49].

To calculate the turbulence quantities, the fluctuating parts of the fluid velocities

were extracted from the PIV measurements by means of a Reynolds decomposition using Eqs. 3.1 and 3.2. In this case, 1,000 contiguous instantaneous fluid velocity vector maps were used to obtain the local time-averaged fluid velocities for the Reynolds decomposition using Eq. 3.3. The turbulence intensities in the streamwise and wall-normal directions, T_u and T_v, and the turbulent kinetic energy, k, were calculated from the two in-plane components of the velocity fluctuations using

$$T_u = \frac{\sqrt{\overline{u'^2}}}{v_h} \tag{3.5}$$

$$T_v = \frac{\sqrt{\overline{v'^2}}}{v_h} \tag{3.6}$$

$$k = 0.5(\overline{u'^2} + \overline{v'^2}) \tag{3.7}$$

respectively.

The results for the turbulence intensities in ROI 1 are shown in Figs. 3.26, 3.27, and 3.28. The dark regions just below $z/R = 1.0$ in these and the following plots are masked regions that are an artifact of laser light reflections from the rotor blades and should be ignored. The high-intensity regions just below the masked region near the root of the blade that are seen only in the dual-phase flow results are also erroneous and are caused by reflections.

As previously discussed, the flow at the ground below the rotor was dominated by the concentrated vorticity contained in the blade tip vortices, which produced significant local velocity fluctuations and induced secondary vorticity at the ground. Increased turbulence intensities in the near-wall region were mainly a result of the action of the vortices. Notice that all turbulence quantities are higher near

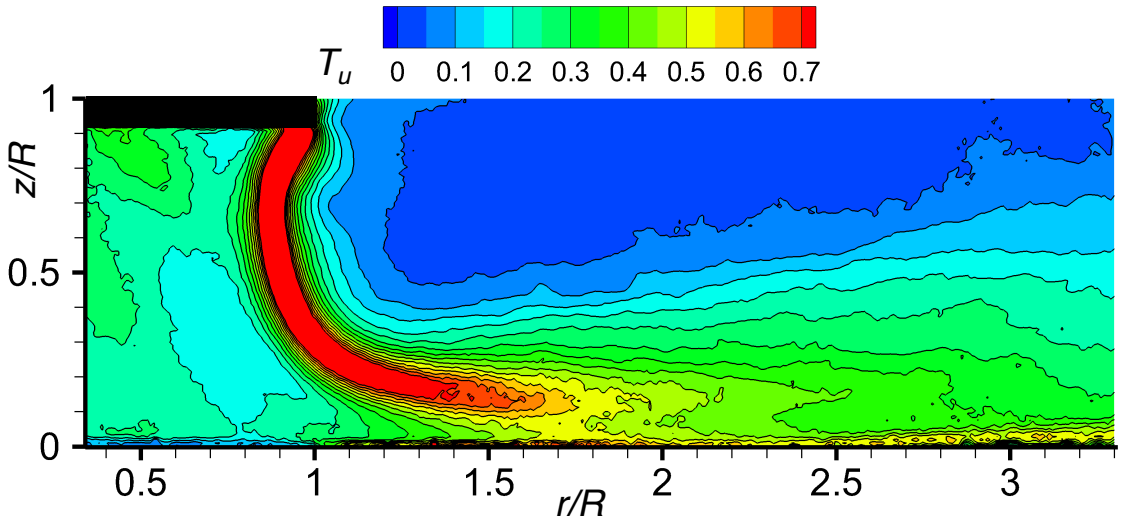

(a) Single-phase flow

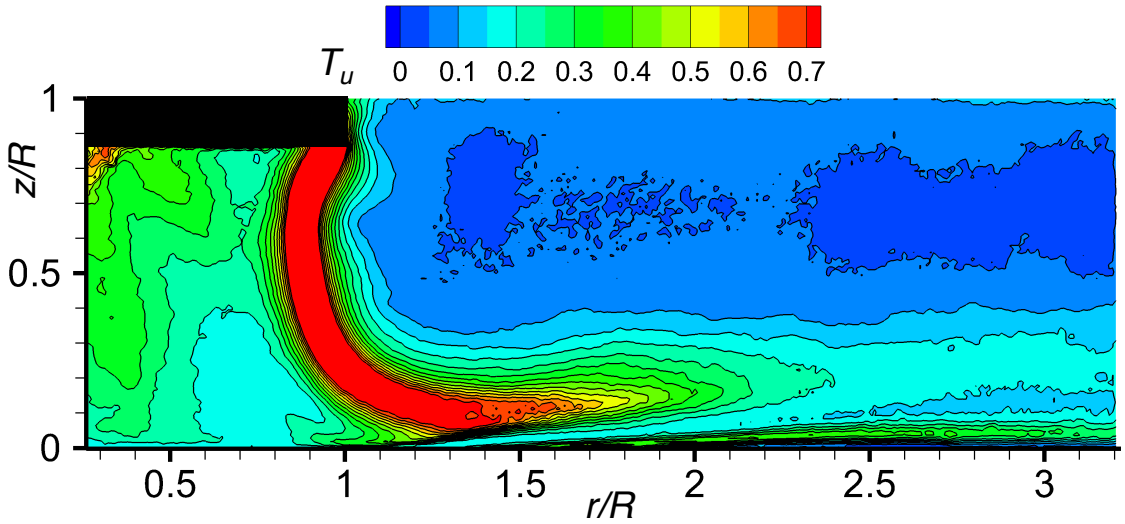

(b) Carrier of the dual-phase flow

Figure 3.26: Streamwise turbulence intensity, $T_u = \sqrt{\overline{u'^2}}/v_h$, for the single-phase and dual-phase flows in ROI 1.

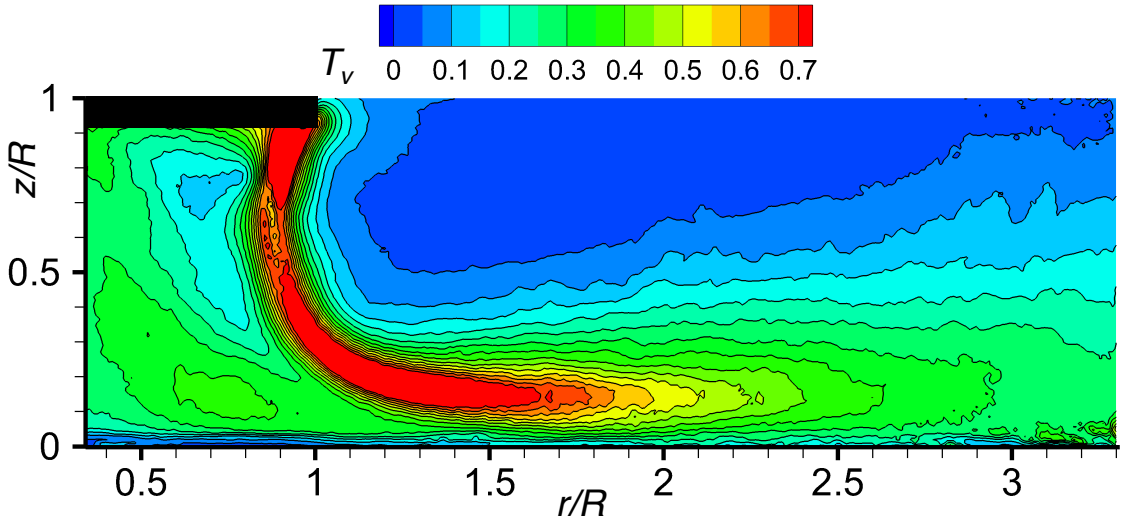

(a) Single-phase flow

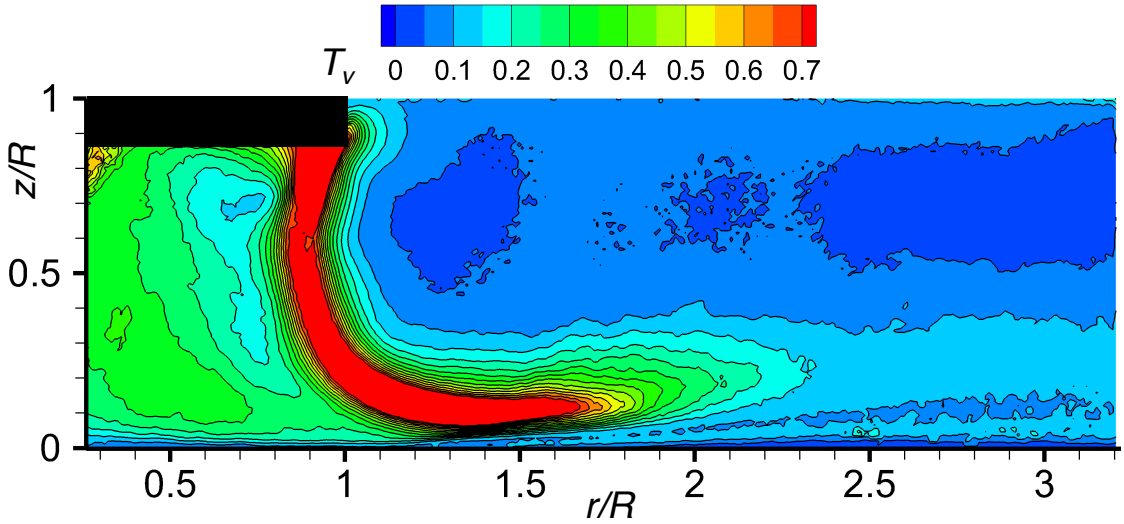

(b) Carrier of the dual-phase flow

Figure 3.27: Wall-normal turbulence intensity, $T_v = \sqrt{\overline{v'^2}}/v_h$, for the single-phase and dual-phase flows in ROI 1.

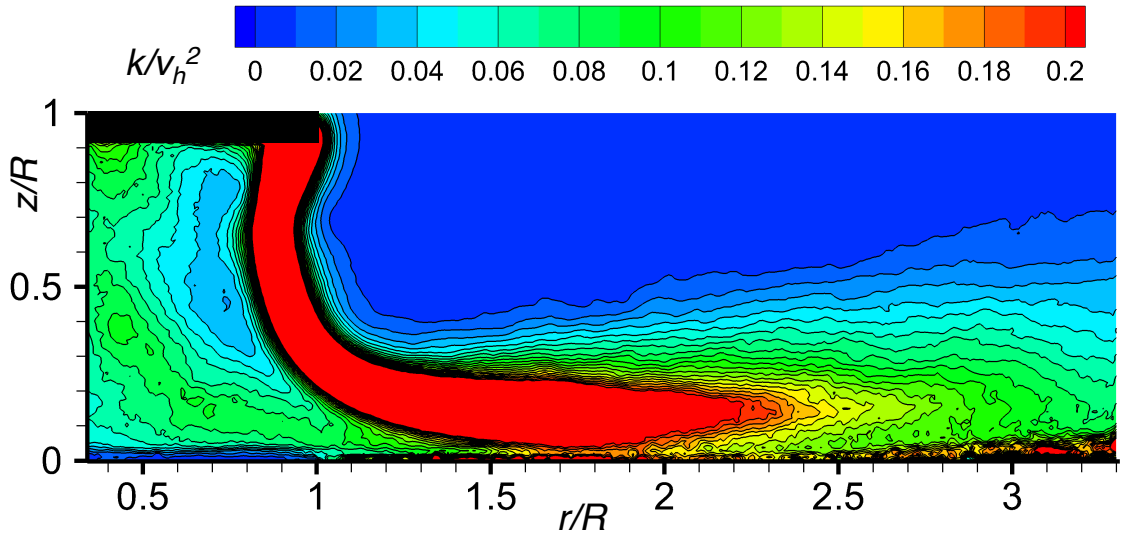

(a) Single-phase flow

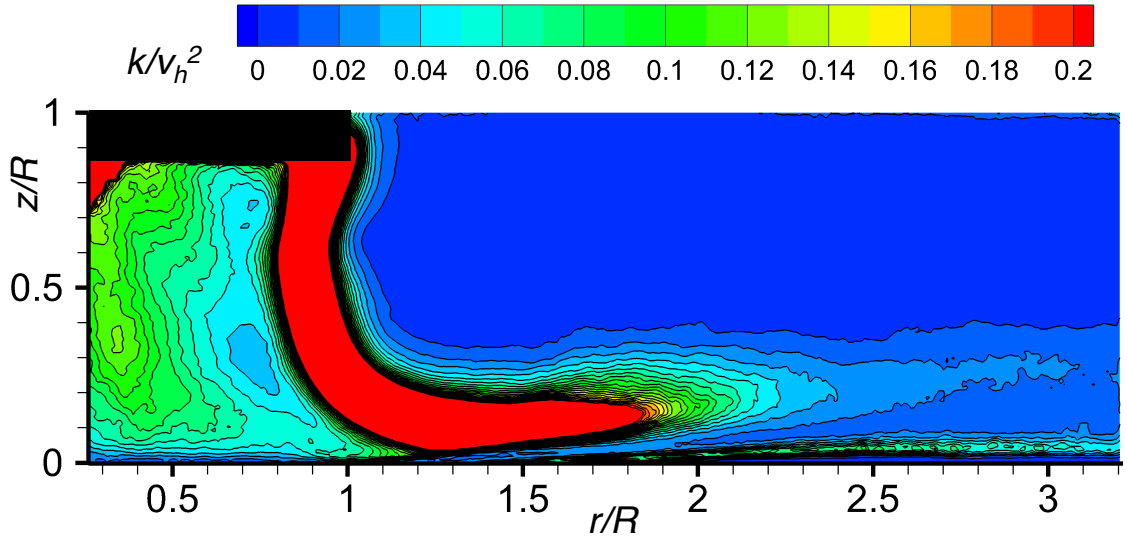

(b) Carrier of the dual-phase flow

Figure 3.28: Turbulent kinetic energy, $k = 0.5(\overline{u'^2} + \overline{v'^2})$, normalized by theoretical hover induced velocity, v_h, in ROI 1.

the slipstream boundary of the rotor wake, which is from the effects of the strong shearing between the accelerated flow inside the rotor wake and the more quiescent flow outside the wake. The convecting tip vortices also follow this shear layer (at the slipstream boundary), introducing additional turbulent stresses there. These general observations did not change when the dispersed phase was added, however the turbulence characteristics were found to be notably modified.

Figure 3.23 showed that the particles distorted and diffused the tip vortices and smaller vortical structures, which resulted in the break-up of the vortices downstream of $r/R \approx 1.8$ where most of the particles were suspended; see Fig. 3.21. This behavior was also reflected in the values of the global turbulence quantities. For $r/R > 1.8$, the carrier-phase turbulence intensities, T_u and T_v, showed significantly lower levels in the dual-phase flow compared to what was measured in the single-phase flow; see Figs. 3.26 and 3.27.

Turbulent flows comprise eddies covering a wide spectrum of sizes and energy. In a natural turbulent flow, there is a cascading process of energy transfer from the larger eddies to the smaller ones, and energy is finally dissipated at the so-called Kolmogorov scale by the action of viscosity. Therefore, large-scale vortex structures carry the preponderance of turbulent kinetic energy, much more so than the more frequent smaller vortical structures or eddies [118]. As a consequence of the particle-enhanced vortex break-up and diffusion process, the turbulent kinetic energy also decreased significantly downstream of $r/R = 1.8$; see Fig. 3.28.

The diffusion of any remaining concentrated vorticity occurred mostly downstream of $r/R = 2.0$ in the dual-phase measurements where remaining (lower) levels

of vorticity were not associated with the coherent vortices; see Fig. 3.23. In the single-phase flow, however, the vortex structures remained coherent to greater downstream distances; see Fig. 3.22. Therefore, the turbulence intensities in the streamwise and wall-normal directions (Figs. 3.26 and 3.27, respectively), as well as the turbulent kinetic energy (Fig. 3.28), decayed more slowly downstream of $r/R = 1.8$ in this case.

Comparing the detailed vorticity distributions shown in Figs. 3.24 and 3.25 to the turbulence intensities T_u in the same region (Figs. 3.29 and 3.30) further confirmed that the addition of the dispersed phase suppressed the turbulence by means of two mechanisms. First, the particles themselves decreased the local turbulence in the carrier phase; see the stream of particles near the bed in the region $r/R = 1.2$–1.6. In prior work this behavior has been attributed to the particle inertia in the resulting fluid flow [87]. Second, the particles acted to diffuse the concentrated vorticity in the flow, which was initiated downstream of $r/R \approx 1.4$, as discussed previously in Section 3.3.2.

Further insight into how the diffusion of the vortices reduced the overall turbulence in the flow is shown in Fig. 3.30, where the instantaneous flow vectors are plotted on a background contour of the mean turbulence intensity, T_u. The wake age, ζ, of a tip vortex is the time (in degrees of rotor rotation) that has passed between the current realization and the point in time the vortex was formed at the blade; also see Section 2.3.4. In this realization, the younger tip vortex at radial position A was 540° old, while the older vortex further downstream at position B was 720° old.

The radially less organized velocity vectors around the vortex core of older wake

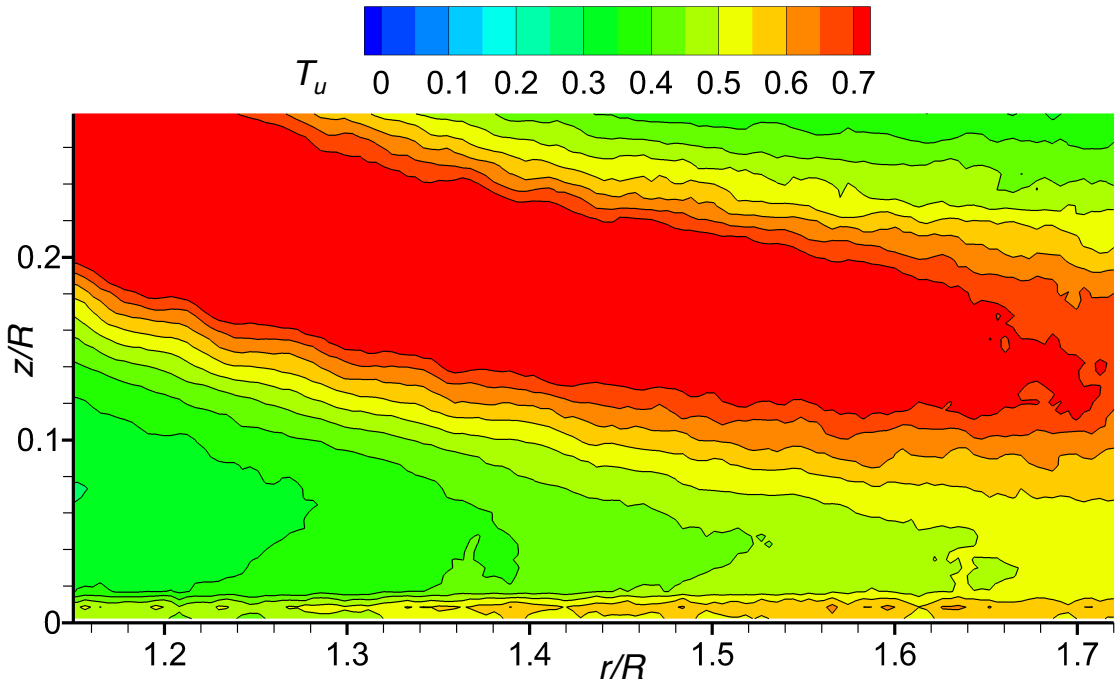

Figure 3.29: Mean streamwise turbulence intensity, T_u, for the single-phase flow within ROI 2.

age (position B, $\zeta = 720°$) indicated the loss of coherence in the vortex structure, which also coincided with a steep decrease in the streamwise turbulence intensity. The same instantaneous flow realization was shown previously in Fig. 3.24, but with the vorticity being shown in this case. This realization depicted the process of vortex diffusion by indicating a more complex, smaller-scale vorticity distribution around the older vortex core ($\zeta = 720°$, at $r/R = 1.62$), while the younger, more coherent vortex ($\zeta = 540°$, further upstream at $r/R = 1.24$ in this instance) showed more highly concentrated levels of vorticity.

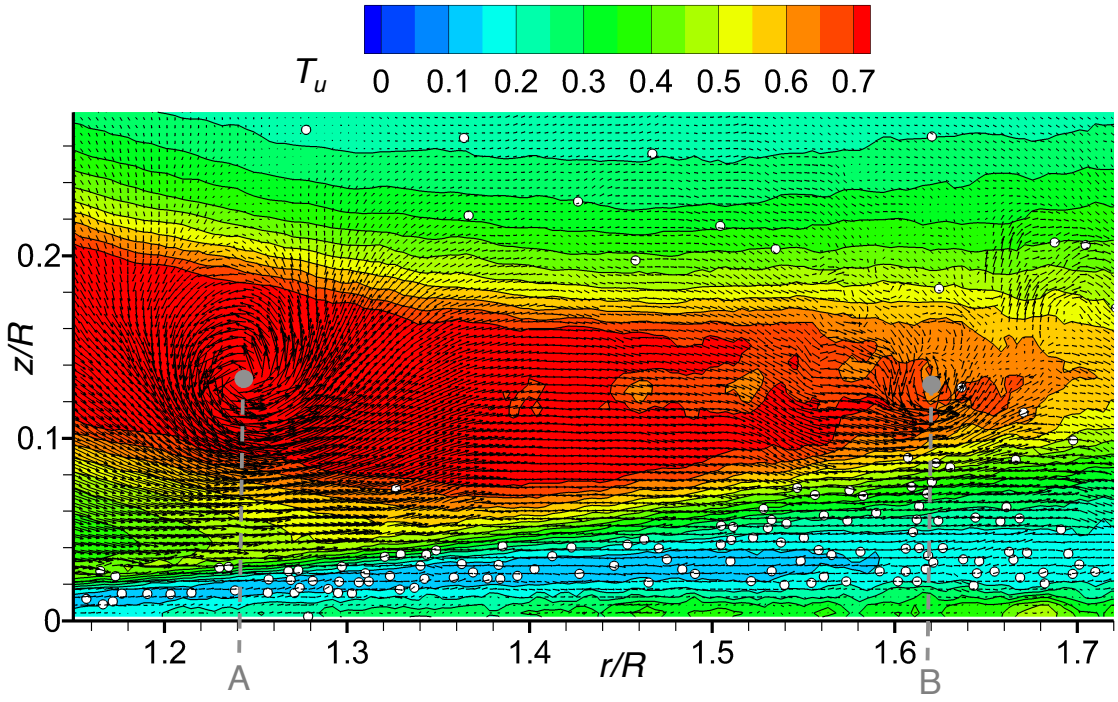

Figure 3.30: Instantaneous flow realization on a background contour of the carrier mean streamwise turbulence intensity, T_u, for the dual-phase flow within ROI 2.

3.3.4 Turbulence Production

The turbulent kinetic energy equation for a two-dimensional turbulent flow can be written as

$$\underbrace{\frac{Dk}{Dt}}_{\text{Advection}} \underbrace{-\overline{u'v'}\left(\frac{\partial \overline{u}}{\partial z}\right)}_{\text{Production}} + \underbrace{\frac{\partial}{\partial z}\left(\frac{\overline{pv}}{\rho} + \overline{kv}\right)}_{\text{Diffusion}} + \underbrace{\epsilon}_{\text{Dissipation}} = 0 \tag{3.8}$$

From Eq. 3.8, the term describing turbulence production is $-\overline{u'v'}\,(\partial\overline{u}/\partial z)$ [118]. The corresponding measured values are shown in Figs. 3.31(a) and (b) for the single-phase and dual-phase flows, respectively. The large region of intense turbulence production

that is shown corresponds to the location of the shear layer between the accelerated flow near the wall and the more quiescent flow outside the rotor wake boundary. Also, as previously described, the tip vortices convected downstream along this shear layer, producing additional turbulence here.

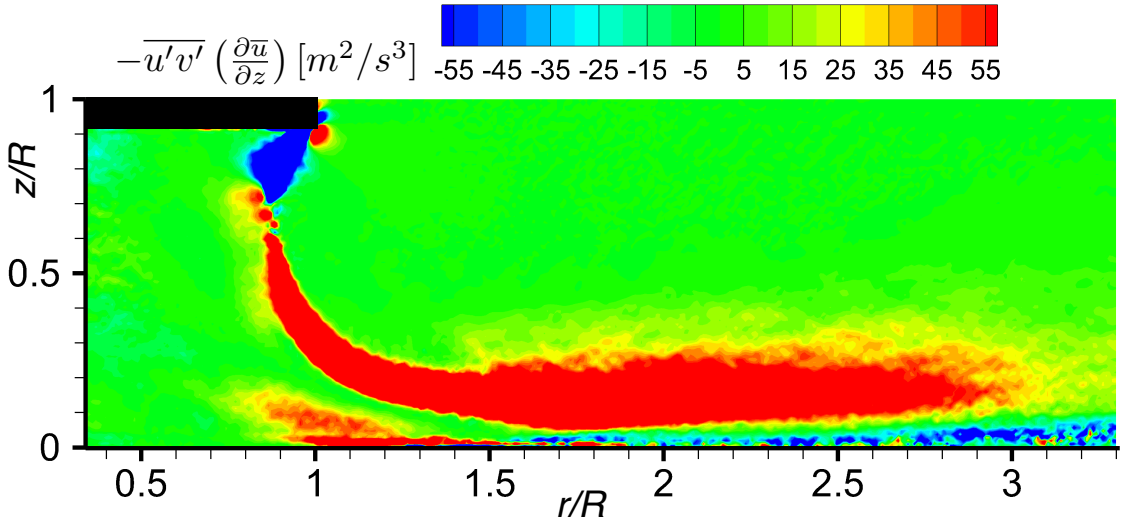

(a) Single-phase flow

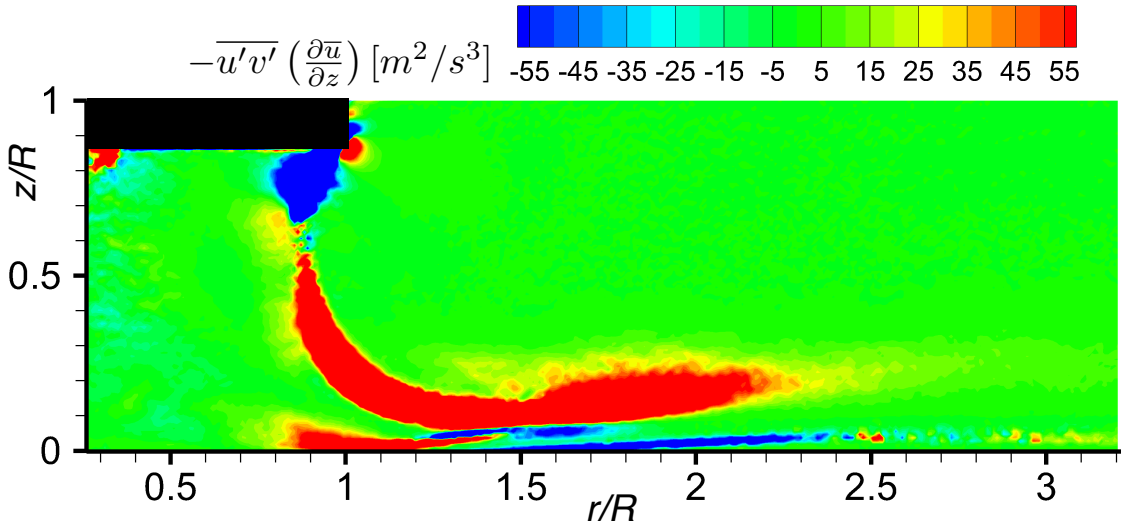

(b) Carrier of the dual-phase flow

Figure 3.31: Turbulence production measured in the single-phase and dual-phase flows in ROI 1.

Turbulence production by the action of the tip vortices was found to extend to greater radial distances from the rotor in the single-phase flow. For the dual-phase flow, the turbulence production decreased quickly in the slipstream boundary between $2.2R$ and $2.3R$. Downstream of this region, the turbulence production was seen to decrease even further, to the point where its values within the rotor wake were of the same order as those seen in the quiescent flow above the wake boundary, i.e., downstream of $r/R = 2.7$. These results suggested that the more rapid diffusion of the tip vortices in the dual-phase flow (discussed in Section 3.3.2; see e.g., Figs. 3.22 and 3.23) limited their ability to produce turbulence and, consequently, the overall levels of turbulence in the flow were decreased. This is an important finding because current models describing the rotor-generated vortex flow do not account for this effect and hence they might need to be revisited.

Figure 3.31(b) shows that negative values of turbulence were produced between $1.3R$ and $1.7R$. However, it became apparent that the negative production (or suppression) of turbulence in this region was not caused by the action of the particles, but by the negative vorticity that was induced at the ground, which was soon entrained into the tip vortices. This behavior can be seen from more detailed comparisons of the turbulence production (Fig. 3.32) to the mean vorticity distribution (Fig. 3.33) in ROI 2. In both cases, the carrier-phase flow quantities are shown together with a representative instantaneous particle distribution in this region. The mean vorticity in this case was calculated by using a time-average over 1,000 contiguous vector fields.

The instantaneous particle distribution shown in Fig. 3.32 and the time-averaged

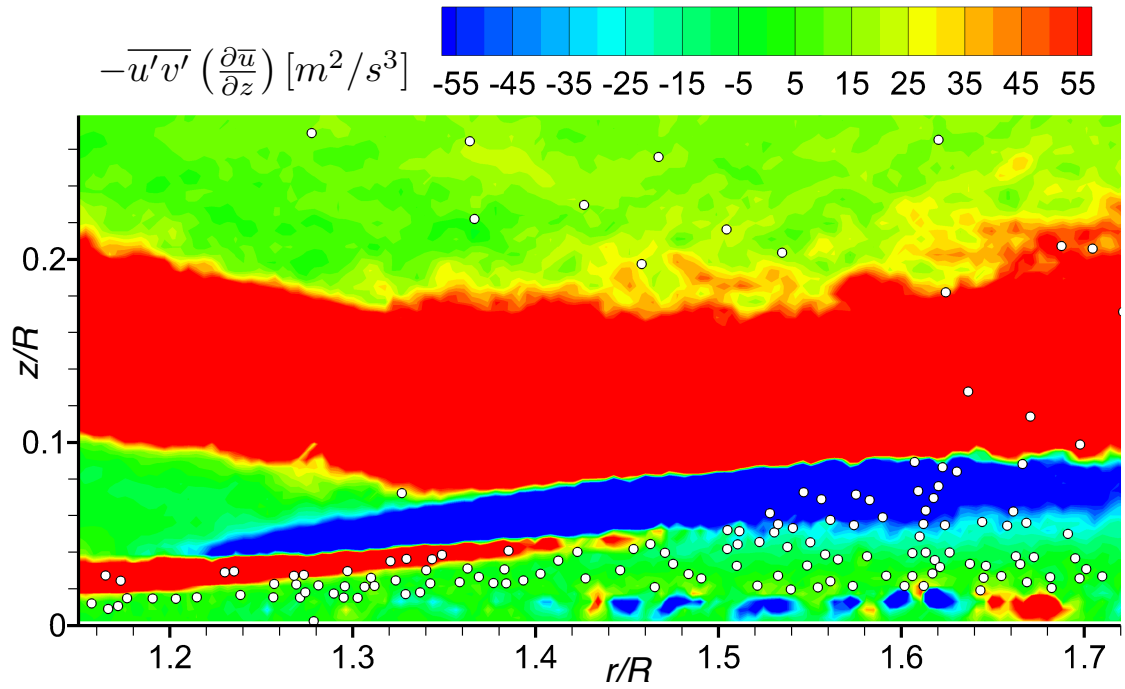

Figure 3.32: Turbulence production overlaid with an instantaneous particle distribution for a detailed dual-phase flow region at the ground in ROI 2.

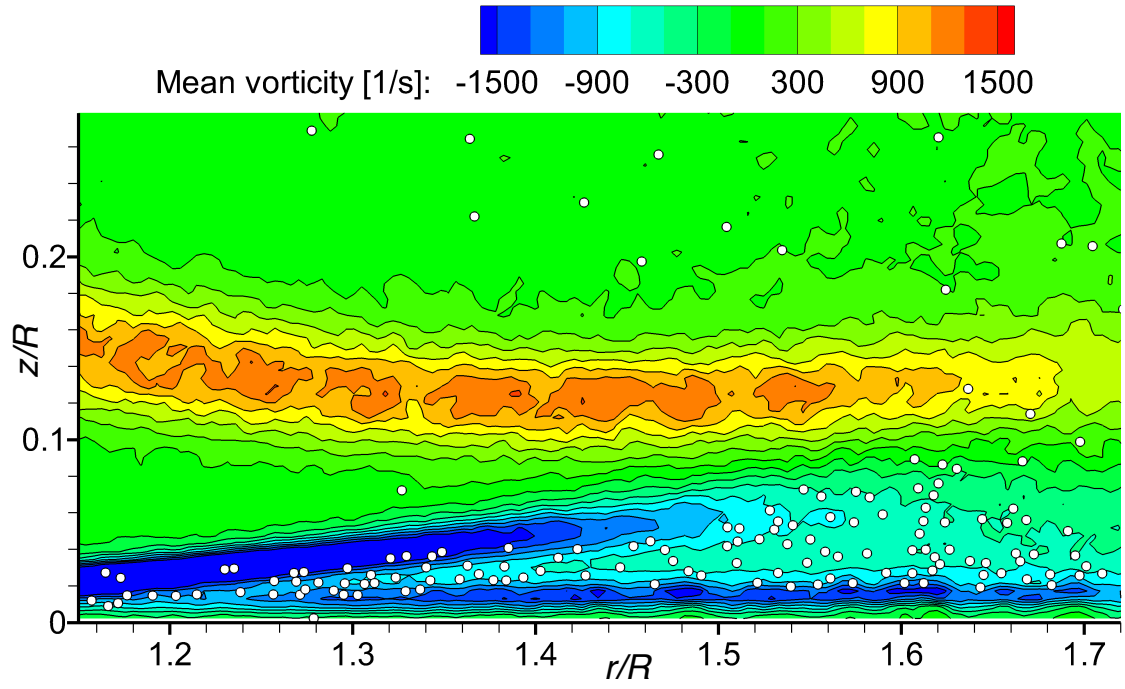

Figure 3.33: Mean vorticity distribution overlaid with an instantaneous particle distribution for a detailed dual-phase flow region at the ground in ROI 2.

particle concentration (shown previously in Fig. 3.21) indicated that the region of negative production was located mostly above the region of preferred particle flow. However, the negative mean vorticity contours shown in Fig. 3.33 more closely followed the intense regions of turbulence production; see Fig. 3.32. These results suggested that it was not the particles themselves that were the source of negative turbulence production in the carrier-phase flow.

Negative vorticity was also produced in the single-phase flow in regions near the ground. However, in the single-phase flow, this negative vorticity was mostly not convected away from the ground and, therefore, this vorticity was not entrained in the main flow; see Fig. 3.22. Hence, there is no negative turbulence production in the region between $1.3R$ and $1.7R$ in Fig. 3.31(a), while it is seen in Fig. 3.31(b).

The change in the sign of the turbulence production between $1.2R$ and $1.4R$ resulted from the variation in the turbulent Reynolds shear stresses, $\overline{u'v'}$, from negative Reynolds shear stress closer to the bed to positive values further away from the bed, while the viscous shear, $(\partial\overline{u}/\partial z)$, remained positive. The turbulence production term in Eq. 3.8 is $-\overline{u'v'}\,(\partial\overline{u}/\partial z)$, and the mean vorticity (the out-of-plane vorticity component in this two-dimensional case) is $(\partial\overline{v}/\partial x) - (\partial\overline{u}/\partial z)$.

For positive Reynolds shear stress, $\overline{u'v'}$, the values of the turbulence production will be negative for regions in which the measured mean vorticity is negative. This outcome (as shown in Figs. 3.32 and 3.33) is because the mean vorticity and the turbulence production are linked by the viscous shear stress, or synonymously, by the mean velocity gradient in wall-normal direction, $(\partial\overline{u}/\partial z)$, which is the dominant gradient that determines the vorticity near the wall and which remained positive. For

these reasons, it can be deduced that the negative vorticity (which became entrained into the tip vortices) is the source of negative turbulence production, acting to further diffuse the coherent vortex structures, thereby contributing to an overall reduction of the turbulence levels further downstream in the flow. As a consequence of the diffused vortex structures and the reduced turbulence levels, the flow may not be able to mobilize and uplift the same quantity of particles, as discussed previously in Section 3.2.

3.3.5 Anisotropy of Turbulence

Many flow simulations rely on a Reynolds-averaged approach to turbulence modeling, and the present observations have led to some interesting questions about the assumptions used in such flow models. A common method of modeling turbulence employs the Boussinesq hypothesis [118]. The so-called eddy-viscosity models are computationally inexpensive and, therefore, most widely used. Exemplars in this class of turbulence models are the $k-\epsilon$ models and the $k-\omega$ models [118]. However, the major disadvantage of the underlying Boussinesq hypothesis is the assumption that the computed eddy viscosity is an isotropic scalar quantity, which is not strictly true [95, 96, 118]. In fact, highly swirling flows (e.g., vortex flows), near-wall flows, and stress-driven flows are all known to have relatively high levels of anisotropy when turbulence is produced.

In the present results, the levels of the anisotropy of turbulence, i.e., the term

$|\sqrt{\overline{u'^2}} - \sqrt{\overline{v'^2}}|/v_h$, were calculated from the measured velocity fields for the single-phase and dual-phase flows; see Figs. 3.34(a) and (b), respectively. Figure 3.34(b) shows that the anisotropy of turbulence increased between $r/R = 1.1$–1.5 by the negative vorticity that was picked up from the ground; see Fig. 3.33. This vorticity was induced by the tip vortices and also partially originated from the eddies contained in the turbulent vortex sheet, as previously discussed in Section 3.3.2.

The region of maximum anisotropy seen in the turbulence field was located along the rotor slipstream boundary; see Fig. 3.34. As discussed in Section 3.3.3, the powerful tip vortices convected along this shear layer thereby producing additional turbulence in the flow; see Fig. 3.31. It is also known that vortices and shearing flows, in general, can cause the anisotropic production of turbulence [118]. From the results shown in Figs. 3.31 and 3.34, it can be concluded that indeed the tip vortices were a significant source of anisotropic turbulence in the flow below the rotor.

In the single-phase flow, the tip vortices persisted to relatively old wake ages corresponding to radial distances of $r/R \approx 2.0$ and more, mainly by virtue of vortex stretching [25, 44]. The anisotropy in the shear layer decreased abruptly near this radial location ($r/R \approx 2.0$) because the tip vortices were also the primary source of turbulence anisotropy in both flows. In the dual-phase flow, however, the vortices were less coherent further upstream. Consequently, the quicker diffusion of the vortices further upstream also resulted in a reduction of the anisotropy of turbulence further upstream, i.e., for $r/R \approx 1.7$. However, after the turbulence produced by the tip vortices had sufficiently decayed, the anisotropy was found to increase downstream

of $r/R = 1.9$. This particular effect was caused by the particles themselves because this region contained a relatively large quantity of suspended particles, as shown in Fig. 3.21.

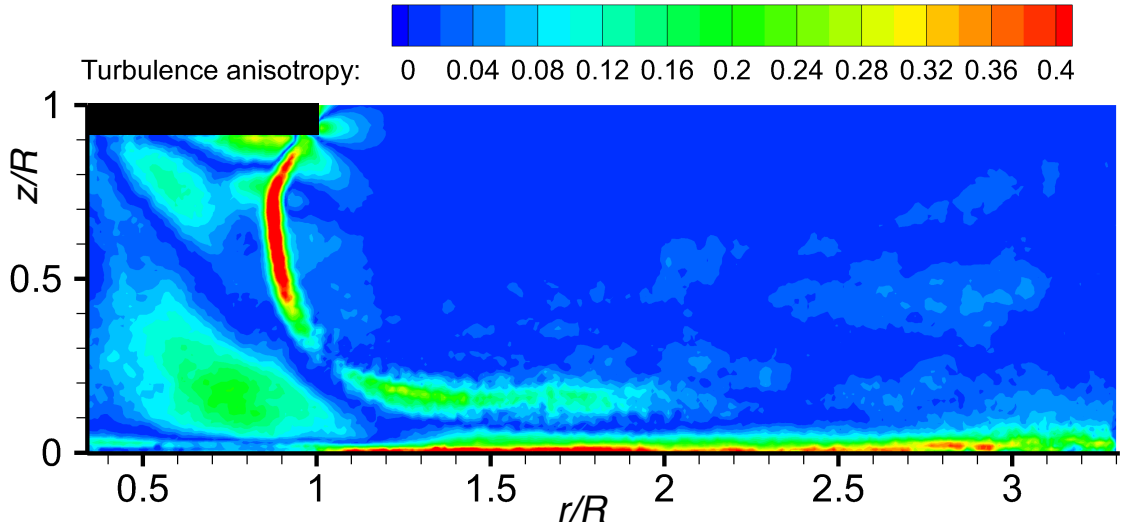

(a) Single-phase flow

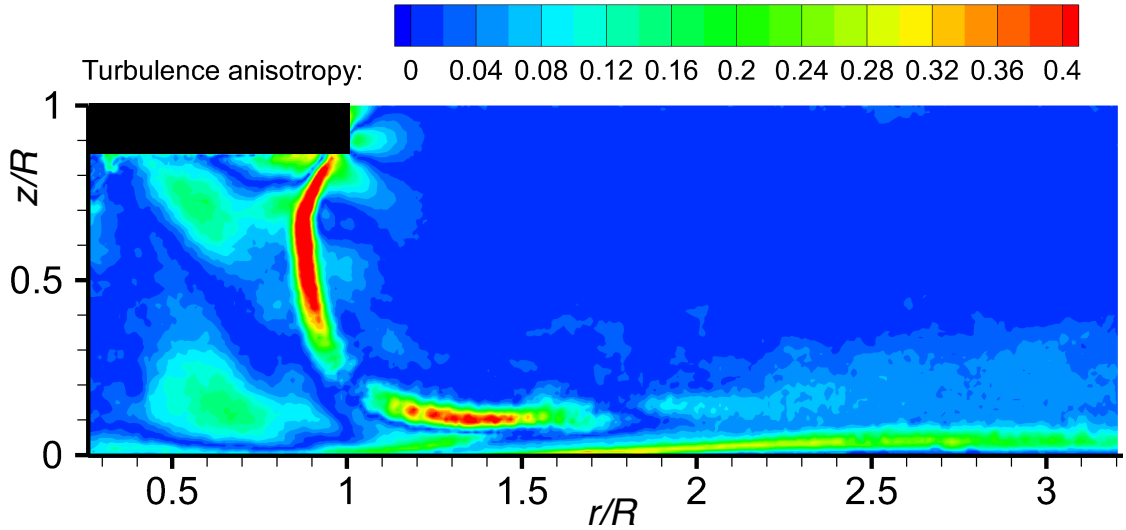

(b) Carrier of the dual-phase flow

Figure 3.34: Turbulence anisotropy normalized by theoretical hover induced velocity, $|\sqrt{\overline{u'^2}} - \sqrt{\overline{v'^2}}|/v_h$.

3.3.6 Comparison to Previous Work

The modifications of the turbulence characteristics and the anisotropy of turbulence that were found for the rotor flow have also been observed in recent measurements performed with grid turbulence and channel flows [69, 95]. Poelma et al. [69] found that a high particle volume fraction leads to significant coupling of the flow phases, also increasing the levels of anisotropy in the turbulence field. However, this behavior was found only for regions far downstream of the grid, where the larger-scale grid-generated turbulence had decayed sufficiently. Similarly, Gualtieri [95] found that in a channel flow there was an overall suppression of turbulence by the action of the particles on the larger-scale flow structures, while turbulence augmentation, including an increase in its anisotropy, was observed only in the smaller-scale range after the coherent vortices had become sufficiently diffused.

The present measurements are for a problem that is substantially different to other dual-phase flow experiments that have been previously conducted and reported in the literature. However, the rotor-generated flow investigated here showed that there were some interesting similarities to other published results. For example, turbulence was found to be attenuated by the action of the dispersed phase on the larger-scale turbulent flow structures, in this case as a consequence of distortions to coherent tip vortices by the particle field. Furthermore, an augmentation in the anisotropy of turbulence by the particles was found only in regions downstream

where the vortex-generated turbulence had largely decayed and the concentration of suspended particles was sufficiently high.

3.4 Secondary Flow Structures in the Dual-Phase Flow

The results presented thus far have shown that it was the rotor-generated vortices that were mostly responsible for sediment uplift from the underlying sediment bed; see Section 3.2. It was observed that particle pickup and suspension occurred mostly in phase with the periodic passage of the tip vortices over the bed, but the role of organized near-wall turbulent motions was less clear. Therefore, a closer examination of the instantaneous dual-phase flow field at the ground below the rotor was necessary, in particular with respect to organized turbulent motions (or turbulence events) and secondary vortical structures at the ground. To this end, the time-resolved (725 frames per second) dual-phase flow measurements of the vortex flow–particle interactions (as shown in Section 3.3) were further analyzed to better understand the fluid dynamic mechanisms involved in such rotor-induced particle flows, particularly the physical flow mechanisms that were behind particle uplift and suspension.

Although the younger tip vortices at radial positions of $r/R \approx 1.2$–1.3 from the rotor shaft axis (e.g., Fig. 3.24) were convected at the same height above the sediment bed and they were of the same strength or stronger than the older vortices (because of vortex distortion and diffusion becoming more intense further downstream), they

were mostly unable to lift up particles from the bed at these upstream locations; see Figs. 3.21 and 3.35. Therefore, attention was also given to secondary flow structures and organized turbulent motions as they may contribute to the complex flow environment near the bed and to the processes of sediment mobilization and uplift. For this analysis, the dual-phase measurements done in ROI 2 (Fig. 2.11) were used because of the finer spatial resolution that could be obtained in this region; see Section 2.4.4.

3.4.1 Reynolds-Decomposed Velocity Field

Because secondary flow structures such as secondary (induced) vortices or eddies between two passes of the tip vortex are (relatively) not as strong, and because they convect essentially with the mean flow, these structures do not appear in instantaneous velocity vector maps or vorticity realizations of the flow. Also, coherent turbulent motions (or organized turbulence structures) tend to convect with the mean flow. Therefore, to visualize these turbulent motions, it is necessary to observe the flow in a moving reference frame [124]. Because the present experimental setup did not allow for the camera to move with the flow, the mean convection velocity at each spatial point was subtracted a posteriori from the instantaneous fluid velocity components measured by the PIV. This process leaves the turbulent fluctuations about the mean at each location in the flow (i.e., a Reynolds type of decomposition). 1,000 contiguous instantaneous fluid velocity vector maps were used to obtain the local time-averaged fluid velocities for the Reynolds decomposition.

A comparison between an instantaneous flow vector map and the Reynolds-decomposed equivalent for the same instance in time is shown in Fig. 3.35. The particle locations for this instance are superimposed on the vector maps. Note that only every other flow vector is shown and the particle sizes are exaggerated for clarity. The tip vortices are still coherent at this stage and they constitute by far the strongest vortical structure in this flow, their local induced velocities being much greater than the local mean flow velocities. Therefore, the tip vortices are apparent in both vector maps, i.e., both when the flow vectors are shown on basis of the instantaneous velocity components (Fig. 3.35(a)) and when shown on basis of the Reynolds-decomposed velocity fluctuations, u' and v'; see Fig. 3.35(b). However, for the reasons described previously, most of the other vortical structures and organized turbulent motions in the flow are omitted in the former representation of the flow, as shown in Fig. 3.35(a). The Reynolds-decomposed fluctuation (or perturbation) velocity gives further insight into the turbulent flow near the ground, and a secondary vortical structure becomes visible that is counter-rotating with respect to the tip vortices (vortical center at $r/R = 1.4$ and $z/R = 0.12$ in this case).

Notice that the vortex that is located further away from the rotor (viscous core at $r/R = 1.6$ in this case) lifts up a relatively large quantity of particles, whereas the younger tip vortex further upstream does not. In general, the younger vortices carried more concentrated vorticity than the vortices further downstream because they were more coherent and less diffused than the vortices that had aged more in the flow and that have undergone significant interactions with the sediment particles, as discussed previously in Section 3.3.2. This observation indicated that the tip

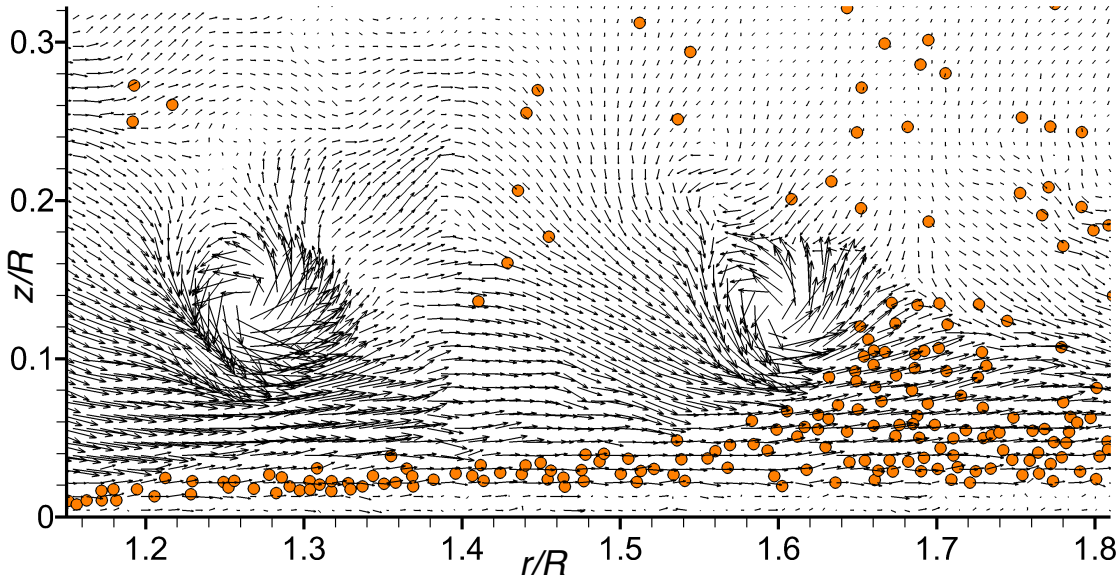

(a) Instantaneous velocity vectors

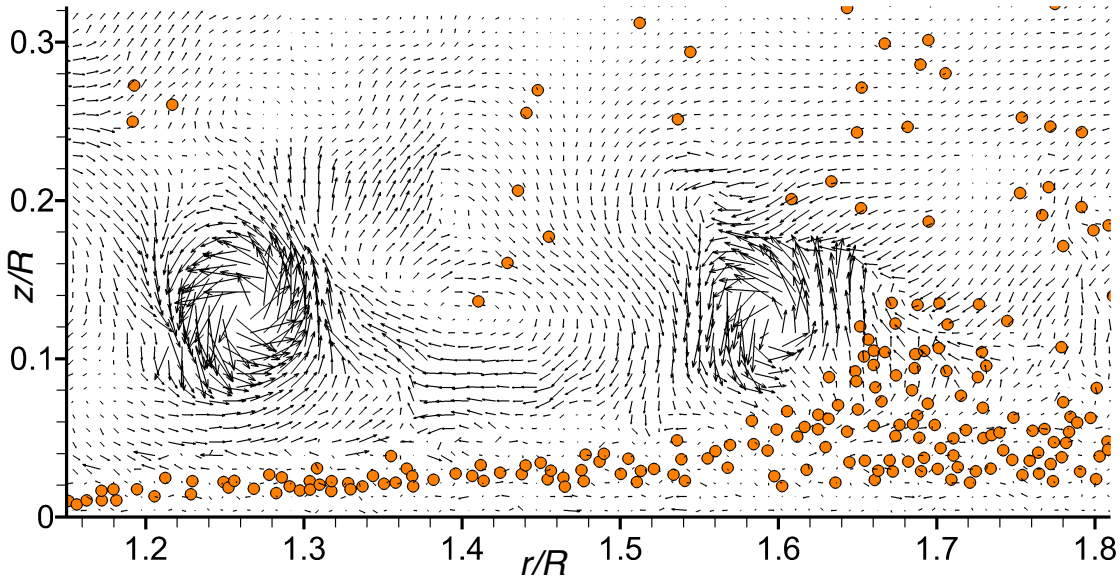

(b) Instantaneous fluctuation velocity vectors (Reynolds decomposed)

Figure 3.35: Velocity vector maps superimposed by particle locations for the same instance in ROI 2. Particle sizes exaggerated for clarity.

vortex alone was not always responsible for uplifting particles from the sediment bed, but that there were other physical mechanisms that can also contribute to the process of particle uplift.

From Fig. 3.35(b), notice the turbulent motion just downstream of the older vortex ($r/R = 1.6$–1.8) in the region where most particles are uplifted by the vortex flow. This decelerated flow region (in the streamwise direction) appears to convect particles onto the powerful tip vortex that is then able to pick up the particles and elevate them to greater heights above the bed and even into the main flow nearer to the rotor. Another interesting observation is that there was no significant difference in the (u, v) vector fields around the two vortices contained in Fig. 3.35(a), although sediment uplift occurred at the downstream location ($r/R = 1.6$–1.8) and not further upstream around the younger vortex (with its vortical center at $r/R = 1.27$ in this instance). However, local differences were observed when examining the (u', v') vector field of the turbulent fluctuations of the carrier phase for the same instance, as shown in Fig. 3.35(b).

Although the previous observations are certainly interesting and very useful, it should be pointed out that the sediment particles see the instantaneous velocity components and not only the turbulent perturbations, i.e., the mean flow components cannot be neglected in this non-uniform flow. In addition, unsteady pressure forces induced by the tip vortices may contribute to sediment uplift [65, 85]. Therefore, a Reynolds decomposition (Fig. 3.35) gives another way of looking at this flow problem, and may help to understand a possible contributor to sediment uplift and entrainment mechanisms in this flow. However, by itself, the velocity fluctuations

cannot give a holistic picture and so they cannot fully explain the particle motion.

Figures 3.36(a)–(d) show consecutive instantaneous, Reynolds-decomposed flow realizations near the ground (within ROI 2) for every 30° of wake age. Again, the wake age, ζ, of the tip vortex is the time (in degrees of rotor rotation) that has passed since the respective vortex was formed at the blade. The coherent blade tip vortices exposed a distinct quadrupole structure when the $u'v'$ correlation was plotted; see Fig. 3.36. Most tip vortices trailed a decelerated flow region (so-called "inward interaction" motion after Wallace et al. [59]), $r/R = 1.6$–1.8 in this case, that seemed to convect particles back towards the succeeding vortex, where they were subsequently picked up and elevated to greater heights off the bed. This interesting observation rises the question if this turbulent fluid motion was a precursor to particle uplift, and if it was a necessary but insufficient condition.

In a detailed case study on particle resuspension and saltation in a water channel flow, van Hout [106] observed that particle suspension occurred in case of the combined action of a strong, coherent fast-moving ($u' > 0$) flow structure upstream of the particle pickup, and a downstream ejection (i.e., a turbulent motion with $u' < 0$ and $v' > 0$). They also showed that uplifted particles were immersed in positive wall-normal velocity fluctuations, $v' > 0$. In the present work, Figs. 3.35(b) and 3.36 suggested that positive values of v' (i.e., excess velocities in the upward direction away from the bed) prevailed in the regions where most of the sediment particles were picked up and suspended by the tip vortices; statistical distributions of these fluctuation velocities are shown later. This latter observation suggested that similar uplift mechanisms were at work in this rotor-generated vortical flow near the

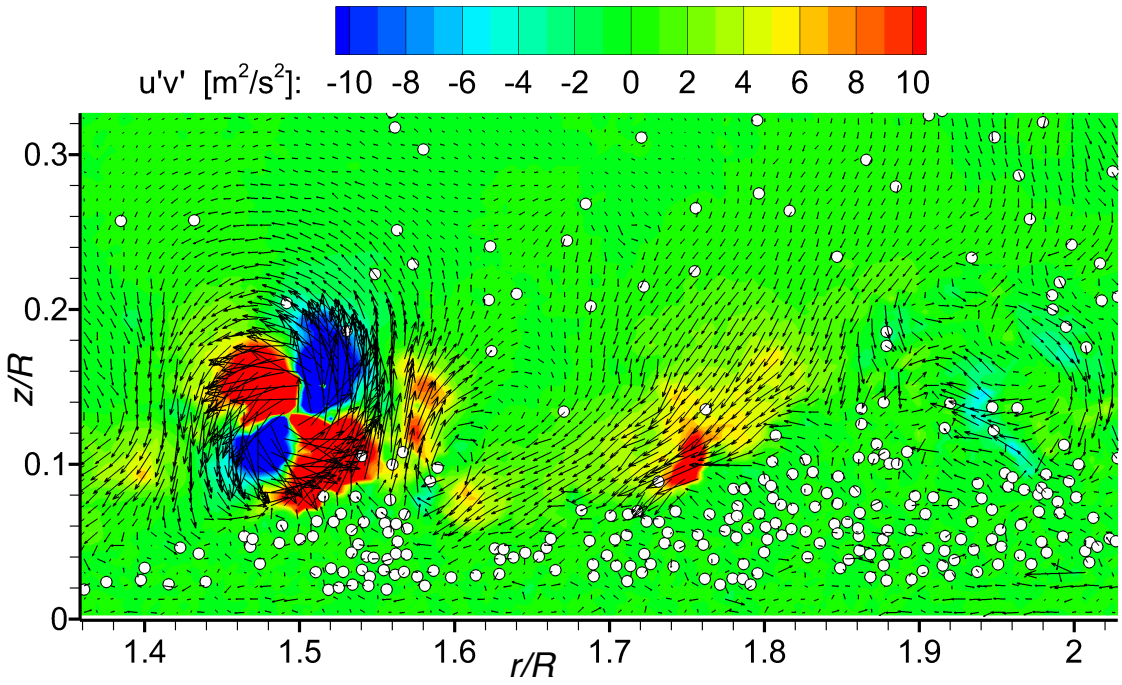

(a) $\zeta \approx 660°$

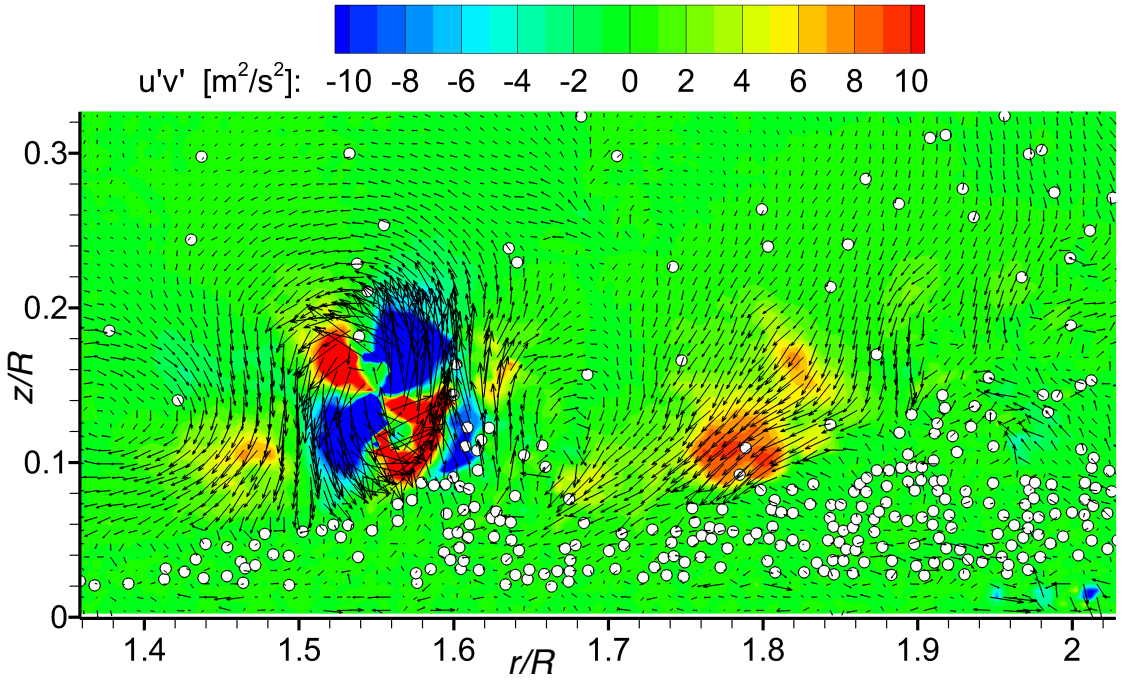

(b) $\zeta \approx 690°$

Figure 3.36: Consecutive carrier-phase velocity vector fields (Reynolds decomposed) superimposed by the particle distribution on a background contour showing the instantaneous $u'v'$ correlation in ROI 2. Only every other measured velocity vector is shown.

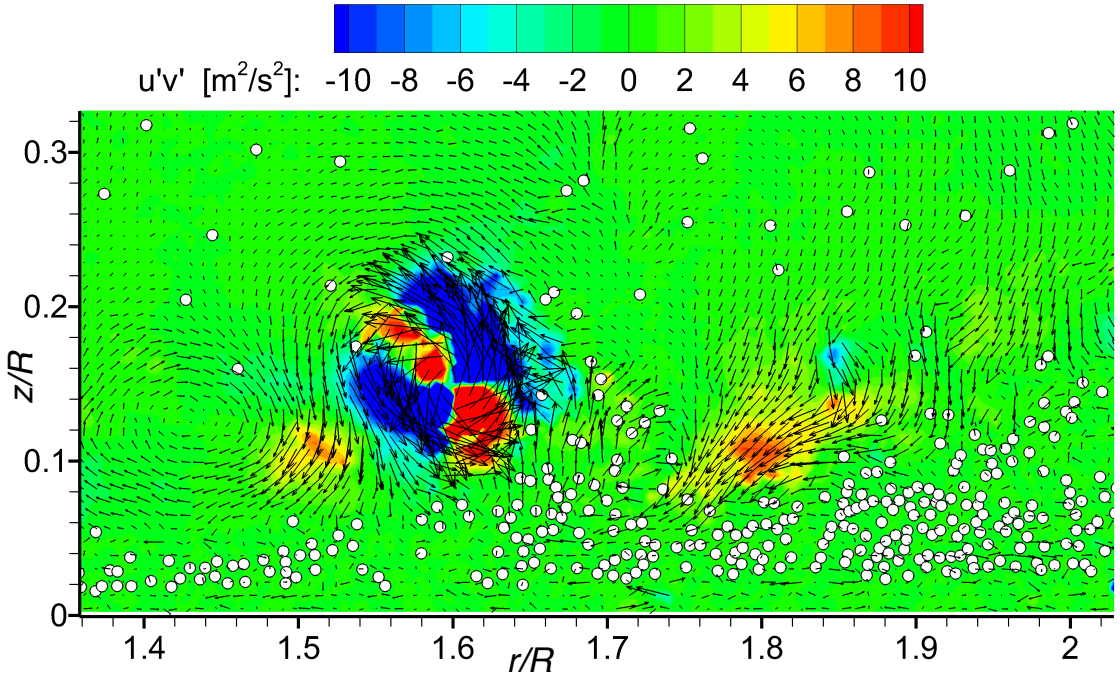

(c) $\zeta \approx 720°$

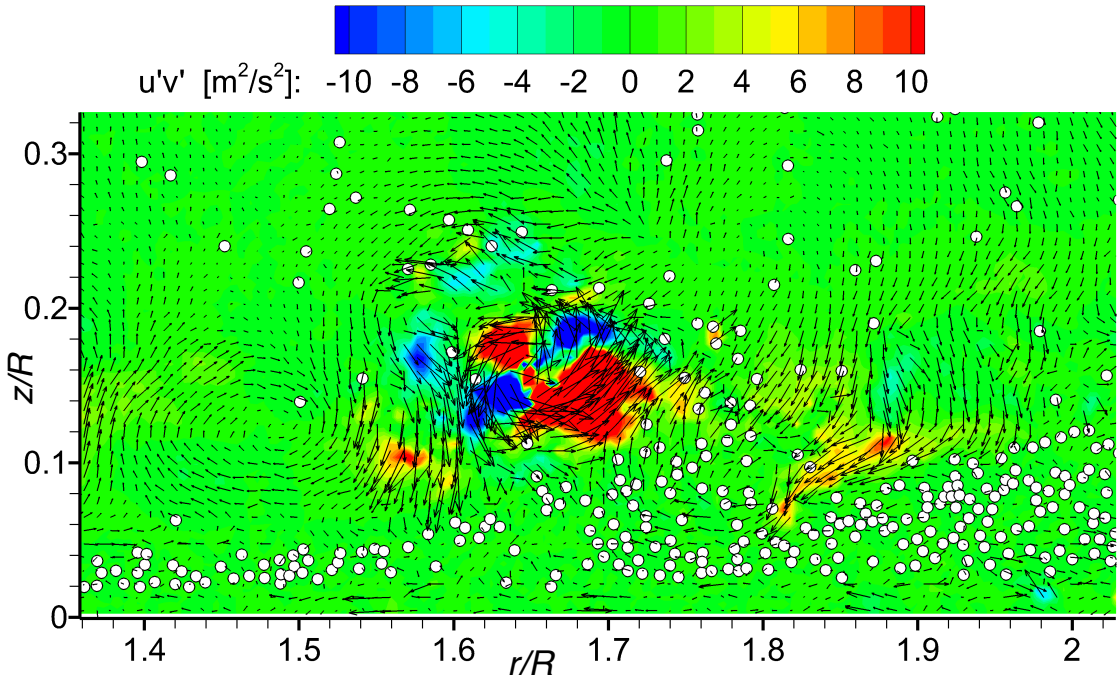

(d) $\zeta \approx 750°$

Figure 3.36: Consecutive carrier-phase velocity vector fields (Reynolds decomposed) superimposed by the particle distribution on a background contour showing the instantaneous $u'v'$ correlation in ROI 2. Only every other measured velocity vector is shown.

sediment bed when compared to the channel flow investigated by van Hout [106]. The downstream ejection motion contributing to particle uplift was mostly caused by a clockwise-rotating secondary vortical structure that was downstream of the tip vortex; see Fig. 3.37.

Another example showing the particle pickup process from the ground in ROI 2 is seen in the contiguous time-history given in Fig. 3.37. The instantaneous Reynolds-decomposed (fluctuation) velocities are shown on background contours of the out-of-plane vorticity for a sequence of flow realizations recorded every 30° of wake age. The younger tip vortex at $r/R \approx 1.4$ just entering the ROI has a coherent structure with a clearly defined vortical center containing high levels of concentrated positive vorticity; see Figs. 3.37(a) and 3.37(b). The two older vortical structures further downstream in the same realizations of the flow (at $r/R \approx 1.7$ and $r/R \approx 2.0$) exposed a much less organized structure, which was attributed to the gradual diffusion of the tip vortices as they aged in the flow and convected downstream; also see the larger field of view that was given previously in Fig. 3.23. The detailed time-history in Fig. 3.37 also provides evidence of how the younger tip vortex (wake age $\zeta = 600°$ when entering this region in Fig. 3.37(a)) became less coherent and more diffused as it aged by $\Delta\zeta = 150°$ over the flow realizations shown in Figs. 3.37(a)–(f).

It is also seen how negative vorticity from the ground was picked up by the tip vortex (between $r/R = 1.35$–1.7 in this sequence). Negative vorticity was previously shown to contribute to particle uplift from the sediment bed; see Section 3.3.2. Furthermore, when the negative vorticity was picked up from the ground by the (still

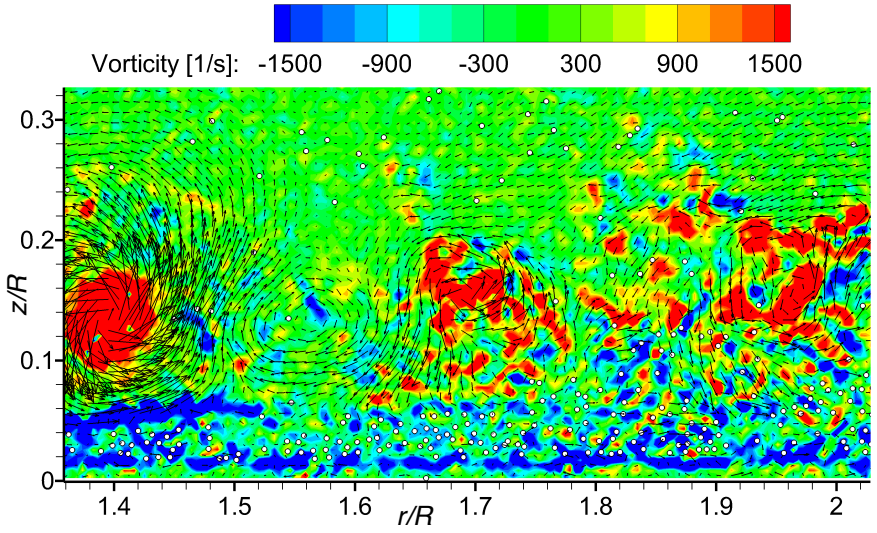

(a) Wake age of younger tip vortex $\zeta \approx 600°$

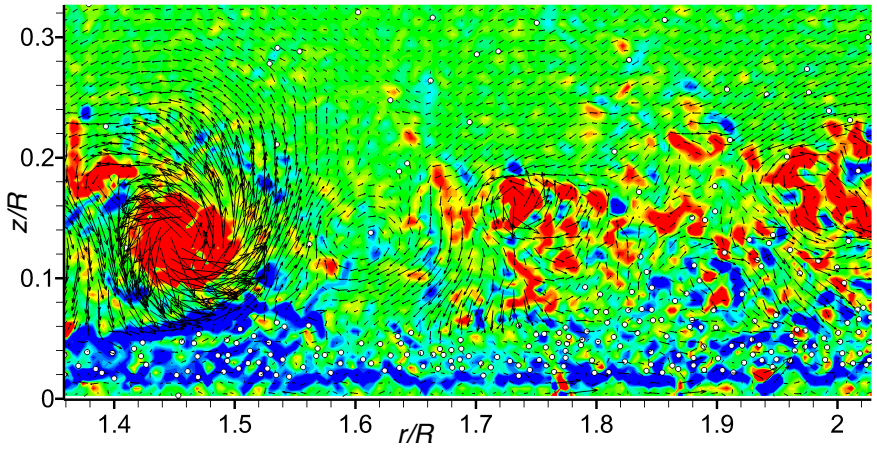

(b) Wake age of younger tip vortex $\zeta \approx 630°$

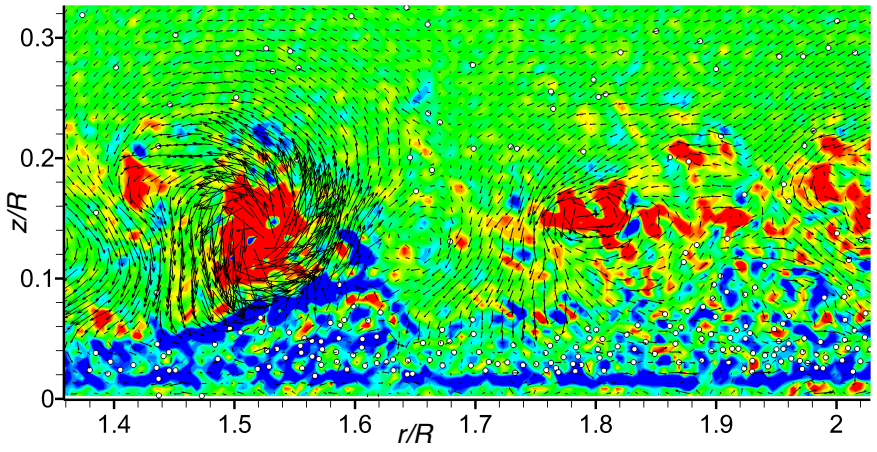

(c) Wake age of younger tip vortex $\zeta \approx 660°$

Figure 3.37: Consecutive carrier-phase velocity vector fields (Reynolds decomposed) superimposed by the particle distribution on a background contour showing the instantaneous out-of-plane vorticity in ROI 2.

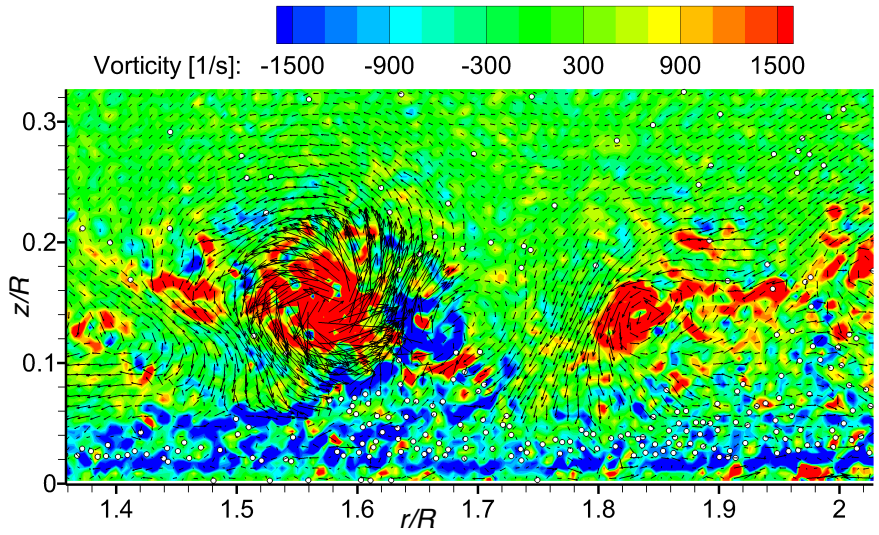

(d) Wake age of younger tip vortex $\zeta \approx 690°$

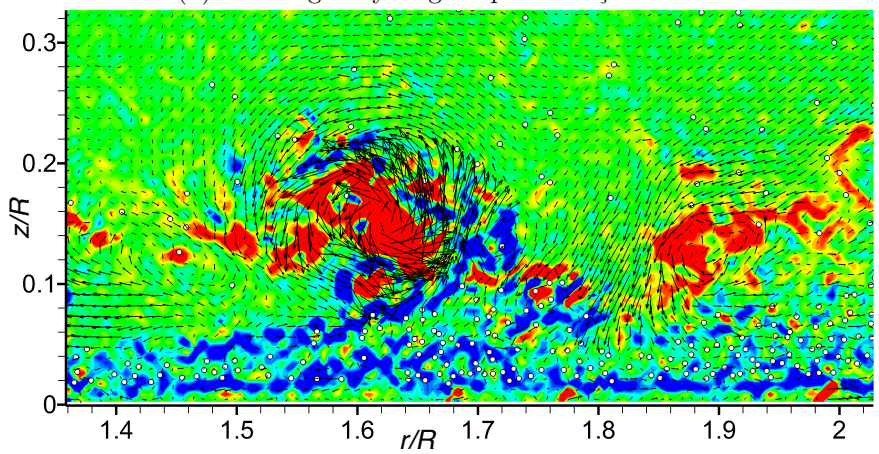

(e) Wake age of younger tip vortex $\zeta \approx 720°$

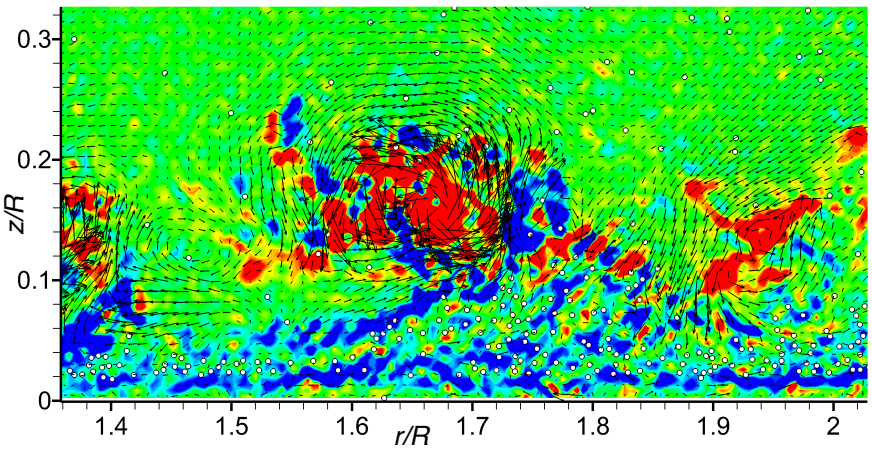

(f) Wake age of younger tip vortex $\zeta \approx 750°$

Figure 3.37: Consecutive carrier-phase velocity vector fields (Reynolds decomposed) superimposed by the particle distribution on a background contour showing the instantaneous out-of-plane vorticity in ROI 2.

at this point) coherent tip vortices, this process accelerated the diffusion of the tip vortices that contained the positive vorticity in this case, as discussed in more detail in Section 3.3.4. While the flow was clearly vortically dominated by the blade tip vortices trailing from the rotor blades, secondary vortical flows were also observed in between the passages of the tip vortices; see Fig. 3.37. With radial velocities of less than 20% of those of the tip vortices, these secondary vortices were obviously much weaker than their source.

The sequence in Figs. 3.37(b)–(e) shows a time-history of one wave of sediment pickup (or a particle burst) by the interplay of the tip vortex and the secondary vortical structure observed in between the two tip vortices in this ROI. This clockwise-rotating secondary vortical structure can, by nature of its rotational orientation, be attributed to the tip vortices, i.e., it was produced by the combined action of two successive counterclockwise-rotating tip vortices. The decelerated flow region of the secondary vortical structure (between $r/R = 1.6$–1.7 at a height of $z/R \approx 0.07$ in this case) appears to move the particles towards the succeeding tip vortex. This relatively strong vortex is then able to pick up these decelerated particles by accelerating the fluid in downstream ($u' > 0$) and upward direction (away from the bed; $v' > 0$), i.e., in the opposite direction to the previous decelerated turbulent motion downstream of the tip vortex.

It is somewhat intuitive that the dominant, counterclockwise-rotating tip vortices are more likely to pick up particles when a preceding flow structure has decelerated the particles before, just downstream of the tip vortex. A similar observation has been made [106], although for a more canonical water channel flow with

much different flow conditions than those in the vortically-dominated flow below a rotor in the present work. Whereas the previously shown results were instantaneous flow realizations, the statistical distribution of the turbulent motions are also of interest, i.e., the recurrence of turbulence events.

3.4.2 Quadrant Analysis

As previously discussed, the quadrant analysis method can be useful to examine the recurrence of turbulent flow phenomena and turbulence structures as they may contribute to sediment uplift, entrainment, and suspension mechanisms, eventually also contributing to the development of a brownout dust cloud. The quadrant analysis (after Wallace et al. [59]) was introduced and explained in Section 3.2.5. However, only one measurement height above the ground was investigated, and the focus of the previously shown investigation was more on the two-way coupling and how the $u'v'$ correlations were modified by the presence of the particles. In the present section, a more detailed examination of the statistical distribution of the turbulence events in the dual-phase flow is shown. A range of measurement heights above the ground was investigated for several downstream distances from the rotor axis, and the results were then correlated to the processes of sediment mobilization and uplift.

Wallace et al. [59] identified four kinds of turbulence events, namely sweeps, ejections, outward interactions and inward interactions. Recall that the four types

of motion are classified by the signs of the fluctuation velocities, u' and v'. The measurements are then plotted on a quadrant map, as shown in Fig. 3.16, which essentially shows the main directions of the turbulent momentum transfer relative to the bulk movement of the fluid. Scatter quadrant plots for the fluid turbulence are shown in Fig. 3.38 for several spatial measurement locations in the flow. Each data point represents a turbulence event for one location and for one point in time. The data that were obtained from a single location were then extracted from the carrier phase over time and plotted on a quadrant map.

Figures 3.38(a) and 3.38(b) show that the streamwise turbulent fluctuations prevailed very near the sediment bed, which is associated with the wall-condition that the sediment bed constitutes, thereby suppressing the wall-normal fluctuation component, v'. This outcome yielded a slightly stretched or elongated distribution of turbulence events in the quadrant map, which also means higher levels of anisotropic turbulence. Moving away from the wall (the edge of the sediment bed), the organization of the turbulence events into the quadrants shows that the vortices produced significant amounts of turbulence and also a relatively high level of anisotropy in the turbulence.

The foregoing behavior was pronounced for greater elevations above the ground, especially closer to the height where the tip vortex passed ($z/R \approx 0.15$); see Fig. 3.38(c). However, this tip-vortex-related anisotropy in the flow was of different nature than the one observed near the wall in that the wall-normal (vertical) component of the velocity fluctuation dominated over the streamwise fluctuations in the tip vortex path, while it was of relatively low magnitude closer to the wall. In

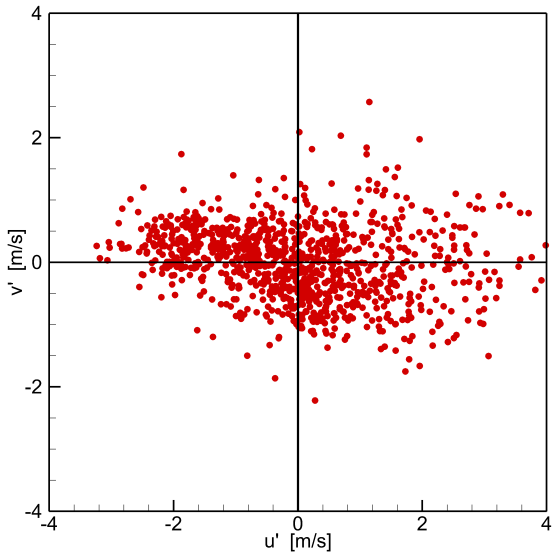

(a) $r/R = 1.2$, $z/R = 0.03$

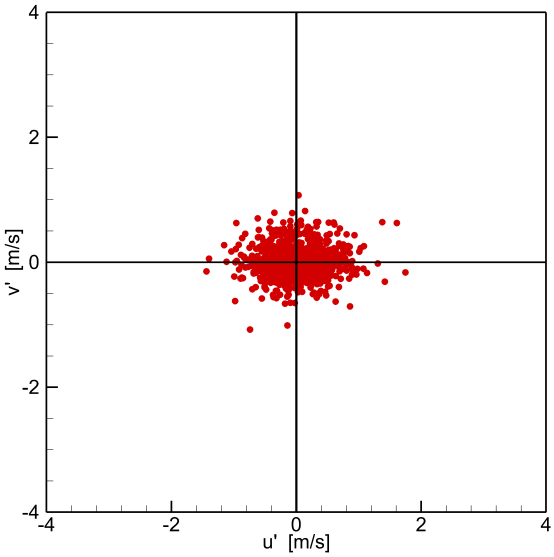

(b) $r/R = 1.5$, $z/R = 0.03$

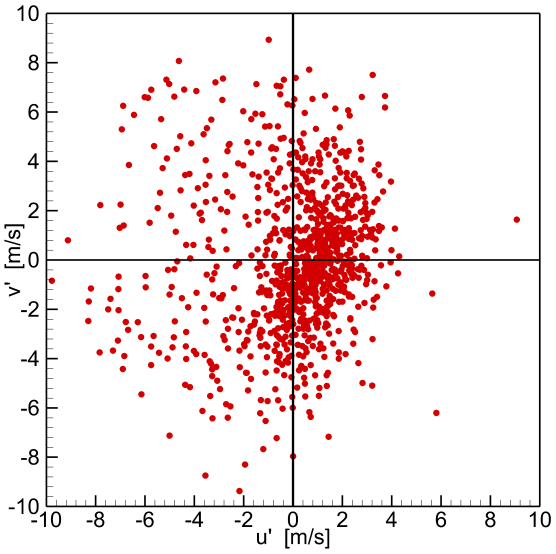

(c) $r/R = 1.5$, $z/R = 0.15$

Figure 3.38: Quadrant plots of fluid turbulence events for several spatial measurement locations in the flow.

general, the tip vortices were a primary source of anisotropy in the production of turbulence. As a consequence, the turbulence anisotropy in the slipstream boundary decreased abruptly as the tip vortices began to diffuse further downstream, an observation previously documented in Section 3.3.5.

For heights from the bed that were closer to the slipstream boundary (which also constitutes the approximate tip vortex path), the negative excess velocities discussed previously with Fig. 3.36 were apparent; see Fig. 3.38(c). Notice the much greater magnitude of the decelerated (in the streamwise direction) turbulence events ($u' < 0$; ejections and inward interactions) compared to the events with positive u' components. Also notice the greater range of the axes in Fig. 3.38(c), which was necessary to cover the whole spectrum of turbulence events at this measurement location. The radial location from which the turbulence data were extracted in this case coincided with the region where much sediment uplift from the bed was detected; see Fig. 3.21. This latter observation is interesting because it was found by van Hout [106] for a channel flow that such decelerated turbulent motion played a key role in the process of uplifting particles, particularly the ejection motion. This turbulent motion is sometimes called "Q2" motion because this turbulence event falls in the second quadrant of a quadrant map.

In the present results, the dominant streamwise turbulent fluctuations near the sediment bed were seen to correlate well with particle mobilization and sediment transport along the bed, an observation also made for aeolian and channel flows [52,62]. This latter conclusion can be drawn from a comparison of the quadrant plots near the sediment bed with the observed particle motion upstream of $r/R = 1.4$, i.e., where

barely any particles were uplifted and were merely convected radially outward along the bed in a saltation-like manner; see Figs. 3.21 and 3.35. Comparing the quadrant plot for the upstream location ($r/R = 1.2$) to the one further downstream ($r/R = 1.5$) for the same wall-normal distance ($z/R = 0.03$) shows that both components of the near-wall fluctuations were greater upstream. Of particular interest, is the fact that the upstream location shows much greater streamwise fluctuations, u', compared to the downstream location, which further confirms the previous outcome that it was the streamwise Reynolds stresses (and hence the streamwise turbulent fluctuations) that were mostly responsible for sediment mobilization on the bed; see Section 3.2.3.

Because information about a preferred statistical organization of turbulence events is of particular interest, the probability density for the turbulence events can be shown for measurement locations at several radial distances from the rotor, and for several heights above the sediment bed. The probability density distributions (or joint frequency distributions) show the frequency or likeliness with which turbulence events occur. Exemplars of such joint frequency distributions are shown in Figs. 3.39(a) and 3.39(b), which are the equivalent representations of the scatter quadrant plots shown previously in Figs. 3.38(a) and 3.38(b), respectively.

For the joint frequency distributions, the fluctuation velocities, u' and v', were normalized by the theoretical hover-induced velocity, v_h. The stretched probability density distribution (in the streamwise direction) seen in Fig. 3.39(a) shows that the streamwise components of the turbulent fluctuations prevailed in magnitude and in recurrence. Comparing Fig. 3.39(a) to Fig. 3.39(b) shows that the upstream location at $r/R = 1.2$ has greater streamwise (i.e., u') fluctuations, while all locations further

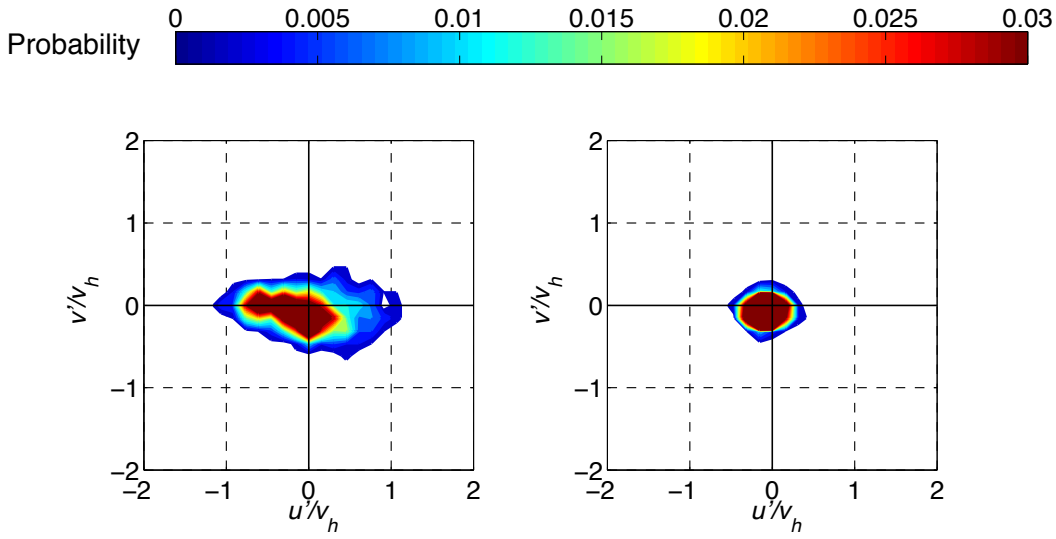

(a) $r/R = 1.2$, $z/R = 0.03$ (b) $r/R = 1.5$, $z/R = 0.03$

Figure 3.39: Joint frequency distributions of turbulence events for the carrier phase at $z/R = 0.03$ above the sediment bed.

downstream show a much more isotropic turbulence distribution; see Fig. 3.39(b). The mobilization of most of the sediment particles on the bed was also observed at these upstream locations around $r/R = 1.2$. This observation confirmed that it was primarily the streamwise velocity fluctuations and their related streamwise Reynolds stresses that were responsible for sediment mobilization on the bed; see also the discussion in Section 3.2.3. Both measurement locations showed relatively low wall-normal velocity fluctuations, v', and particles were not suspended at these upstream locations closer to the rotor (for $r/R < 1.5$; see Fig. 3.21). This outcome suggested that greater magnitude positive wall-normal velocity fluctuations ($v' > 0$; upward and away from the ground) were important for picking up and suspending the sediment particles.

The joint frequency distributions at a height of $z/R = 0.05$ above the sediment bed and for several downstream distances from the rotor are shown in Fig. 3.40.

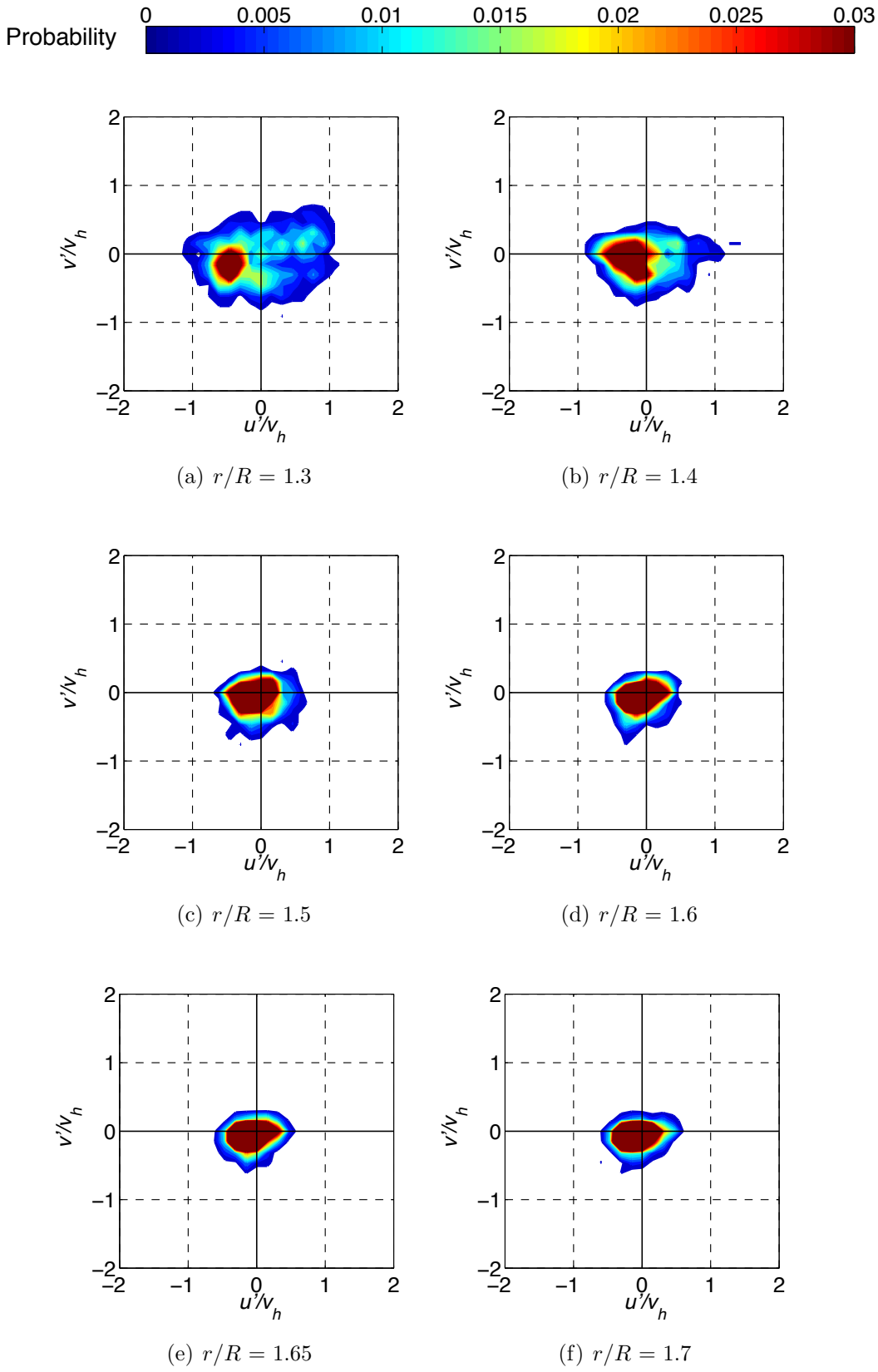

(a) $r/R = 1.3$

(b) $r/R = 1.4$

(c) $r/R = 1.5$

(d) $r/R = 1.6$

(e) $r/R = 1.65$

(f) $r/R = 1.7$

Figure 3.40: Joint frequency distributions of turbulence events for the carrier phase at $z/R = 0.05$ above the sediment bed.

For this relatively close distance to the sediment bed, prevailing decelerated fluid was found for measurement locations of $r/R < 1.5$. Such negative excess velocities were previously associated with initial particle uplift by van Hout [106], albeit for a different research problem, namely dispersed polystyrene beads in a water channel flow.

Such ejections and inward interactions contributed to the initial particle uplift from the sediment bed, which occurred mostly at $r/R \approx 1.3$–1.5 (Figs. 3.23 and 3.24), although most of the particles were not suspended in the main flow until greater downstream distances from the rotor. Positive excess velocities in upward and downstream direction ($u' > 0$; $v' > 0$) were also needed to suspend these particles. These positive velocity fluctuations were introduced by the tip vortices when they convected at greater heights above the sediment bed; see e.g., Fig. 3.36, where the flow vectors were plotted on the basis of the velocities u' and v'.

A similar outcome was observed for a height of $z/R = 0.07$ above the sediment bed, as shown in Fig. 3.41, although the fluctuation velocities were generally greater than for positions closer to the ground (Fig. 3.40). The vortices became more diffused as they aged and convected downstream in the flow; see Fig. 3.23. Therefore, they were not able to produce similarly high levels of turbulent fluctuations near the ground further downstream ($r/R \geq 1.6$) compared to locations upstream; see Figs. 3.40 and 3.41. Furthermore, the tip vortices were also measured a primary source of anisotropy in the turbulence (Section 3.3.5). Consequently, the turbulence distribution also became more isotropic further downstream, which is shown by the more homogeneous distribution of the turbulent fluctuations in the quadrants of the

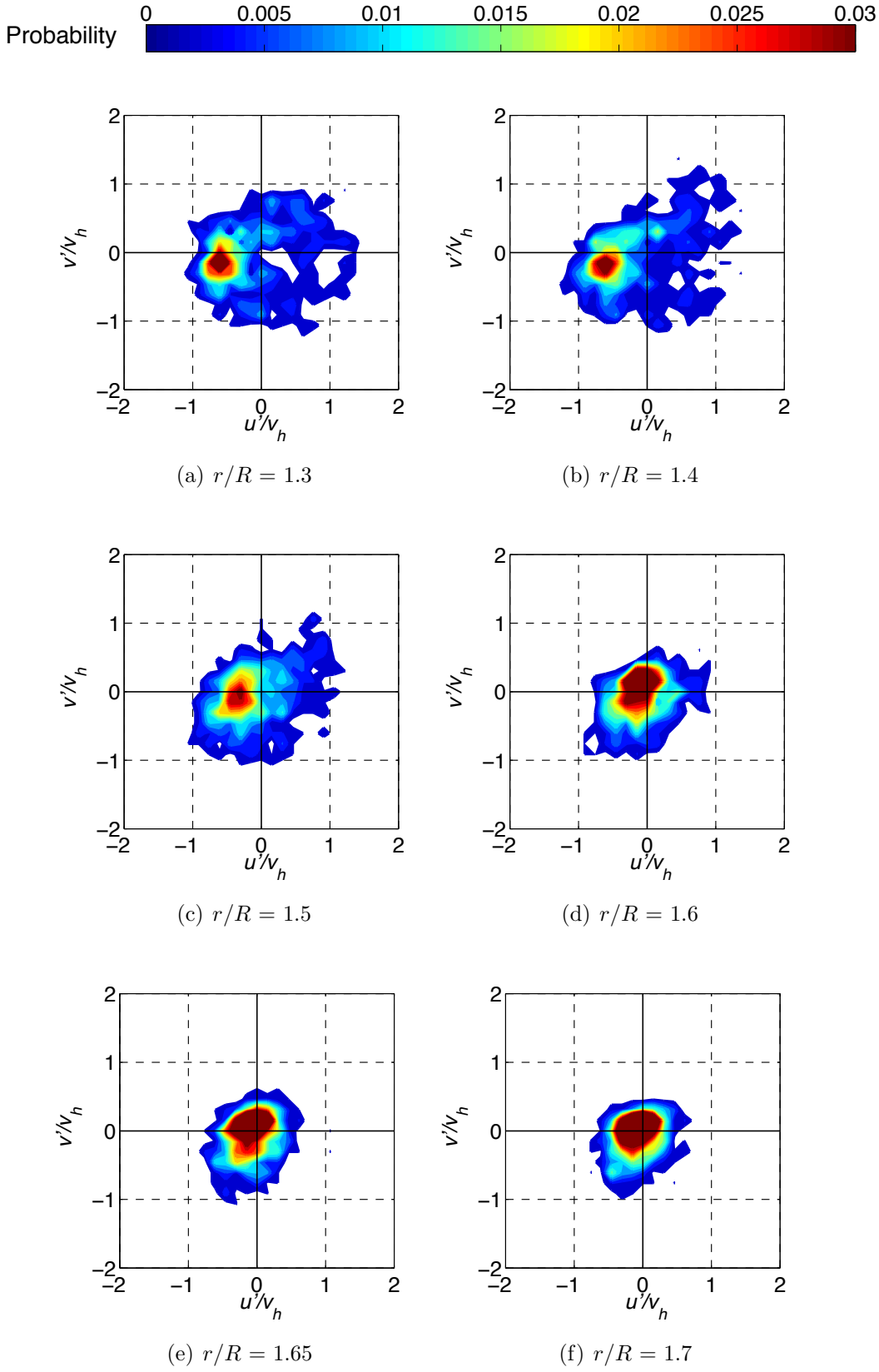

(a) $r/R = 1.3$

(b) $r/R = 1.4$

(c) $r/R = 1.5$

(d) $r/R = 1.6$

(e) $r/R = 1.65$

(f) $r/R = 1.7$

Figure 3.41: Joint frequency distributions of turbulence events for the carrier phase at $z/R = 0.07$ above the sediment bed.

joint frequency distributions for $r/R \geq 1.6$.

Relatively high wall-normal velocity fluctuations, v', were observed throughout all downstream measurement locations at a height of $z/R = 0.1$ above the sediment bed; see Fig. 3.42. These wall-normal velocity fluctuations were largely produced by the blade tip vortices, and they can be suppressed closer to the ground by the presence of a boundary, i.e., the sediment bed in this case; see Figs. 3.39(a) and 3.39(b). Following the development of the flow in downstream direction for this constant height above the bed shows a shift from the prevailing streamwise decelerated fluid ($r/R < 1.4$) to ejection motions ($r/R = 1.5$–1.65), and to more and more turbulence events with greater positive wall-normal fluctuations ($v' > 0$; upward, away from the ground) at $r/R = 1.65$–1.8. These positive (upward) excess velocities are important for particle uplift and suspension [106] and they were measured to be more prominent further downstream from the rotor ($r/R = 1.65$–1.8), which correlated well with the region where more sediment was uplifted to sufficient heights above the ground to be entrained into the main vortex flow; see Fig. 3.21.

Turbulence events with both positive u and v, i.e., accelerated fluid away from the wall, were previously shown to be most effective in picking up and suspending particles from the sediment bed, also transporting them to greater heights [62]. In the present measurements, these outward interaction events gained increasingly more weight in the turbulence distributions (i.e., their occurrence was more probable) downstream of $r/R = 1.6$; see Fig. 3.42. The instantaneous flow vectors based on the (Reynolds-decomposed) velocity fluctuations shown in Figs. 3.36(c),(d) and Figs. 3.37(d)–(f) further confirmed that these turbulence events were induced by the

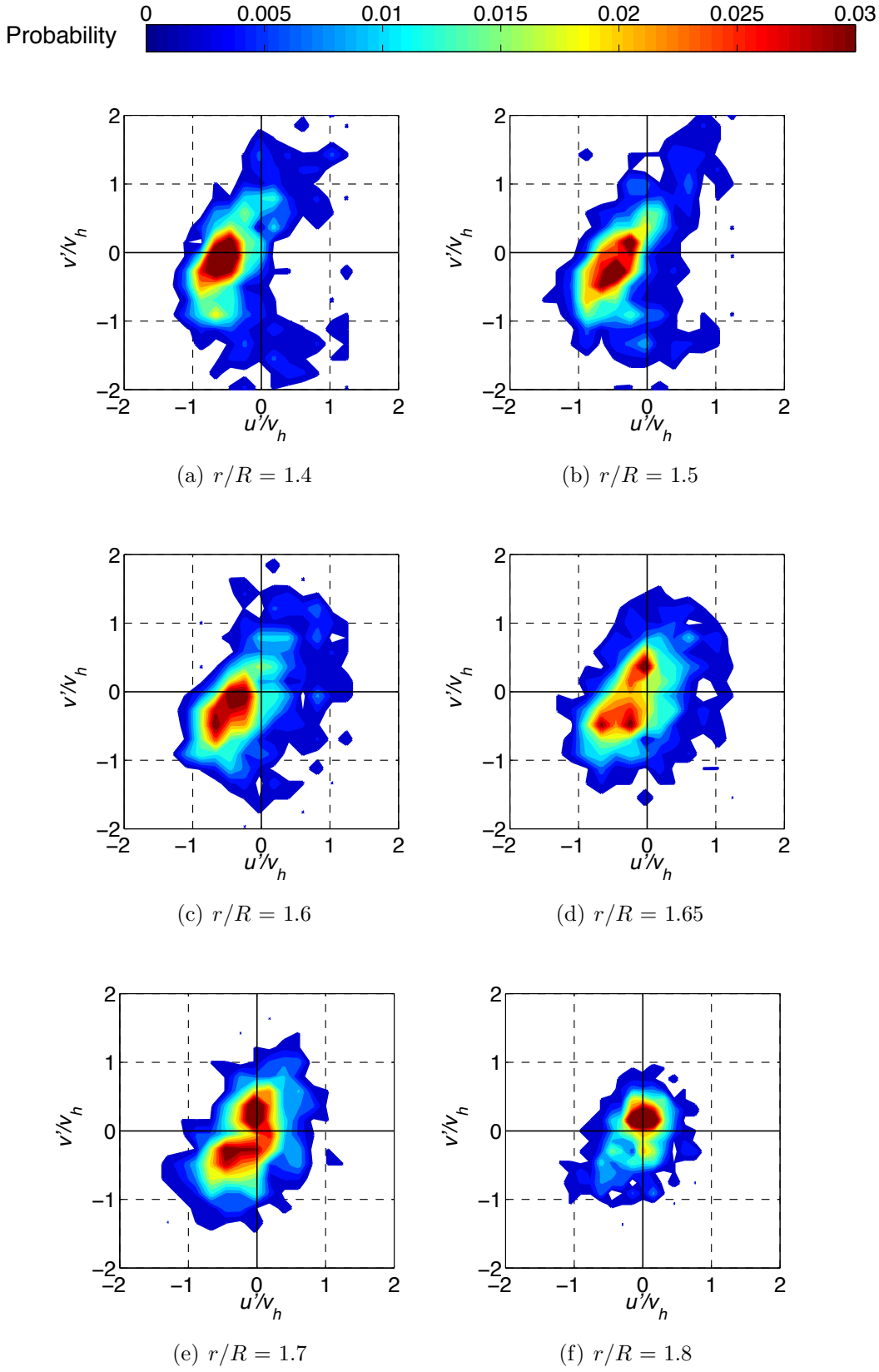

(a) $r/R = 1.4$

(b) $r/R = 1.5$

(c) $r/R = 1.6$

(d) $r/R = 1.65$

(e) $r/R = 1.7$

(f) $r/R = 1.8$

Figure 3.42: Joint frequency distributions of turbulence events for the carrier phase at $z/R = 0.1$ above the sediment bed.

blade tip vortices when they passed by and lifted up particles from the sediment bed in this region (i.e., $r/R \approx 1.6$–1.8).

Figure 3.42(d) shows the statistically prevailing ejections and inward interactions around $r/R \approx 1.65$ that were shown to facilitate initial particle uplift; see e.g., Figs. 3.35 and 3.36. These decelerated ($u' < 0$) turbulence events needed to be followed by a tip vortex convecting downstream. In most cases, only with this interplay between the decelerated turbulent motion downstream of the vortex and the positive excess velocities induced by this tip vortex itself, may the particles then be uplifted and entrained into the main rotor flow above the sediment bed, as also previously discussed in Figs. 3.36 and 3.37.

The local probability density distributions for the turbulence fluctuation velocities (as shown in Figs. 3.39–3.42) will be useful for modeling and simulation, in that existing numerical models can be validated. Furthermore, future computational models for the flow near the ground below rotors may be developed by including the statistical distributions of the turbulent fluctuations given by this work. For example, in computational models that are unable to predict turbulent fluctuations (i.e., models that are merely descriptions of the mean flow), these perturbations could be prescribed by statistical probability distributions to better simulate the flow near the sediment bed, which then will have effects on particle mobilization and uplift. It was shown in this present work that the turbulent fluctuations significantly affected sediment uplift and entrainment. Therefore, it may be important that the source of these fluctuations be also explicitly included in particle pickup and sediment entrainment models.

In an earlier study of particle resuspension and saltation in a water channel flow, it was observed [106] that particle suspension occurred from the combined action of a strong, coherent fast-moving ($u' > 0$) flow structure upstream of the particle pickup, and a downstream ejection motion (i.e., a turbulent motion with $u' < 0$ and $v' > 0$). This work also showed that uplifted particles were immersed in positive wall-normal velocity fluctuations, $v' > 0$. Similarly, in the present work the results in Figs. 3.35(b) and 3.36 showed that positive values of v' (i.e., excess velocities in the upward direction away from the bed) prevailed in the regions where most of the sediment particles were picked up and suspended by the tip vortices. This finding was also statistically confirmed by the results from a quadrant analysis.

In the present study, the downstream ejection motion previously observed [106] to contribute to sediment uplift was mostly caused by a clockwise-rotating secondary vortical structure downstream of the tip vortex; see Fig. 3.37. Despite these interesting parallels between the outcomes of these two studies, the flow characteristics and vortical structures in the rotor-generated flow were fundamentally different from the more canonical flow that was investigated in Ref. 106. Most notably were the sources of the relatively strong turbulent motions in the rotor-generated blade tip vortices and not in any naturally occurring flow structures near the wall.

3.5 Summary

In the present chapter, the results from the flow measurements for the single-phase and the dual-phase flows below rotors have been shown and thoroughly discussed. These measurements have given much insight into these rotor-generated wall-bounded flows, with and without sediment particles in the fluid flow, including an analysis of the boundary layers developing over the ground plane and the sediment bed below the rotors. Vortical structures and the turbulence characteristics of these rotor-generated flows were documented, and they were correlated to sediment mobilization and particle uplift from the underlying sediment bed. Furthermore, the detailed vortex flow–particle interactions were examined, including detailed investigations into the two-way coupling of the carrier flow to the dispersed particle flow, and vice versa.

Chapter 4: Conclusions

The present research has contributed to the understanding of the fluid dynamics responsible for the development of rotorcraft brownout conditions. The occurrence of brownout is characterized by the rapid evolution of a large dust cloud generated by a rotorcraft during takeoff, approach, or landing over terrain covered with loose sediment material such as desert sand. The severity of the dust cloud can greatly reduce the pilot's ability to distinguish visual cues on the ground that would normally be used for landing purposes.

It is the dynamic interplay of the flow features in the rotor wake and the interactions of the wake features with the ground that makes it difficult to discern the fundamental mechanisms that contribute to the mobilization and pickup of mobile particles and so to the formation of rotor-induced brownout conditions. Therefore, in the present work, flow field measurements near the ground below laboratory-scale rotors have been performed to understand the details of the rotor wake-induced flow, the flow-induced particle motion, and any particle-induced modifications to the vortical flow.

The primary objectives of the present research were to measure the particle mobilization and uplift from a mobile sediment bed below a rotor and to better

understand the fluid mechanics of the processes involved. The role of both concentrated vorticity and stochastic turbulence in the rotor flow was investigated as it influenced the motion of particles on the sediment bed and the subsequent pickup of these particles from the bed. Another objective of the work was to establish useful approximations and boundary conditions for the development of better sediment entrainment models that are based on justifiable physical assumptions and that can be deemed applicable to the modeling of rotor-induced brownout conditions. Furthermore, both of the flow phases were resolved simultaneously so as to be able to make detailed assessments regarding the degree of two-way coupling between the phases of this rotor-induced flow. That is, the goal was to relate possible changes in the coherent vortex structures, the mean flow, and the turbulence characteristics of the carrier flow phase directly to the action of the dispersed particle phase.

This final chapter provides a summary of the contributions of this work to the state of the art in brownout research and in multiphase fluid dynamics. The specific conclusions that were drawn from the performed measurements are given here, as well as recommendations for future work that could follow based on the results and conclusions made in the present research.

4.1 Summary of Contributions

The problem of rotorcraft brownout is governed by the complex two-phase fluid dynamical processes involved when a rotorcraft operates near surfaces covered with mobile sediment particles such as sand. The underlying fluid dynamics have to

be understood to be able to validate existing computational models or to develop new ones. Before any mitigation of the problem of brownout can even be attempted, the root cause of developing brownout conditions, i.e., the cause of the generation of a dust cloud around the rotorcraft, must be understood.

Because the problem of brownout is a truly multidisciplinary research problem, prior work has been reviewed in Chapter 1 as it pertains to the present work, including studies in sedimentology, flow physics, fluid/particle dynamics and multiphase flows, turbulence and boundary layer research. However, the results and conclusions from the reviewed studies are only partially applicable to the problem at hand because vortically-dominated flows have not yet been studied with respect to sediment mobilization and uplift, and also not with respect to the flow phase couplings in such flows.

Sediment entrainment models included in brownout simulations have been formulated based on more uniform, steady boundary-layer flows. These modeling approaches have been questioned by the experimental evidence that was given in the present work, revealing significant unsteady stresses on the ground that were generated by the rotor wake, and discrete unsteady flow features that were shown to contribute to sediment mobilization and uplift in the two-phase vortex flows generated by rotors. One impediment in the development and validation of appropriate models is that sediment entrainment in unsteady, rotor-generated vortical flows has not been quantified before, nor could particle entrainment be correlated to flow quantities other than the mean fluid velocity or the mean friction velocity at the sediment bed.

Therefore, time-resolved particle image and particle tracking velocimetry mea-

surements were made in the turbulent particle-laden flow environment below a hovering rotor near a ground plane that was covered with mobile sediment particles of 45–63 μm diameter, as discussed in detail in Chapter 2. These results were also compared to the near-wall flow produced by a nominally equivalent two-dimensional wall jet. The measurements permitted the resolution of the viscous sublayer, buffer layer, and log law region of the boundary layer as it developed over the ground below the rotor. The mean flow in the boundary layer at the ground below the rotor was found to be similar to a wall jet. However, the instantaneous flow field and turbulence characteristics between the two flows were found to be significantly different.

Measurements of the heterogeneous dual-phase flow field also exposed the complex interplay between the carrier and the dispersed particle phase of the flow. Further insight into the turbulent motions in the near-wall region was obtained using the quadrant analysis method, which revealed a preferential distribution of turbulence events near the sediment bed. To quantify both the particle mobilization on the sediment bed and the uplift of these particles from the bed, the particle fluxes in streamwise and wall-normal directions were measured, respectively. These measured particle fluxes were then correlated to discrete fluid structures and turbulence quantities of the carrier phase. With the simultaneous resolution of both of the flow phases and with the spatio-temporal resolution of the present measurements, changes in the temporal development of the vortical flow structures and the modified turbulence characteristics could be correlated to the action of the dispersed particle phase and to the degree of two-way coupling in such a complex flow.

4.2 Specific Conclusions

The key observations and conclusions drawn from the present work are listed in this section. These conclusions are divided into three subsections pertaining to 1. The single-phase near-wall flow at the ground below the rotor, 2. Particle mobilization, uplift and entrainment from the sediment bed, and 3. The flow phase coupling and turbulence modifications in the rotor-induced dual-phase flow environment.

4.2.1 Single-Phase Near-Wall Flow at the Ground

1. The time-averaged velocity fields at the ground below the rotor showed similar characteristics to those measured for a wall jet type of flow. However, significant spatial variations in the Reynolds shear stresses were found for the rotor flow, while the wall jet flow showed a much smoother wall-normal distribution. This outcome was shown to be because of the effects of the discrete tip vortices and associated turbulent vortex sheets trailed by the rotor, which are convected toward the ground and merge into the developing flow in the near-wall region.

2. The normal Reynolds stresses in streamwise direction were found to be the dominant component of the Reynolds stress tensor in the flow near the ground plane below a hovering rotor that was operating in ground effect. The streamwise Reynolds stresses were measured to be one order of magnitude greater than the shear stresses. This finding suggests that the streamwise turbulent stresses should be also included in modeling approaches of the investigated rotor-

generated flow, in most of which only the turbulent shear stress components are included.

3. Negative vorticity was produced by the interaction of the tip vortices with the ground. In some instances, this negative vorticity from the ground became entrained into the (still at this point) coherent vortices. It was found that when negative vorticity was entrained into the tip vortices, it acted to distort and destabilize the vortex and led to an enhanced diffusion of the vortices downstream of the location where the vorticity entrainment was detected.

4. Higher levels of turbulence were produced in the shear layer (or slipstream boundary) between the accelerated flow in the rotor wake and the more quiescent flow outside the wake. Moreover, the turbulence produced in this shear layer was found to be highly anisotropic, which raises the stakes for modeling this kind of flow because most computational models are based on the assumption of isotropic turbulence.

5. The tip vortices and the secondary (negative) vorticity induced at the ground were a primary source of anisotropy in the production of turbulence in the flow below the rotor. The loss of coherence in the tip vortices and their diffusion resulted in significantly less turbulence production and a more isotropic distribution of turbulence in the near-wall flow.

4.2.2 Particle Mobilization, Uplift and Entrainment

1. The streamwise Reynolds stress was found to be the dominant component of the Reynolds stress tensor in the dual-phase flow (as well as in the single-phase flow), and it was one order of magnitude greater than the Reynolds shear stress. The mobilization of particles on the sediment bed was also quantified by measuring the wall-parallel (streamwise) particle flux, which correlated well with the distribution of the streamwise Reynolds stress. It was predominantly the streamwise Reynolds stresses that were responsible for the initiation of bedload transport.

2. After the prior mobilization of upstream particles on the bed, coherent vortex structures were able to uplift these particles. Discrete turbulence events, their origin being mostly from the periodic passage of the blade tip vortices, were shown to be responsible for most of the particle pickup from the sediment bed. Statistically prevailing turbulence events with positive wall-normal velocity fluctuations (namely ejection and outward interaction events) were also seen to correlate well with the subsequent suspension of particles in the flow.

3. It was found that most tip vortices trailed a region of decelerated fluid. These negative streamwise velocity fluctuations (namely ejection and inward interaction motions) facilitated the initial particle uplift, in that they decelerated the particles that could subsequently be picked up by a succeeding (younger) part of the tip vortex.

4. Negative vorticity near the ground surface was produced by the interaction of the tip vortices with the ground. This negative vorticity was found to increase the mobilization and uplift of particles from the underlying sediment bed.

5. The present results confirm that the problem of rotorcraft brownout is driven by the intensity and proximity of the blade tip vortices to the sediment bed rather than by the average rotor-induced downwash flow. Although the concentrated vorticity contained in the tip vortices is a dominant feature of the flow below the rotor, secondary flow structures and turbulent motions were also found to contribute significantly to the process of particle uplift and entrainment.

4.2.3 Flow Phase Coupling and Turbulence Modifications

1. The turbulence characteristics of the carrier fluid in the dual-phase flow environment were found to be altered by the presence of suspended sediment particles in the flow. This two-way coupling of the phases produced significantly different distributions of Reynolds stresses compared to the flow results obtained without suspended sediment particles.

2. The dispersion of uplifted sediment particles in the dual-phase flow served to attenuate the turbulence field because of the distortion and enhanced diffusion of the concentrated vorticity. The source of this vorticity was initially in the blade tip vortices and also in any residual vorticity that was otherwise associated with the presence of the tip vortices or the vortex sheets that were trailed from the inner parts of the rotor blades.

3. In regions where the particle concentrations were high enough, i.e., at greater downstream distances from the rotor and near the ground plane, the presence of particles in the flow caused the deceleration of the mean fluid velocities.

4. The tip vortices and the secondary (negative) vorticity induced at the ground were the primary sources of anisotropy in the production of turbulence. However, it was found that after the concentrated vorticity contained in the blade tip vortices had diffused sufficiently (i.e., the primary sources of anisotropy had decayed), then the suspended particles were also found to augment the anisotropy in the turbulence field. This increased anisotropic turbulence was observed only in regions relatively far downstream from the rotor, where both the particle concentrations were relatively high and the tip vortices were mostly diffused.

4.3 Recommendations for Future Work

Some questions about the modeling of dual-phase vortical flows have been posed during the course of the present research. In the future, numerical models that are being used to simulate rotor-induced dust clouds and brownout conditions may have to better account for the two-way couplings between individual fluid structures and the particles, and the resulting turbulence modifications that were presented in this dissertation. Any flow models should at least account for the momentum exchange between the dispersed phase and the fluid phase, i.e., the fluid to be decelerated by the particles. In a further step, the models could also better account for particles

interacting with vortical structures and eddies, such as to allow the dispersed phase to diffuse vortical carrier-phase structures. Although the added complexity of the models and the increased computational expense will constitute a challenge of these higher-fidelity models, the results are expected to much better represent the actual flow physics that were identified and discussed in this dissertation.

Sediment mobilization and uplift processes were correlated to mean turbulence quantities (primarily the streamwise Reynolds stresses) and discrete turbulence events in the carrier-phase flow, respectively. The acquired experimental dataset and this previously unavailable knowledge about the causes for sediment mobilization and uplift may help to develop future entrainment models applicable to vortically-dominated, rotor-induced particle flows that lead to brownout conditions. From the experimental evidence that was shown in this research, such entrainment (or pickup) models will need to account for the effects of turbulence and discrete vortical structures and cannot solely rely on the mean (steady-flow boundary layer) fluid velocities as mobilization criteria.

With the previously unavailable turbulence characteristics for the rotor-induced flow near the ground, rotor-in-ground-effect models and simulations can now be better validated, for both single-phase and dual-phase flows. Certain regions of the flow field below the rotor revealed significantly high levels of anisotropy in the turbulence. Therefore, the use of turbulence models that are based on the assumption of isotropic turbulence should be applied with caution, at least in certain flow regimes. It should be examined whether using different turbulence models for this type of flow has a significant effect on the flow simulations.

Although the present work focused on the two-phase flow generated by a rotor, the outcomes of this work also have implications on other particle-laden flows that are vortically dominated. The findings of this dissertation may be applied to other research problems and they may be helpful for the studies and analyses of more industrial problems such as a turbulent pipe flow with suspended material, such as dirt, sedimentary deposition, fouling, etc.

Bibliography

[1] Syal, M., "Development of a Lagrangian-Lagrangian Methodology to Predict Brownout Dust Clouds," Ph.D. Dissertation, Department of Aerospace Engineering, University of Maryland, College Park, MD, May 2012.

[2] Sydney, A., Baharani, A., and Leishman, J. G., "Understanding Brownout using Near-Wall Dual-Phase Flow Measurements," 67th Annual Forum Proceedings of the American Helicopter Society, Virginia Beach, VA, May 3–5, 2011.

[3] Leishman, J. G., *Principles of Helicopter Aerodynamics*, 2nd ed., Cambridge University Press, New York, NY, 2006.

[4] Mapes, P., Kent, R., and Wood, R., "DoD Helicopter Mishaps FY85-05: Findings and Recommendations," U.S. Air Force, AFRL-WS-07-0731, Washington, DC, 2008.

[5] "NTSB Accident Briefs: LAX01LA283, LAX01LA304, LAX04LA285, SEA05CA173," National Transportation Safety Board.

[6] Jansen, C., Wennemers, A., and Groen, E., "FlyTact: A Tactile Display Improves a Helicopter Pilots Landing Performance in Degraded Visual Environments," *Haptics: Perception, Devices and Scenarios*, Vol. 502, No. 4, 2008, pp. 867–875.

[7] "Sandblaster 2: Support of See-Through Technologies for Particulate Brownout," Task 1 Technical Report, Sponsored by Defense Advanced Research Projects Agency (DOD) Strategic Technology Office, Issued by U.S. Army Aviation and Missile Command under Contract No. W31P4Q-07-C-0215, MRI Project No. 110565, October 31, 2007.

[8] "Sandblaster 2: Support of See-Through Technologies for Particulate Brownout," Task 5 Technical Report, Sponsored by Defense Advanced Research Projects Agency (DOD) Strategic Technology Office, Issued by U.S. Army Aviation and Missile Command under Contract No. W31P4Q-07-C-0215, MRI Project No. 110565, October 31, 2007.

[9] Tritschler, J., Syal, M., Celi, R., and Leishman, J. G., "A Methodology for Rotor Design Optimization for Rotorcraft Brownout Mitigation," 66th Annual Forum Proceedings of the American Helicopter Society, Phoenix, AZ, May 10–13, 2010.

[10] Betz, A., "The Ground Effect on Lifting Propellers," Technical Report TM-836, NACA, 1937.

[11] Knight, M., and Hefner, R. A., "Analysis of Ground Effect on the Lifting Airscrew," Technical Report TN-835, NACA, 1941.

[12] Zbrozek, J., "Ground Effect on the Lifting Rotor," Technical Report 2347, ARC R&M, 1947.

[13] Taylor, M. K., "A Balsa-Dust Technique for Air-Flow Visualization and Its Application to Flow Through Model Helicopter Rotors in Static Thrust," Technical Report TN-2220, NACA, 1950.

[14] Cheeseman, I. C., and Bennett, W. E., "The Effect of the Ground on a Helicopter Rotor in Forward Flight," Technical Report 3021, ARC R&M, 1955.

[15] Fradenburgh, E. A., "The Helicopter and the Ground Effect Machine," *Journal of the American Helicopter Society*, Vol. 5, No. 4, 1960, pp. 26–28.

[16] Fradenburg, E. A., "Aerodynamic Factors Influencing Overall Hover Performance," AGARD CP-111, 1972.

[17] Hayden, J. S., "The Effect of the Ground on Helicopter Hovering Power Required," American Helicopter Society 32th Annual National V/STOL Forum Proceedings, Washington, DC, May 10–12, 1976.

[18] Curtiss, H. C., Sun, M., Putman, W. F., and Hanker, E. J., "Rotor Aerodynamics in Ground Effect at Low Advance Ratios," *Journal of the American Helicopter Society*, Vol. 29, No. 1, 1984, pp. 48–55.

[19] Prouty, R. W., "Ground Effect and the Helicopter," AIAA Paper 85-4034, AIAA/AHS/ASEE Aircraft Design Systems and Operations Meeting, Colorado Springs, CO, October 14–16, 1985.

[20] Rossow, V. J., "Effect of Ground and/or Ceiling Planes on Thrust of Rotors in Hover," Technical Report TM-86754, NACA, 1985.

[21] Curtiss, H. C., Erdman, W., and Sun, M., "Ground Effect Aerodynamics," *Vertica*, Vol. 11, No. (1/2), 1987, pp. 29–42.

[22] Light, J. S., and Norman, T., "Tip Vortex Geometry of a Hovering Helicopter Rotor in Ground Effect," 45th Annual Forum Proceedings of the American Helicopter Society, Boston, MA, May 22–24, 1989.

[23] Martin, P. B., Leishman, J. G., Pugliese, J. P., and Anderson, S. L., "Stereoscopic PIV Measurements in the Wake of a Hovering Rotor," 56th Annual Forum Proceedings of the American Helicopter Society, Virginia Beach, VA, May 2–4, 2000.

[24] Martin, P. B., and Leishman, J. G., "Trailing Vortex Measurements in the Wake of a Hovering Rotor with Various Tip Shapes," 58th Annual Forum Proceedings of the American Helicopter Society, Montréal, Canada, June 11–13, 2002.

[25] Ramasamy, M., and Leishman, J. G., "Interdependence of Diffusion and Straining of Helicopter Blade Tip Vortices," *Journal of Aircraft*, Vol. 41, No. 5, September 2004, pp. 1014–1024.

[26] Raffel, M., Richard, H., Ehrenfried, K., van der Wall, B., Burley, C., Beaumier, P., McAlister, K., and Pengel, K., "Recording and Evaluation Methods of PIV Investigations on a Helicopter Rotor Model," *Experiments in Fluids*, Vol. 36, No. 1, 2004, pp. 146–156.

[27] Kindler, K., Goldhahn, E., Leopold, F., and Raffel, M., "Recent Developments in Background Oriented Schlieren Methods for Rotor Blade Tip Vortex Measurements," *Experiments in Fluids*, Vol. 43, No. 2-3, 2007, pp. 233–240.

[28] Raffel, M., de Gregorio, F., de Groot, K., Schneider, O., Sheng, W., Gibertini, G., and Seraudie, A., "On the Generation of a Helicopter Aerodynamic Database," *Aeronautical Journal*, Vol. 115, No. 1164, 2011, pp. 103–112.

[29] Saberi, H. A., and Maisel, M. D., "A Free-Wake Rotor Analysis Including Ground Effect," 43rd Annual Forum Proceedings of the American Helicopter Society, St. Louis, MO, May 18–20, 1987.

[30] Quackenbush, T. R., and Wachspress, D. A., "Enhancements to a New Free Wake Hover Analysis," Technical Report CR-177523, NASA, 1989.

[31] Graber, A., Rosen, A., and Seginer, A., "An Investigation of a Hovering Rotor in Ground Effect," 16th European Rotorcraft Forum Proceedings, Glasgow, Scotland, September 18–20, 1990.

[32] Itoga, N., Nagashima, T., Iboshi, N., Kawakami, S., Prasad, J. V. R., and Peters, D. A., "Numerical Analysis of Ground Effect for a Lifting Rotor Hovering at Close Proximity to Inclined Flat Surface," American Helicopter Society Specialists Meeting on Advanced Helicopter Technology and Disaster Relief, Gifu, Japan, April 21–23, 1999.

[33] Griffiths, D. A., Ananthan, S., and Leishman, J. G., "Predictions of Rotor Performance in Ground Effect Using a Free-Vortex Wake Model," *Journal of the American Helicopter Society*, Vol. 50, No. 4, 2005, pp. 302–314.

[34] Moulton, M., O'Malley, J. A., and Rajagopalan, G., "Rotorwash Prediction Using an Applied Computational Fluid Dynamics Tool," 60th Annual Forum Proceedings of the American Helicopter Society, Baltimore, MD, June 7–10, 2004.

[35] Brown, R., and Whitehouse, G., "Modeling Rotor Wakes in Ground Effect," *Journal of the American Helicopter Society*, Vol. 49, No. 3, October 2004, pp. 238–249.

[36] Nathan, N. D., and Green, R. B., "The Flow around a Model Helicopter Main Rotor in Ground Effect," *Experiments in Fluids*, Vol. 52, No. 1, 2012, pp. 151–166.

[37] Milluzzo, J., and Leishman, J. G., "Assessment of Rotorcraft Brownout Severity in Terms of Rotor Design Parameters," *Journal of the American Helicopter Society*, Vol. 55, No. 3, 2010, Paper 032009, pp. 1–9.

[38] Sydney, A., and Leishman, J. G., "Measurements of Rotor/Airframe Interactions in Ground Effect Over a Sediment Bed," 69th Annual Forum Proceedings of the American Helicopter Society, Phoenix, AZ, May 21–23, 2013.

[39] Lee, T. E., Leishman, J. G., and Ramasamy, M., "Fluid Dynamics of Interacting Blade Tip Vortices With a Ground Plane," *Journal of the American Helicopter Society*, Vol. 55, No. 2, 2010, Paper 022005, pp. 1–16.

[40] Nathan, N. D., and Green, R. B., "Measurements of a Rotor Flow in Ground Effect and Visualisation of the Brown-out Phenomenon," 64th Annual Forum Proceedings of the American Helicopter Society, Montréal, Canada, April 29–May 1, 2008.

[41] Johnson, B., Leishman, J. G., and Sydney, A., "Investigation of Sediment Entrainment Using Dual-Phase, High-Speed Particle Image Velocimetry," *Journal of the American Helicopter Society*, Vol. 55, No. 4, 2010, Paper 042003, pp. 1–16.

[42] Leishman, J. G., "Challenges in Understanding the Fluid Dynamics of Brownout: Review and Update," Proceedings of the AHS International Meeting on Advanced Rotorcraft Technology and Safety Operations, Omiya, Japan, November 1–3, 2010.

[43] Rauleder, J., and Leishman, J. G., "Flow Environment and Organized Turbulence Structures Near a Plane Below a Rotor," *AIAA Journal*, Vol. 52, No. 1, 2014, pp. 146–161.

[44] Milluzzo, J., Sydney, A., Rauleder, J., and Leishman, J. G., "In-Ground-Effect Aerodynamics of Rotors with Different Blade Tips," 66th Annual Forum Proceedings of the American Helicopter Society, Phoenix, AZ, May 10–13, 2010.

[45] Syal, M., Rauleder, J., Tritschler, J. K., and Leishman, J. G., "On the Possibilities of Brownout Mitigation Using a Slotted-Tip Rotor Blade," 29th AIAA Applied Aerodynamics Conference, Honolulu, HI, June 27–30, 2011.

[46] Tritschler, J., Syal, M., Celi, R., and Leishman, J. G., "The Effect of Number of Blades on Optimum Rotor Design for Brownout Mitigation," Future Vertical Lift Aircraft Design Conference, San Francisco, CA, January 18–20, 2012.

[47] Rauleder, J., and Leishman, J. G., "Particle–Fluid Interactions in Rotor-Generated Vortex Flows," *Experiments in Fluids*, Vol. 55, No. 3, 2014, pp. 1–15.

[48] Milluzzo, J., and Leishman, J. G., "Development of the Turbulent Vortex Sheet in the Wake of a Hovering Rotor," 69th Annual Forum Proceedings of the American Helicopter Society, Phoenix, AZ, May 21–23, 2013.

[49] Bagnold, R. A., *The Physics of Blown Sand and Desert Dunes*, Dover Publications, Inc., Mineola, NY, 1941.

[50] Shao, Y., and Lu, H., "A Simple Expression for Wind Erosion Threshold Friction Velocity," *Journal of Geophysical Research*, Vol. 105, No. D17, 2000, pp. 22,437–22,443.

[51] Clifford, N. J., McClatchey, J., and French, J. R., "Measurements of Turbulence in the Benthic Boundary Layer Over a Gravel Bed and Comparison Between Acoustic Measurements and Predictions of the Bedload Transport of Marine Gravels," *Sedimentology*, Vol. 38, No. 1, 1991, pp. 161–171.

[52] Sterk, G., Jacobs, A., and Van Boxel, J., "The Effect of Turbulent Flow Structures On Saltation Sand Transport in the Atmospheric Boundary Layer," *Earth Surface Processes and Landforms*, Vol. 23, 1998, pp. 877–887.

[53] Syal, M., Govindarajan, B., and Leishman, J. G., "Mesoscale Sediment Tracking Methodology to Analyze Brownout Cloud Developments," 66th Annual Forum Proceedings of the American Helicopter Society, Phoenix, AZ, May 10–13, 2010.

[54] Syal, M., and Leishman, J. G., "Modeling of Bombardment Ejection in the Rotorcraft Brownout Problem," *AIAA Journal*, Vol. 51, No. 4, 2013, pp. 849–866.

[55] Ballard, J. D., Orloff, K. L., and Lueds, A., "Effect of Tip Shape on Blade Loading Characteristics and Wake Geometry for a Two-Bladed Rotor in Hover," *Journal of the American Helicopter Society*, Vol. 25, No. 3, 1980, pp. 30–35.

[56] McVeigh, M. A., and McHugh, F. J., "Influence of Tip Shape, Chord, Blade Number, and Airfoil on Advanced Rotor Performance," *Journal of the American Helicopter Society*, Vol. 29, No. 4, 1984, pp. 55–62.

[57] Leishman, J. G., Martin, P. B., and Pugliese, G., "High Resolution Trailing Vortex Measurements in the Wake of a Hovering Rotor," *Journal of the American Helicopter Society*, Vol. 48, No. 1, 2003, pp. 39–52.

[58] Han, O. Y., and Leishman, J. G., "Experimental Investigation of Tip Vortex Alleviation Using a Slotted Tip Rotor Blade," *AIAA Journal*, Vol. 42, No. 4, 2004, pp. 523–535.

[59] Wallace, J. M., Eckelmann, H., and Brodkey, R. S., "The Wall Region in Turbulent Shear Flow," *Journal of Fluid Mechanics*, Vol. 54, 1972, pp. 39–48.

[60] Robinson, S. K., "Coherent Motions in the Turbulent Boundary Layer," *Annual Review of Fluid Mechanics*, Vol. 23, 1991, pp. 601–639.

[61] Carlier, J., and Stanislas, M., "Experimental Study of Eddy Structures in a Turbulent Boundary Layer Using Particle Image Velocimetry," *Journal of Fluid Mechanics*, Vol. 535, 2005, pp. 143–188.

[62] Nelson, J. M., Shreve, R. L., McLean, S. R., and Drake, T. G., "Role of Near-Bed Turbulence Structure in Bed Load Transport and Bed Form Mechanics," *Water Resources Research*, Vol. 31, No. 8, 1995, pp. 2071–2086.

[63] Kaftori, D., Hetsroni, G., and Banerjee, S., "The Effect of Particles on Wall Turbulence," *International Journal of Multiphase Flow*, Vol. 24, No. 3, 1998, pp. 359–386.

[64] Sterk, G., Van Boxel, J., and Zuurbier, R., "Interactions Between Turbulent Wind Flow and Saltation Sand Transport," ICAR5/GCTE-SEN Joint Conference Proceedings, Lubbock, TX, July 22–25, 2002.

[65] Sutherland, A. J., "Proposed Mechanism for Sediment Entrainment by Turbulent Flows," *Journal of Geophysical Research*, Vol. 72, No. 24, 1967, pp. 6183–6194.

[66] Williams, J. J., Butterfield, G. R., and Clark, D. G., "Rates of Aerodynamic Entrainment in a Developing Boundary Layer," *Sedimentology*, Vol. 37, No. 6, 1990, pp. 1039–1048.

[67] Xuan, J., and Robins, A., "The Effects of Turbulence and Complex Terrain on Dust Emissions and Depositions from Coal Stockpiles," *Atmospheric Environment*, Vol. 28, No. 11, 1994, pp. 1951–1960.

[68] Xuan, J., "Turbulence Factors for Threshold Velocity and Emission Rate of Atmospheric Mineral Dust," *Atmospheric Environment*, Vol. 38, No. 12, 2004, pp. 1777–1783.

[69] Poelma, C., Westerweel, J., and Ooms, G., "Particle–Fluid Interactions in Grid-Generated Turbulence," *Journal of Fluid Mechanics*, Vol. 589, 2007, pp. 315–351.

[70] Montante, G., and Magelli, F., "Mixed Solids Distribution in Stirred Vessels: Experiments and Computational Fluid Dynamics Simulations," *Industrial and Engineering Chemical Research*, Vol. 46, No. 9, 2007, pp. 2885–2891.

[71] Montante, G., Paglianti, A., and Magelli, F., "Analysis of Dilute Solid–Liquid Suspensions in Turbulent Stirred Tanks," *Chemical Engineering Research and Design*, Vol. 90, No. 10, 2012, pp. 1448–1456.

[72] Unadkat, H., Rielly, C. D., Hargrave, G. K., and Nagy, Z. K., "Application of Fluorescent PIV and Digital Image Analysis to Measure Turbulence Properties of Solid–Liquid Stirred Suspensions," *Chemical Engineering Research and Design*, Vol. 87, No. 4, 2009, pp. 573–586.

[73] Wenren, Y., Walter, J., Fan, M., and Steinhoff, J., "Vorticity Confinement and Advanced Rendering to Compute and Visualize Complex Flows," Paper AIAA-2006-945, 44th AIAA Aerospace Sciences Meeting and Exhibit, Reno, Nevada, January 9–12, 2006.

[74] Ryerson, C. C., Haehnel, R. B., Koenig, G. G., and Moulton, M. A., "Visibility Enhancement in Rotorwash Clouds," Paper AIAA-2005-263, 43rd AIAA Aerospace Sciences Meeting and Exhibit, Reno, Nevada, January 10–13, 2005.

[75] Haehnel, R. B., Moulton, M. A., Wenren, W., and Steinhoff, J., "A Model to Simulate Rotorcraft-Induced Brownout," 64th Annual Forum Proceedings of the American Helicopter Society, Montréal, Canada, April 29–May 1, 2008.

[76] Phillips, C., and Brown, R. E., "Eulerian Simulation of the Fluid Dynamics of Helicopter Brownout," *Journal of Aircraft*, Vol. 46, No. 4, July 2009, pp. 1416–1429.

[77] D'Andrea, A., "Numerical Analysis of Unsteady Vortical Flows Generated by a Rotorcraft Operating on Ground: A First Assessment of Helicopter Brownout," 65th Annual Forum Proceedings of the American Helicopter Society, Grapevine, Texas, May 27–29, 2009.

[78] Wachspress, D., A., Whitehouse, G., R., Keller, J., D., and Yu, H., "A High Fidelity Brownout Model for Real-Time Flight Simulations and Trainers," 65th Annual Forum Proceedings of the American Helicopter Society, Grapevine, TX, May 27–29, 2009.

[79] Syal, M., and Leishman, J. G., "Predictions of Brownout Dust Clouds Compared to Photogrammetric Measurements," *Journal of the American Helicopter Society*, Vol. 58, No. 1, 2013, pp. 1–18.

[80] Mendoza-Cabrales, C., "Refined Modeling of Shallow, Turbulent Flow over Dunes," Ph.D. Dissertation, Department of Civil Engineering, Colorado State University, Fort Collins, CO, 1987.

[81] McLean, S. R., and Smith, J. D., "A Model for Flow over Two-Dimensional Bed Forms," *Journal of Hydraulic Engineering*, Vol. 112, No. 4, 1986, pp. 300–317.

[82] Mulinti, R., and Kiger, K. T., "Two-Phase PIV Measurements of Particle Suspension in a Forced Impinging Jet," 63rd Annual Meeting of the APS Division of Fluid Dynamics, Long Beach, CA, November 21–23, 2010.

[83] Sechet, P., and Le Guennec, B., "The Role of Near Wall Turbulent Structures on Sediment Transport," *Water Resources Research*, Vol. 33, No. 17, 1999, pp. 3646–3656.

[84] Best, J., "On the Entrainment of Sediment and Initiation of Bed Defects: Insights from Recent Developments within Turbulent Boundary Layer Research," *Sedimentology*, Vol. 39, No. 5, 1992, pp. 797–811.

[85] Iversen, J. D., "Simulated Atmospheric Vortex Threshold," ICAR5/GCTE-SEN Joint Conference Proceedings, Lubbock, TX, July 22–25, 2002.

[86] Poelma, C., and Ooms, G., "Particle-Turbulence Interaction in a Homogeneous, Isotropic Turbulent Suspension," *Applied Mechanics Reviews*, Vol. 59, No. 2, 2006, pp. 78–90.

[87] Li, F., Haiying, Q., and Changfu, Y., "Phase Doppler Anemometry Measurements and Analysis of Turbulence Modulation in Dilute Gas–Solid Two-Phase Shear Flows," *Journal of Fluid Mechanics*, Vol. 663, 2010, pp. 434–455.

[88] Kulick, J. D., Fessler, J. R., and Eaton, J. K., "Particle Response and Turbulence Modification in Fully Developed Channel Flow," *Journal of Fluid Mechanics*, Vol. 277, 1994, pp. 109–134.

[89] Kiger, K. T., and Pan, C., "Suspension and Turbulence Modification Effects of Solid Particulates on a Horizontal Turbulent Channel Flow," *Journal of Turbulence*, Vol. 19, No. 3, 2002, pp. 1–17.

[90] Elghobashi, S., "On Predicting Particle-Laden Turbulent Flows," *Journal of Applied Sciences Research*, Vol. 52, No. 4, 1994, pp. 309–329.

[91] Taniere, A., Oesterle, B., and Monnier, J. C., "On the Behaviour of Solid Particles in a Horizontal Boundary Layer with Turbulence and Saltation Effects," *Experiments in Fluids*, Vol. 23, No. 6, 1997, pp. 463–471.

[92] Fessler, J. R., and Eaton, J. K., "Turbulence Modification by Particles in a Backward-Facing Step Flow," *Journal of Fluid Mechanics*, Vol. 394, 1999, pp. 97–117.

[93] Hwang, W., and Eaton, J. K., "Homogeneous and Isotropic Turbulence Modulation by Small Heavy Paticles," *Journal of Fluid Mechanics*, Vol. 564, 2006, pp. 361–393.

[94] Tanaka, T., and Eaton, J. K., "Sub-Kolmogorov Resolution Particle Image Velocimetry Measurements of Particle-Laden Forced Turbulence," *Journal of Fluid Mechanics*, Vol. 643, 2010, pp. 177–206.

[95] Gualtieri, P., Picano, F., Sardina, G., and Casciola, C. M., "Clustering and Turbulence Modulation in Particle-Laden Shear Flows," *Journal of Fluid Mechanics*, Vol. 715, 2013, pp. 134–162.

[96] Thiesset, F., Danaila, L., and Antonia, R. A., "Dynamical Effect of the Total Strain Induced by the Coherent Motion on Local Isotropy in a Wake," *Journal of Fluid Mechanics*, Vol. 720, 2013, pp. 393–423.

[97] Adrian, R. J., and Westerweel, J., *Particle Image Velocimetry*, Cambridge University Press, New York, NY, 2011.

[98] Leishman, J. G., "On Seed Particle Dynamics in Tip Vortex Flows," *Journal of Aircraft*, Vol. 33, No. 4, 1996, pp. 823–825.

[99] Martin, P. B., Bhagwat, M. J., and Leishman, J. G., "Strobed Laser-Sheet Visualization of a Helicopter Rotor Wake," *Journal of Flow Visualization and Image Processing*, Vol. 7, No. 1, 2000.

[100] Bhagwat, M. J., and Leishman, J. G., "Correlation of Rotor Tip Vortex Measurements," *AIAA Journal*, Vol. 38, No. 2, 2000, pp. 301–308.

[101] Scarano, F., "Iterative Image Deformation Methods in PIV," *Measurement Science and Technology*, Vol. 13, No. 1, 2002, pp. R1–R19.

[102] Rohaly, J., Frigerio, F., and Hart, D., "Reverse Hierarchical PIV Processing," *Measurement Science and Technology*, Vol. 13, No. 7, 2002, pp. 984–996.

[103] Wong, O. D., and Tanner, P. E., "Photogrammetric Measurements of an EH-60L Brownout Cloud," 67th Annual Forum Proceedings of the American Helicopter Society, Phoenix, AZ, May 10–13, 2010.

[104] Baharani, A., "Investigation into the Effects of Aeolian Scaling Parameters on Sediment Mobilization Below a Hovering Rotor," M.S. Thesis, Department of Aerospace Engineering, University of Maryland, College Park, MD, May 2011.

[105] Zeng L., Balachandar S., Fischer P., and Najjar F., "Interactions of a Stationary Finite-Sized Particle with Wall Turbulence," *Journal of Fluid Mechanics*, Vol. 594, 2008, pp. 271–305.

[106] van Hout, R., "Spatially and Temporally Resolved Measurements of Bead Resuspension and Saltation in a Turbulent Water Channel Flow," *Journal of Fluid Mechanics*, Vol. 715, 2013, pp. 389–423.

[107] Zhang, W., Wang, Y., and Lee, S. J., "Simultaneous PIV and PTV Measurements of Wind and Sand Particle Velocities," *Experiments in Fluids*, Vol. 45, No. 2, 2008, pp. 241–256.

[108] Kiger, K. T., and Pan, C., "PIV Technique for the Simultaneous Measurement of Dilute Two-Phase Flows," *Journal of Fluids Engineering*, Vol. 122, No. 4, 2000, pp. 811–818.

[109] Khalitov, D. A., and Longmire, E. K., "Simultaneous Two-Phase PIV by Two-Parameter Phase Discrimination," *Experiments in Fluids*, Vol. 32, No. 2, 2002, pp. 252–268.

[110] Mulinti, R., and Kiger, K. T., "Particle Suspension by a Forced Jet Impinging on a Mobile Sediment Bed," 16th International Symposium on Applications of Laser Techniques to Fluid Mechanics, Lisbon, Portugal, July 09–12, 2012.

[111] Westerweel, J., and Scarano, F., "Universal Outlier Detection for PIV Data," *Experiments in Fluids*, Vol. 39, No. 6, 2005, pp. 1096–1100.

[112] Irwin, H. P. A. H., "Measurements in a Self-Preserving Plane Wall Jet in a Positive Pressure Gradient," *Journal of Fluid Mechanics*, Vol. 61, 1973, pp. 33–63.

[113] Klebanoff, P. S., "Characteristics of Turbulence in a Boundary Layer with Zero Pressure Gradient," Technical Report 1247, NACA, 1955.

[114] Purtell, L. P., Klebanoff, P. S., and Buckley, F. T., "Turbulent Boundary Layer at Low Reynolds Number," *Physics of Fluids*, Vol. 24, No. 5, 1981, pp. 802–811.

[115] Antonia, R. A., Bisset, D. K., and Browne, L. W. B., "Effect of Reynolds Number on the Topology of the Organized Motion in a Turbulent Boundary Layer," *Journal of Fluid Mechanics*, Vol. 213, 1990, pp. 267–286.

[116] Wygnanski, I., Katz, Y., and Horev, E., "On the Applicability of Various Scaling Laws to the Turbulent Wall Jet," *Journal of Fluid Mechanics*, Vol. 234, 1992, pp. 669–690.

[117] Hebbar, K. S., and Melnik, W. L., "Wall Region of a Relaxing Three-Dimensional Incompressible Turbulent Boundary Layer," *Journal of Fluid Mechanics*, Vol. 85, 1978, pp. 39–48.

[118] Bernard, P. S., and Wallace, J. M., *Turbulent Flow: Measurement, Analysis and Prediction*, John Wiley & Sons, New York, NY, 2002.

[119] Ramasamy, M., Johnson, B., and Leishman, J. G., "Turbulent Tip Vortex Measurements Using Dual-Plane Stereoscopic Particle Image Velocimetry," *AIAA Journal*, Vol. 47, No. 8, 2009, pp. 1826–1840.

[120] Geiser, J., and Kiger, K., "A Simplified Analog for a Rotorcraft-in-Ground-Effect Flow Using a Forced Impinging Jet," 63rd Annual Meeting of the APS Division of Fluid Dynamics, Long Beach, CA, November 21–23, 2010.

[121] Papanicolaou, A. N., Diplas, P., Dancey, C. L., and Balakrishnan, M., "Surface Roughness Effects in Near-Bed Turbulence: Implications to Sediment Entrainment," *Journal of Engineering Mechanics*, Vol. 127, No. 3, 2001, pp. 211–218.

[122] Cellino, M., and Lemmin, U., "Influence of Coherent Flow Structures on the Dynamics of Suspended Sediment Transport in Open-Channel Flow," *Journal of Hydraulic Engineering*, Vol. 130, No. 11, 2004, pp. 1077–1088.

[123] Ramasamy, M., and Leishman, J. G., "A Generalized Model for Transitional Blade Tip Vortices," *Journal of the American Helicopter Society*, Vol. 51, No. 1, January 2006, pp. 92–103.

[124] Corino, E. R., and Brodkey, R. S., "A Visual Investigation of the Wall Region in Turbulent Flow," *Journal of Fluid Mechanics*, Vol. 37, 1969, pp. 1–30.